universität wien

MASTERARBEIT / MASTER'S THESIS

Titel der Masterarbeit / Title of the Master's Thesis

Utilizing spins in a nitrogen-vacancy center for tests of quantum mechanics

verfasst von / submitted by

Denis Mijatovic, BSc

angestrebter akademischer Grad / in partial fulfilment of the requirements for the degree of

Master of Science (MSc)

Wien, 2019 / Vienna, 2019

Studienkennzahl lt. Studienblatt / degree programme code as it appears on the student record sheet:	A 066 876
Studienrichtung lt. Studienblatt / degree programme as it appears on the student record sheet:	Masterstudium Physik UG2002
Betreut von / Supervisor:	Univ.-Prof. Dipl.-Ing. Dr. Philip Walther
Mitbetreut von / Co-Supervisor:	Michael Trupke, PhD

Abstract

A small set of comprehensible demonstrations for the utility of nitrogen-vacancy center spins is provided within the framework of quantum mechanical tests covering spin entanglement, reversal of decoherence, the invasiveness of measurements and the reality of the quantum state. Considering the nature of the presented experiments, they offer a coherent description of the relevant phenomena by virtue of connecting them to the underlying mechanisms like energy level splittings, populations, coherences, phases, Rabi oscillations, off-resonant driving, transition efficiencies of pulses, decoherence etc. Besides the actual results of the experiments, a method for the preparation and projection of potentially arbitrary spin states for the nitrogen nucleus is suggested as a tool. Its performance is tested for a set of orthogonal and nearly orthogonal states as well as the ability of inverting the procedure for these states. Using this scheme, a prominent test for the reality of the quantum state is translated to the nuclear spin and the result is found to be highly promising in the sense that it is highly likely to yield a statistically relevant outcome by slight improvement of the experimental conditions.

Zusammenfassung

Diese Arbeit umfasst eine Reihe an Demonstrationen der Nützlichkeit von Spins im Stickstoff-Fehlstellen-Zentrum im Zusammenhang quantenmechanischer Tests, die die Konzepte Verschränkung, Umkehr von Dekohärenz, eingreifende Messungen und Realität des Quantenzustandes abdecken. Die Experimente sind so konzipiert, dass sie die relevanten Phänomene in kohärenter Weise auf die zugrundeliegenden Mechanismen wie Aufspaltungen von Energieniveaus, Populationen, Kohärenzen, Phasen, Rabi-Oszillationen, nicht-resonantes Treiben, Übergangswirksamkeiten von Pulsen, Dekohärenz etc. zurückführen. Neben den eigentlichen Resultaten der Experimente wird eine Methode zur Vorbereitung und Projektion potentiell beliebiger Spin-Zustände des Stickstoff-Kerns vorgestellt. Der Erfolg wird für einen Satz an orthogonalen und nahezu orthogonalen Zustände gezeigt und auch, dass die Prozedur für diese invertiert werden kann. Damit wird ein prominenter Test der Realität des Quantenzustandes auf den Kernspin übersetzt und das Resultat ist vielversprechend in dem Sinne, dass es andeutet, dass das Experiment höchstwahrscheinlich unter leicht verbesserten experimentellen Bedingungen einen statistisch relevanten Wert hervorbringen würde.

Contents

1 Introduction

The development of techniques for handling elementary quantum information systems like spins is of great technological as well as scientific merit. The efforts of building a functional quantum computer depend not least on the precise control of the quantum states, once sufficient coherence times are established. Besides the feasibility for pragmatic applications, these endeavours have a value in and of themselves, especially in the science of quantum theory itself. Understanding the nature of quantum mechanics after all is among the most important, if not the most important, goals of modern physics. Transcribing the language of the theory to actual quantum systems, in this case solid state spins that have highly convenient features, is an important process that links our current understanding to the potential knowledge of the future by inquiring the empirical machinery. The courteous interplay between these two worlds facilitates any fundamental progress and its importance cannot possibly be overemphasized. One common theme of the overall project introduced here, or rather of quantum physics in general, is the lack of clear distinction between purely mathematical descriptions and actual physical entities. It connects to the persistent question about what the quantum state, being a vector in a complex vector space, actually is. This question is partially addressed, not least in the last experiment involving a related test. The nitrogen-vacancy center is a fascinating quantum system that finds application in a variety of fields. The long coherence times of the defect spins at room temperature allow for involved manipulations of their states which also constitutes the bedrock for the experiments in this work. The first topic regards the entanglement of electron and nuclear spin. By measuring the degree of coherence between the entangled components and witnessing the loss of it through decoherence, the theoretical expectation is married with the empirically known facts about the electron's interaction with the environment. Experimentally transitioning through all accessible degrees of entanglement, the symmetry of the problem is shown also to be as expected and thereby the maximum entanglement is found and calculated. The electron spin decoheres by the interaction with the environment. It is found that this process can be partially reversed by virtue of inverting the spin state through the application of spin flips. A limiting factor is identified and the decoherence process is then used to simulate a measurement by a fundamentally independent party. The effect of this invasive interaction is demonstrated and put in contrast to the case of no intervention. The last chapter deals with the coherent preparation of nearly pure nuclear spin states. A technique for preparing potentially arbitrary spin states is suggested, combined with a way of projecting any state onto an eigenstate. It is shown that these transformations can be inverted and that orthogonal states can be achieved. Utilizing this discovery, the ambitious goal of proving the reality of the quantum state is undertaken. The outcome implies that this test is possible with the nitrogen-vacancy center by performing a minor optimization. The ontological parameter is computed in a statistically non-rigorous (incomplete) way.

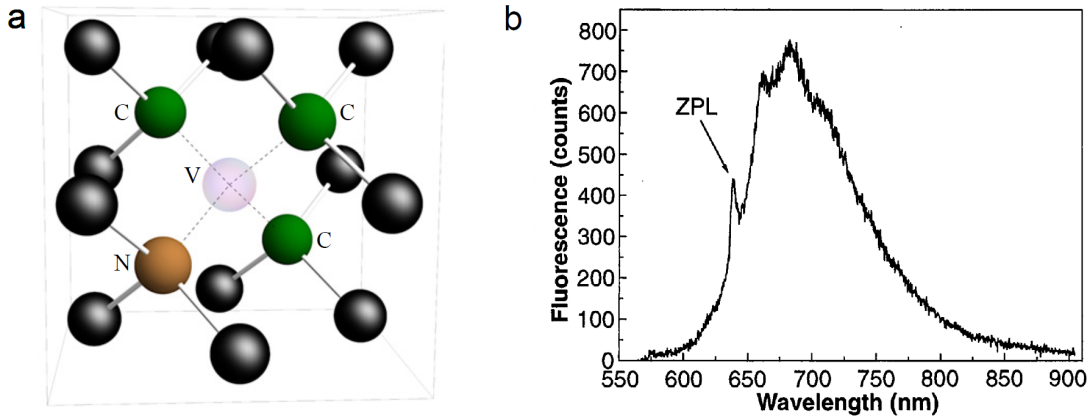

Figure 1: Lattice structure and fluorescence spectrum of the nitrogen-vacancy (NV) center. a) The NV center consists of one nitrogen atom replacing a carbon atom in the diamond lattice accompanied by a vacancy at a neighbouring site. b) Fluorescence spectrum of a single NV^- center at room temperature excited by a laser of wavelength 514 nm. The sharp zero phonon line (ZPL) at 637 nm corresponds to a resonant transition between ground state and excited state. The longer wavelength characteristics are attributed to vibronic bands of phonons [1, 2]. Reproduced from References [3, 4].

2 The Nitrogen-Vacancy Center

2.1 General Remarks

The nitrogen-vacancy (NV) center in diamond is a point defect prominent for its long coherence times of the electron spins and the nitrogen nuclear spin, even at room temperature. While the electron spins couple more strongly to the environment, for isotopically pure diamonds a coherence time of 1.8 ms has been observed [5]. The NV center comes in two different charge states, the neutral NV^0 and the negatively charged NV^-. The photoconversion process from NV^- to NV^0, however, is weak for low powers of the exciting laser [1] and no spin manipulations in the NV^0 state have been achieved so far. This work, also, exclusively concentrates on the NV^- charge state. In addition to areas of application like magnetometry and metrology in general, the NV center, by now, has been utilized in many projects for photonics and quantum mechanics purposes. Some examples include milestone room temperature demonstrations of quantum registers built upon the NV electronic spin and proximal N and ^{13}C nuclear spins [6, 7], spin-photon entanglement between the ground state spin of a single NV center and the polarisation of an emitted photon at low temperature ($<$10 K) [8], demonstrations of NV–NV spin coupling [9], important steps towards photonic coupling [10], Bell inequality violation [11], magnetic resonance beyond the

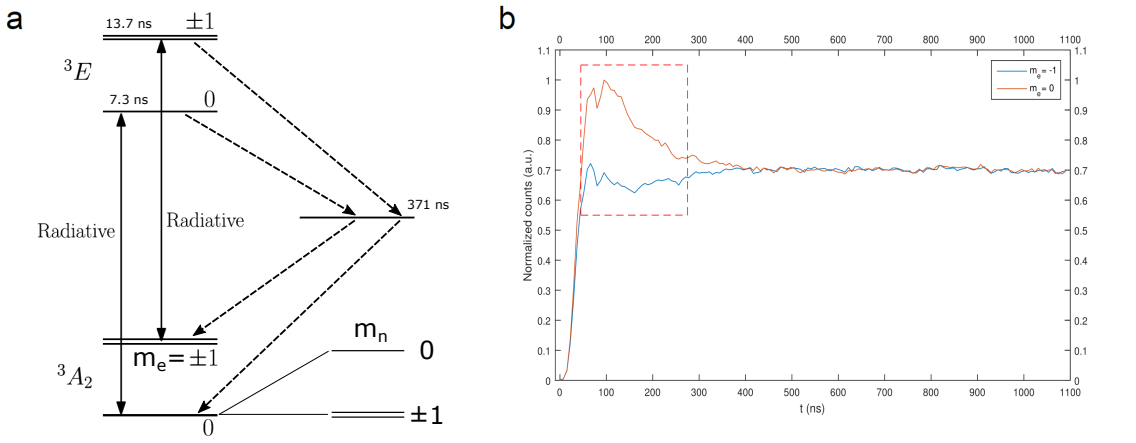

Figure 2: NV^- energy levels and fluorescence time trace. a) The ground state ($^3A_2$) and the excited state (^3E) are split up by zero field splittings onto spin states 0 and ± 1 of the electron spin m_e and the ^{14}N nuclear spin m_n. The non-radiative transitions to and from the intermediate state are indicated by dashed lines (lifetimes taken from Reference [17]). b) The fluorescence time trace of the NV center involves a spin-dependent part that allows readout of the electron spin in this time (cf. Section 6.1).

rotating frame approximation [12], detection of the Meissner effect [13], quantum process tomography [14] and quantum cryptography [15, 16]. Like some of the above, the demonstrations in this thesis lie within the scope of quantum information processing and the foundations of quantum mechanics.

2.2 Level Scheme and Fluorescence

Figure 2 shows the electronic level structure of NV^- with the ground state $^3A_2$, the excited state ^3E and one intermediate state. Off-resonant excitation of the NV with a laser frequency higher than the transition frequency between ground state and excited state is possible due to a phonon band that lies above the excited state (not shown in the diagram). The NV^- comprises two unpaired electrons occupying degenerate molecular orbits in the vacancy that are formed by dangling bonds between the carbon atoms and the nitrogen atom surrounding it. One electron, it is believed, is accepted from a nearby donor [3], thus giving a net negative charge and triplet states for the electron spin. The states are split by zero field splittings and a similar pattern translates to the nuclear spin of the, in this case, ^{14}N nucleus but there the splitting is flipped upside down due to the opposite sign of the gyromagnetic ratio. In the non-zero electron spin states, there is also hyperfine coupling between electron spin and nuclear spin which makes the energy levels shift accordingly. A more detailed picture of the energy levels is given in Section 6.3. When the system is optically driven by a laser,

the decay channels in Figure 2 leading to the intermediate state result in a polarization of the electron spin. As they favour the transition to electron spin 0, this spin state can be polarized to a significant degree by applying a laser pulse. This allows for the preparation of detectable electron spin states. The readout is accomplished by the spin dependent property of the fluorescence time trace seen in Figure 2. By collecting the counts in this special time window, one can assess the electron spin state in a relative manner. As it turns out, this is sufficient to do a lot of experiments as this offers a linear handle on the populations in the electron spin states. The electron spin is the readout channel onto which every information that is to be read out is projected, e.g. if a nuclear spin manipulation is being performed, simply shining a laser onto the system doesn't change a thing in the fluorescence signal. Applying a NOT gate on the electron spin, however, controlled by the nuclear spin gives a linear handle on the population in the control state of the nucleus. With knowledge about the nuclear spin polarization, this relative measure can be concretized. For all spin manipulations, the usual selection rules for magnetic dipole transitions (here, basically $\Delta J = \pm 1$) apply.

2.3 Application of a Static Magnetic Field

When a static magnetic field, e.g. by virtue of a small bar magnet, is applied to the NV center, the non-zero electron spin states split apart which makes them selectively addressable. Obviously, the nuclear spin states also split slightly and the selectivity of manipulations is also somewhat improved. At a magnetic field strength of approximately 500 G, an excited state level anticrossing occurs between the electron spin states 0 and -1 [18]. Via a mixing process in the excited state governed by the hyperfine interaction that couples states with equal sum of electron and nuclear spins and a difference in each of ± 1, the nuclear spin is polarized [19]. The fact that the $m_e = -1$ state (m_e is the electron spin) couples more strongly to the decay channel over the intermediate states described above introduces an asymmetry between mixing processes that increase the nuclear spin m_n and those that decrease it. The increasing processes win because the radiative decay rate is the same for $m_e = 0$ and $m_e = -1$ but the non-radiative decay rate is higher in the $m_e = -1$ state. The alignment of the magnetic field with the defect symmetry axis is important for this mechanism to proceed and the degree of polarization is expected to decrease monotonically with the field strength in this direction which is held well below 500 G in these experiments. So by aligning a static magnetic field along the NV axis, the electron as well as the nuclear spin of the ^{14}N atom can be polarized to a remarkable degree (cf. Figure 9). The resulting concentration of most of the population in one spin state $|m_e, m_n\rangle$ is of great importance for quantum information processing experiments. The preparation of a pure or nearly pure state is often a desirable goal. When the spin state is already highly polarized to begin with, less work has to be invested in achieving that goal. Although there are other methods, this polarization procedure is very easy and useful.

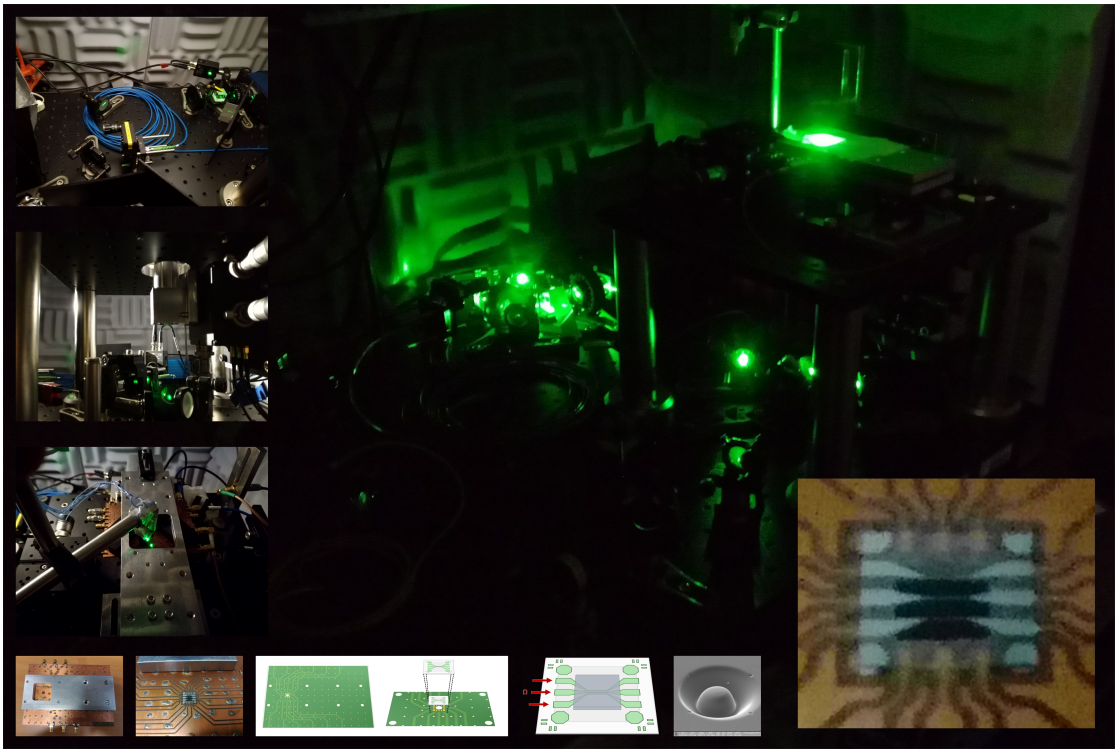

Figure 3: Photographs of the experimental setup. The diamond sample is placed on the wires on a thin glass window attached to a printed circuit board (lower left corner photos), mounted onto a translation stage seen on top of the table in the upper right corner. The diamond is located at the brightly glowing spot illuminated by the laser. A photo of the focusing lens that is etched onto the diamond's surface is also displayed.

3 Experimental Setup

3.1 Mechanics

The thin diamond sits on a wired glass window attached to a printed circuit board (PCB) which, in turn, is mounted on a translation stage. A vibration-isolated table holds this translation stage on top of it, another one for a bar magnet, and a third one moves an optical objective on the lower side of the tabletop. The breadboard to which the table and the rest of the optical setup is affixed is located inside of a wooden box with acoustic foam on the inside. The box can be closed completely, isolating the setup also from air flows in the room. The breadboard and the box reside on a larger table that is pneumatically vibration-isolated. It is used to kill off longer vibration modes. A construct of aluminium bars and plastic boards framed above the table holds most of the electronic devices as well as the computer that collects and monitors the data.

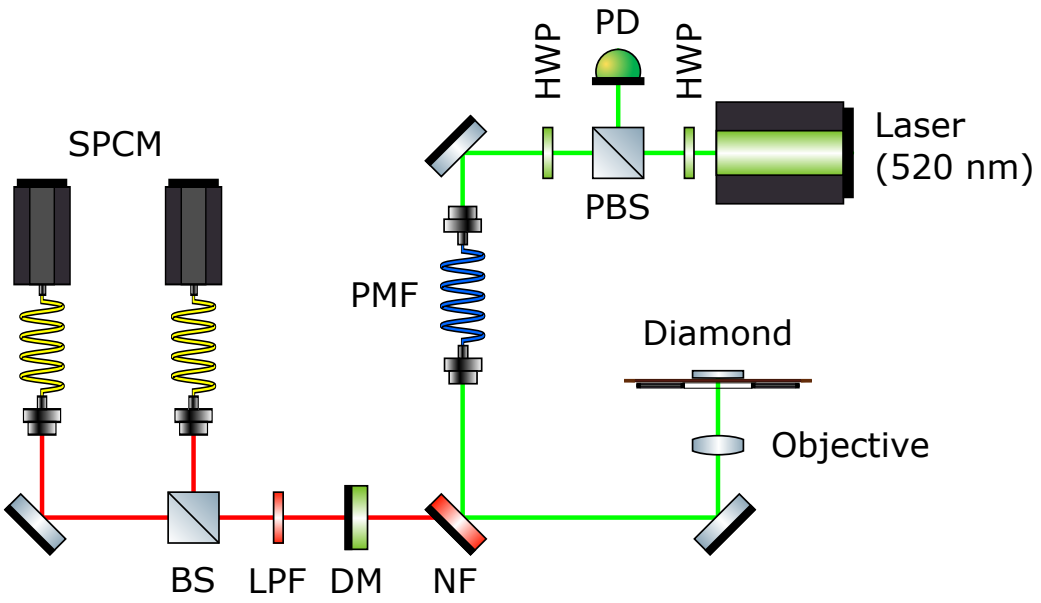

Figure 4: Schematics of the optical setup. A $520\ nm$ laser is sent through two half-wave plates (HWP) and a polarizing beam splitter (PBS) where the polarization of the beam is determined. The second output of the PBS is directed towards a photodiode (PD) that monitors laser power. The beam is then directed through a polarization-maintaining fiber (PMF) impinging on a notch filter (NF) after it. Then the beam is focussed onto a spot inside the diamond lying on a wired glass window. The red fluorescence of the NV center then passes through the NF, a dichroic mirror (DM) and a longpass filter (LPF). A beamsplitter divides the signal up onto two single photon counting modules (SPCM) connected by telecom-wavelength, single-mode fibers.

3.2 Optics

The goal of the optical setup is to uniformly excite the NV center with a green laser and collect red fluorescence photons as a signal. To this end, the laser beam polarization is adjusted before it is sent onto the diamond through an optical fiber and a focussing objective as seen in Figure 4. On the way back, all the photons meet a notch filter, a dichroic mirror and a longpass filter. These select out the right photon wavelengths. A beamsplitter then splits the signal onto the two avalanche photo diodes (APD) integrated in single photon counting modules (SPCM). The diamond rests on an optically transparent window and the objective can be moved as to focus on the right depth and transversal position. The whole optical setup resembles the concept of a confocal microscope. A software-controlled piezo stage is used to position the objective on the submicrometer scale to keep the focus on the NV center over a longer period of time.

3.3 Electronics

3.3.1 Applying an Oscillating Field

An oscillating magnetic field is applied to the NV center by sending an oscillating current over the wires on the glass window and beneath the diamond. This field couples to the spins in the NV center and can induce Rabi oscillations, the theoretical underpinning of which is covered in the next section. Thereby controlled manipulations of the electron and nuclear spins can be achieved by simply sending electronic pulses.

3.3.2 Microwave and Radio-Frequency Sources

Several voltage controlled oscillator boards are used as microwave sources to generate signals for steering electron spin state manipulations at different frequencies in a short period of time. They generate a continuous signal. The frequency is set by microcontrollers connected to each board and the PC. Pulses are created by sending pulses to the switches that open the signal line in the desired time window. The nuclear spin states of the $^{14}\mathrm{N}$ nucleus are addressed with radio-frequency signals produced by a frequency generator with arbitrary waveform function. The waveform itself is triggered by a pulse sent to the frequency generator. Both signal types have to be amplified in order to obtain the necessary powers to produce observable effects on the spin states.

3.3.3 Pulsing, Counting and Temperature Stabilization

The pulses are generated by a single-board computer (SBC) programmed to play pulse sequences in a continuous loop after they are handed over from the computer. The pulses coming from these channels steer the laser to generate laser pulses, open the gates for the signals coming from the APDs and going to the counting device, open switches to generate microwave pulses, trigger radio-frequency waveforms and act as synchronization markers for data processing purposes. The switches are known to have a rise time of up to 10 ns while the raw pulses are slightly faster. A time tagger unit is utilized for the purpose of assigning time-stamps to single photons as the signal arrives. Its signal is fed directly into the computer of the experimental setup. The magnet on top of the diamond is equipped with a thermoelectric cooler (TEC) as well as a temperature sensor that stabilizes the magnet's temperature for a constant field.

3.3.4 Software

The control of the instruments and the data acquisition and saving is done by LabVIEW. In addition, an interface to Python codes is implemented that writes pulse sequences onto the SBC every time a new kind of measurement is done. As mentioned above, an important tracking routine is implemented that keeps the laser focussed on the NV.

4 Theoretical Aspects

4.1 Two-Level Systems and Rabi Oscillations

For a general system with two energy levels described by the states $|0\rangle$ and $|1\rangle$ separated by an energy $E = \hbar\omega_0$ to which an oscillating field with angular frequency ω is applied, the Hamiltonian can be written as

$$\hat{H} = \frac{\hbar\omega_0}{2}\hat{\sigma}_z + \hbar g\cos(\omega t + \phi)\vec{n}\cdot\vec{\hat{\sigma}}, \tag{1}$$

where $\vec{\hat{\sigma}} = (\hat{\sigma}_x, \hat{\sigma}_y, \hat{\sigma}_z)$ are Pauli matrices, $\vec{n} = (n_x, n_y, n_z)$ is a normalized vector pointing in the direction of the positive field and g can be seen as the coupling constant. By transforming to a rotating frame, one can achieve a simplification that allows an approximate analytical treatment of the problem. To do this, a unitary operator

$$\hat{U} = e^{i\frac{\omega t}{2}\hat{\sigma}_z} \tag{2}$$

is applied to the state $|\psi\rangle$ of the system which results in a new state $|\Psi\rangle = \hat{U}|\psi\rangle$. The Hamiltonian is transformed by looking at the Schrödinger equation.

$$\begin{aligned} i\hbar\frac{\partial}{\partial t}|\Psi\rangle &= i\hbar\frac{\partial}{\partial t}(\hat{U}|\psi\rangle) = i\hbar(\dot{\hat{U}}|\psi\rangle + \hat{U}\frac{\partial}{\partial t}|\psi\rangle) \\ &= i\hbar\dot{\hat{U}}\hat{U}^\dagger|\Psi\rangle + \hat{U}\hat{H}|\psi\rangle = i\hbar\dot{\hat{U}}\hat{U}^\dagger|\Psi\rangle + \hat{U}\hat{H}\hat{U}^\dagger|\Psi\rangle \\ &= (i\hbar\dot{\hat{U}}\hat{U}^\dagger + \hat{U}\hat{H}\hat{U}^\dagger)|\Psi\rangle = \hat{H}_{RF}|\Psi\rangle \end{aligned}$$

This means that the Hamiltonian in the rotating frame comprises a term with a time derivative of the unitary operator.

$$\hat{H}_{RF} = \hat{U}\hat{H}\hat{U}^\dagger + i\hbar\dot{\hat{U}}\hat{U}^\dagger \tag{3}$$

Without loss of generality, the y-component n_y of the field can be set to zero for simplification. The commutation rules of the Pauli matrices and the algebraic identity

$$e^{\hat{X}}\hat{Y}e^{-\hat{X}} = \hat{Y} + [\hat{X},\hat{Y}] + \frac{1}{2!}\big[\hat{X},[\hat{X},\hat{Y}]\big] + \frac{1}{3!}\Big[\hat{X},\big[\hat{X},[\hat{X},\hat{Y}]\big]\Big] + ... \tag{4}$$

for operators can be used to get an expression for the Hamiltonian. The result is

$$\begin{aligned} \hat{H}_{RF} =& \frac{\hbar(\omega_0-\omega)}{2}\hat{\sigma}_z + \hbar g n_z\cos(\omega t+\phi)\hat{\sigma}_z \\ &+ \hbar g n_x\cos(\omega t+\phi)\big(\cos(\omega t)\hat{\sigma}_x - \sin(\omega t)\hat{\sigma}_y\big). \end{aligned} \tag{5}$$

Simplifying the trigonometric functions in the last term through exponentials yields

$$\frac{\hbar g n_x}{2}\Big[\big(\cos(2\omega t+\phi)+\cos(\phi)\big)\hat{\sigma}_x+\big(\sin(2\omega t)-\sin(\phi)\big)\hat{\sigma}_y\Big] \tag{6}$$

The counterrotating components of the field produce terms in the Hamiltonian that oscillate with twice the frequency of the field. These are discarded in what is canonically known as the rotating wave approximation (RWA). It applies well for weak coupling, i.e. $g \ll \omega_0$, and a signal near resonance, i.e. $\omega \approx \omega_0$ [20]. The second term in the Hamiltonian in Equation 5 produces a rapid oscillation of the eigenvalues of $\hat{H}_{RF}$ and is also neglected. Thus we gain a Hamiltonian that, conveniently, can be written as

$$\hat{H}_{RF} = \frac{\hbar}{2}\vec{m}\cdot\vec{\hat{\sigma}}, \tag{7}$$

where $\vec{m} = (\delta, \Omega\cos(\phi), \Omega\sin(\phi))$, $\delta = \omega_0 - \omega$ and $\Omega = g n_x$. The time evolution operator emerging from this Hamiltonian is a rotation about $\vec{m}$ on the Bloch sphere.

$$\hat{U}_{RF} = e^{i\frac{\vec{m}\cdot\vec{\hat{\sigma}}t}{2}} \tag{8}$$

The rotation frequency can be determined by normalizing $\vec{m}$.

$$\|\vec{m}\| = \sqrt{\Omega^2+\delta^2} \tag{9}$$

So it is the phase and the detuning of the applied field, rather than its orientation, that determine the rotation axis. $\Omega' \equiv \|\vec{m}\|$ is sometimes called the generalized Rabi frequency, Ω just Rabi frequency and δ is the detuning. Another important insight from this deduction is the population transfer that occurs when starting with a state $|0\rangle$ and applying a detuned field for a time t. It can be obtained by using the identity

$$\hat{U}_{RF} = \cos\left(\frac{\Omega' t}{2}\right)\hat{\mathbb{1}} - i\sin\left(\frac{\Omega' t}{2}\right)\frac{\vec{m}\cdot\vec{\hat{\sigma}}}{\Omega'} \tag{10}$$

and squaring the amplitude.

$$\begin{aligned} P_{10}(t) =& |\langle 1|\,\hat{U}_{RF}\,|0\rangle|^2 = |\langle 1|\left[\cos\left(\frac{\Omega' t}{2}\right)\hat{\mathbb{1}} - i\sin\left(\frac{\Omega' t}{2}\right)\frac{\vec{m}\cdot\vec{\hat{\sigma}}}{\Omega'}\right]|0\rangle|^2 \\ =& \frac{\Omega}{\Omega'^2}\sin\left(\frac{\Omega' t}{2}\right)^2 = \frac{1}{1+(2dT)^2}\sin\left(\sqrt{\left(\frac{\pi}{T}\right)^2+(2\pi d)^2}\,\frac{t}{2}\right)^2, \end{aligned} \tag{11}$$

where $d = \frac{\delta}{2\pi}$ is the detuning as ordinary frequency and $T = \frac{\pi}{\Omega}$ is the duration of a π-pulse at $d = 0$. In this work, the relevant ratios are typically $\frac{\Omega}{\omega_0} \ll 0.005$ and $\frac{\delta}{\omega_0} \ll 0.001$, thus justifying the above approximations for these purposes. The concept of considering only two isolated energy levels as an approximation for a clearly more complex problem is very important and is used throughout this entire thesis. For a discussion of the relevance of Equation 11 for resonance shapes refer to Section 5.2.

4.2 Multiple Energy Levels

When the off-resonant driving between additional levels is strong or when crossing effects between levels have to be considered, it becomes necessary to extend the Hilbert space dimensionality of the employed model. A few examples of the used models are given below. The method of obtaining the dynamics of the system is, in each case, a numerical solution of the Schrödinger equation. The following models find application.

4.2.1 Single Qutrit

The Hamiltonian for a single qutrit in an oscillating field can be written as

$$\hat{H} = \sum_{i=1}^{3} E_i \left|i\right\rangle \left\langle i\right| + \Omega \cos(\omega t + \phi)\hat{S}_x, \tag{12}$$

where

$$\hat{S}_x = \begin{pmatrix} 0 & 1 & 0 \\ 1 & 0 & 1 \\ 0 & 1 & 0 \end{pmatrix} \tag{13}$$

is a spin matrix. This model is used in Section 10 where pulse sequences are calculated for the preparation and projection of certain spin states of the Nitrogen nucleus.

4.2.2 Two Qubits

For a model involving only two electron and two nuclear spin states, respectively, the following Hamiltonian is put to use:

$$\hat{H} = \sum_{i=1}^{4} E_i \left|i\right\rangle \left\langle i\right| + \Omega \cos(\omega t + \phi)(\hat{\sigma}_x \otimes \hat{\mathbb{1}} + \hat{\mathbb{1}} \otimes \hat{\sigma}_x). \tag{14}$$

In Section 7, partly, one nuclear and one electron spin state play a negligible role. For comparison with the data and the two-level model, this Hamiltonian is used.

4.2.3 Two Qutrits

This is the Hamiltonian describing all the relevant spin states. It is computationally expensive but takes care of all the relevant processes that can occur during the application of fields. It has the following form

$$\hat{H} = \sum_{i=1}^{9} E_i \left|i\right\rangle \left\langle i\right| + \Omega \cos(\omega t + \phi)(\hat{S}_x \otimes \hat{\mathbb{1}} + \hat{\mathbb{1}} \otimes \hat{S}_x), \tag{15}$$

where S_x is the spin matrix described above. While for complicated or long pulse sequences it can cost a lot of calculation time, it is a very powerful model that effortlessly keeps track of all the phases that are encoded in a nine-dimensional quantum system.

4.3 Decoherence

A system in a coherent quantum state $|\psi\rangle_S$ that lives in Hilbert space $\mathcal{H}_S$ can lose its coherence over time by virtue of interactions with its environment. If the interacting environment can be modelled in terms of a Hamiltonian $\hat{H}_E$ that acts on states in Hilbert space $\mathcal{H}_E$, then the interaction Hamiltonian $\hat{H}_I$ lives in a Hilbert space $\mathcal{H}_I = \mathcal{H}_S \otimes \mathcal{H}_E$ and the decoherence process can be described as a unitary evolution of the combined state of system and environment $|\psi\rangle = |\psi\rangle_S \otimes |\psi\rangle_E$. Similar to the process of entangling quantum systems, the isolated system under consideration loses its property of being a quantum system or having a quantum state all by itself. In stark contrast to deliberately entangling systems in a controlled manner where information that was encoded in the phase relationships between basis states is relocated to describing the phase relations of the larger system, when decoherence occurs, we usually talk about an uncontrolled process that just disperses the phases into the surrounding. The topic of decoherence is a fascinating and deep one. It connects directly to the measurement problem, the question of whether macroscopic objects can in principle be in a quantum superposition and the encompassing question of how the manifest image that we see of the world emerges from the quantum world of coherent states. It is also one of the best tools that we have when targeting the question about what probabilities, in fact, describe and what the quantum state actually is. After all, either everything we see comes into form by the mere process of interaction, or, there isn't even anything else than interaction. No one knows, yet. Describing decoherence in a mathematically rigorous way is something of a paradox. If the surrounding was to be described with an exact Hamiltonian, then, probably, it would be already controllable experimentally and should be considered part of the system, not the environment. What is a measurement?

4.3.1 Measurements and Born's Rule

Now, when we perform a measurement on a quantum system, we can get any orthogonal basis state of the observable $\hat{O}$ corresponding to the quantity that is measured as an outcome, but nothing else. Why is that so? Assume that we have two states $|\psi_1\rangle$ and $|\psi_2\rangle$ which are measured by an apparatus that is in an initial state $|A\rangle_0$. Under the assumptions that measurements on the same state give the same result and that $|\psi_1\rangle$ and $|\psi_2\rangle$ were already measured, the following equalities must hold:

$$\begin{aligned} |\psi_1\rangle \otimes |A_0\rangle &= |\psi_1\rangle \otimes |A_{\psi_1}\rangle \\ |\psi_2\rangle \otimes |A_0\rangle &= |\psi_2\rangle \otimes |A_{\psi_2}\rangle \,. \end{aligned} \tag{16}$$

When we take the scalar product of the two states, we get

$$\langle\psi_1|\psi_2\rangle \otimes \langle A_0|A_0\rangle = \langle\psi_1|\psi_2\rangle \otimes \langle A_{\psi_1}|A_{\psi_2}\rangle \,. \tag{17}$$

This equation tells us that if we want to have different outcomes, i.e. $|\langle A_{\psi_1}|A_{\psi_2}\rangle| \neq 1$, the measured states have to be orthogonal as $\langle A_0|A_0\rangle = 1$. Thus it follows that states that ought to give definite measurement results have to be orthogonal [21]. The same is true for general decoherence processes. Distinguishable events, i.e. distinguishable states of the environment, can only be caused by orthogonal states of the system if its state is to remain the same. By similar considerations one can go on to prove Born's rule describing the probabilities of measurement outcomes, as was done by Zurek [22]. The explanation of why measurements have to be described in terms of probabilities reduces to the statement that the system doesn't have a definitive state as only the composite system including the interacting environment or apparatus has a pure state.

4.3.2 The Lindblad Equation

Independently found in 1976 by Lindblad [23] and Gorini, Kossakowski and Sudarshan [24], the Lindblad or GKSL equation describes the interaction of a quantum system with its environment. It is derived from a unitary evolution of the bigger system including the interacting environment, as described above, and it takes the form

$$\dot{\hat{\rho}} = -\frac{i}{\hbar}[\hat{H}, \hat{\rho}] + \sum_{m,n=1}^{N^2-1} h_{mn}\left(\hat{A}_m \hat{\rho} \hat{A}_n^\dagger - \frac{1}{2}\left\{\hat{A}_m \hat{A}_n^\dagger, \hat{\rho}\right\}\right), \tag{18}$$

where $\hat{\rho}$ and $\hat{H}$ and are the density matrix and Hamiltonian of the system, $\hat{A}_m$ is an operator basis and N is the Hilbert space dimension of the system. The matrix h is a positive semidefinite matrix modelling the interaction. The most general linear evolution that preserves the unit trace and Hermiticity of the density matrix and satisfies the condition of complete positivity is the Lindblad equation. Strictly speaking, however, it does not apply in cases where the initial state involves correlations between system and environment as the complete positivity constraint is no longer valid [25]. This equation can be seen as an explanation of the mechanism by which orthogonal states are discriminated during the measurement process as argued by Weinberg [26]. Conversely, any process that transforms the initial quantum state of the system to a completely mixed state can be seen as a measurement. While the information about the system's state may not end up being effectively readable for an observer, again, the mere entanglement with the environment produces Born's rule for the probabilities of it being in a certain one. This analogy is utilized in Section 9.1. There is one distinction because in a real measurement the phase information is expected to be diffused irreversibly across a wider region of spacetime. However, it seems that this is more of a practical difference than a fundamental one. The spin decoherence phenomena observed will be treated rather superficially because an exact description of it is simply not necessary. But the connection to the Lindblad equation is an indisputable mathematical fact that should be mentioned in light of the overall project's theme.

4.4 Entanglement

4.4.1 Peres-Horodecki Criterion

The density matrix of a bipartite system of qubits A and B

$$\hat{\rho} = \sum_{i,j,k,l=1}^{2} p_{ijkl} \left|i\right\rangle \left\langle j\right| \otimes \left|k\right\rangle \left\langle l\right| \tag{19}$$

is separable if and only if the partially transposed matrix $\hat{\rho}^{T_B}$ is positive, i.e. has non-negative eigenvalues [27, 28]. The partially transposed matrix can be obtained by changing the coefficients in Equation 19 from p_{ijkl} to p_{ijlk}. It can be easily seen that $\hat{\rho}^{T_A} = \left(\hat{\rho}^{T_B}\right)^T$. Therefore it doesn't matter onto which subsystem the transposition is applied. For higher dimensions it is only a necessary but not a sufficient condition and a density matrix satisfying it can still describe what is known as bound entanglement.

4.4.2 Negativity

If the partially transposed matrix of the composite system is negative, however, we know that there is entanglement for any dimension d of the subsystems. The negativity

$$\mathcal{N} = \sum_{i=1}^{d} \frac{|\lambda_i| - \lambda_i}{2}, \tag{20}$$

defined as the absolute sum of the negative eigenvalues λ_i of $\hat{\rho}^{T_A}$ is a possible measure for entanglement [29]. A noteworthy property is convexity $\mathcal{N}(\sum_i p_i\hat{\rho}) \leq \sum_i p_i\mathcal{N}(\hat{\rho}_i)$. The two cases of bipartite qubit and bipartite qutrit entanglement are particularly relevant for the conducted experiments described in Section 7 where the goal is to produce maximally entangled spin states with negativities of $\frac{1}{2}$ and 1, respectively.

4.4.3 Entanglement Entropy

While for mixed states the above may be more adequate, the von Neumann entropy

$$S(\hat{\rho}) = -\mathrm{Tr}[\hat{\rho}\ln(\hat{\rho})] \tag{21}$$

of a density matrix $\hat{\rho}$ introduced by von Neumann [30] can also be used to quantify entanglement of pure states. Written in the eigendecomposition, Equation 21 gives

$$S(\hat{\rho}) = -\sum_{i=1}^{d} \lambda_i \ln(\lambda_i). \tag{22}$$

The entanglement entropy is calculated by taking the von Neumann entropy of the reduced density matrix of any one of the two subsystems by tracing over the other

$$\hat{\rho}_A = \mathrm{Tr}_B[\hat{\rho}] = \sum_i \langle i_B| \hat{\rho} |i_B\rangle \tag{23}$$

for subsystem A, where $|i_B\rangle$ are a set of basis vectors for Hilbert space B, and likewise for subsystem B. Indeed, it can be shown that the eigenvalues of the two reduced density matrices are the same and thus the entanglement entropy is (see section A.1 of the Appendix for a proof). The idea is to measure the randomness in the reduced state to reveal that (some of) the information is distributed on the composite state of the system and thereby quantify mutual entanglement. The von Neumann entropy is

- concave, i.e.
$$S\Big(\sum_i p_i \hat{\rho}_i\Big) \geq \sum_i p_i S(\hat{\rho}_i) \tag{24}$$
for any set of weights p_i with $\sum_i p_i = 1$ and density matrices $\hat{\rho}_i$.
- bounded above by $\ln(d)$, where d is the Hilbert space dimension.
- invariant under unitary transformations of the density matrix because
$$\big|\hat{U}\hat{\rho}\hat{U}^\dagger - \lambda\hat{\mathbb{1}}\big| = \big|\hat{U}\hat{\rho}\hat{U}^\dagger - \lambda\hat{U}\hat{U}^\dagger\big| = \big|\hat{U}(\hat{\rho} - \lambda\hat{\mathbb{1}})\hat{U}^\dagger\big| = \big|\hat{\rho} - \lambda\hat{\mathbb{1}}\big|. \tag{25}$$
Thus the eigenvalues and the von Neumann entropy are the same for $\hat{\rho}$ and $\hat{U}\hat{\rho}\hat{U}^\dagger$. This can be used to justify ignoring phases when they are unknown. Two phase shift unitaries can be combined to transform the state by applying
$$\hat{U}_A \otimes \hat{U}_B = \sum_{mn} e^{i(\phi_m + \phi_n)} |m\rangle\langle m| \otimes |n\rangle\langle n| \tag{26}$$
whereby all (two qubits) or six of eight (two qutrits) phases can be eliminated.

These properties are used for estimating the degree of entanglement in Section 7.4.

4.5 Leggett-Garg Inequality

In 1985, Leggett and Garg tried to develop a small set of assumptions that summarize how we usually think of the macroscopic world [31]. They derived an inequality that is similar to, for instance, a Bell inequality but instead of measuring the state of an entangled system in different bases of the correlated parts, the state of a single system is measured at different times t_i to show not an incompatibility of quantum mechanics with local realism but with what they termed macroscopic realism. For the derivation of the inequality one imagines a quantum system with two possible states corresponding to the two measurement outcomes $Q = \pm 1$. Three measurements are made at times t_1, t_2 and t_3, and the correlations $C_{ij} = \sum_{r=1}^{N} \frac{Q_i^r Q_j^r}{N}$ between the outcomes Q_i and Q_j after Nmeasurements can be shown to satisfy the inequality $K = C_{12} + C_{23} - C_{13} \leq 1$.

This, however, is only true for theories satisfying the following two conditions:

- Macroscopic realism per se: A macroscopic system with two or more macroscopically distinct states available will at all times be in one or the other state.
- Noninvasive measurability: It is possible, in principle, to determine the state of the system with arbitrarily small perturbation on its subsequent dynamics.

A direct extrapolation of quantum mechanics to the macroscopic level denies this, as written by the authors. While the goal of the experiments here is not a numeric violation of this Leggett-Garg inequality, a line of argument is provided by which the mere measurement by an independent apparatus necessarily influences the state of the system and after that, the effect of such an intervention is demonstrated in Section 9.

4.6 PBR Theorem

Named after Matthew F. Pusey, Jonathan Barrett and Terry Rudolph [32], the PBR theorem states that models in which the quantum state is interpreted as mere information about an objective physical state of a system cannot reproduce the predictions of quantum theory. The argument by which the authors arrive at this conclusion is as follows. In general, the whole discussion about the quantum state either representing knowledge (epistemic models) or real physical states (ontic models) starts at the assumption that there is a physical state, either the quantum state or some underlying and more fundamental concept [33]. A probability distribution over the parameters characterizing this physical state is ascribed to every quantum state. Thereby a mathematical correspondence is established that allows for further investigations of the topic. An ontic model for the quantum state is typically defined as one where the probability distributions of different quantum states do not overlap at all whereas in an epistemic model they can. If the distributions overlap, it cannot be said that the quantum state is ontic as two different quantum states are then compatible with all the physical states in the overlap region. To see how the PBR theorem emerges, one is to imagine the independent preparation of two systems, each in either of two states, namely $|0\rangle$ or $|+\rangle = \frac{1}{\sqrt{2}}(|0\rangle + |1\rangle)$. The two systems are then brought together and are jointly measured in the following entangled basis involving a third state $|-\rangle = \frac{1}{\sqrt{2}}(|0\rangle - |1\rangle)$:

$$
\begin{aligned}
|\xi_1\rangle &= \frac{1}{\sqrt{2}}(|0\rangle \otimes |1\rangle + |1\rangle \otimes |0\rangle), \\
|\xi_2\rangle &= \frac{1}{\sqrt{2}}(|0\rangle \otimes |-\rangle + |1\rangle \otimes |+\rangle), \\
|\xi_3\rangle &= \frac{1}{\sqrt{2}}(|+\rangle \otimes |1\rangle + |-\rangle \otimes |0\rangle), \\
|\xi_4\rangle &= \frac{1}{\sqrt{2}}(|+\rangle \otimes |-\rangle + |-\rangle \otimes |+\rangle).
\end{aligned}
\tag{27}
$$

Each outcome gives definite proof that the composite system was not in the state $|0\rangle \otimes |0\rangle$, $|0\rangle \otimes |+\rangle$, $|+\rangle \otimes |0\rangle$ or $|+\rangle \otimes |+\rangle$, respectively. Under the assumption that the two states $|0\rangle$ and $|+\rangle$ share an overlap region in their corresponding probability distributions over the physical state, one arrives at a contradiction. The non-zero probability of actually having the same physical state when the quantum states $|0\rangle$ or $|+\rangle$ are prepared is incompatible with what quantum theory dictates the outcomes should be. This thought experiment is generalizable to all states and Hilbert space dimensions as it can be repeated with two states $|\psi_1\rangle = \cos(\frac{\theta}{2})\,|0\rangle + \sin(\frac{\theta}{2})\,|1\rangle$ and $|\psi_2\rangle = \cos(\frac{\theta}{2})\,|0\rangle - \sin(\frac{\theta}{2})\,|1\rangle$ and every pair of states can be written in this form with orthogonal states $|0\rangle$ and $|1\rangle$ by simply rearranging the equations. The parameter $\theta \in [0, \frac{\pi}{2}]$ covers all values for the overlap between $|\psi_1\rangle$ and $|\psi_2\rangle$. The contradiction arises when n systems are prepared in either $|\psi_1\rangle$ or $|\psi_2\rangle$, where n is the Hilbert space dimension, and measured in an entangled basis that is constructed in analogy to the two-dimensional case to rule out one product state per outcome. Thus the theorem.

4.7 Distinguishability of States

Strictly speaking, the PBR theorem assumes what is known as preparation independence. While from the quantum mechanics side this is unproblematic because every possible pair of states is considered, there is a possibility of the underlying physical states being correlated in some way. Hence one could argue that it only applies for a subspace of physical states of the composite system. A more general approach [34] simply states that the probability of distinguishing two states as described by quantum mechanics P_Q strictly has to be less or equal than the probability of distinguishing the two corresponding probability distributions P_C. Introducing the absolute value of an operator defined as $|\hat{\rho}| = \sqrt{\hat{\rho}^\dagger \hat{\rho}}$, the trace distance between density matrices $\hat{\rho}$ and $\hat{\sigma}$

$$D(\hat{\rho}, \hat{\sigma}) = \frac{1}{2}\mathrm{Tr}|\hat{\rho} - \hat{\sigma}| \tag{28}$$

can be used to get an expression for the quantum probability. The probability of being able to distinguish two states by measuring the best choice of state corresponding to a projector $\hat{P}$ is closely related to the trace distance between the states, as it holds that

$$D(\hat{\rho}, \hat{\sigma}) = \max_{\hat{P}} \mathrm{Tr}\big[\hat{P}(\hat{\rho} - \hat{\sigma})\big]. \tag{29}$$

This is proved by decomposing $\hat{\rho} - \hat{\sigma}$ into positive operators with orthogonal supports

$$\hat{\rho} - \hat{\sigma} = \hat{U}\hat{D}\hat{U}^\dagger = \hat{U}(\hat{D}^+ + \hat{D}^-)\hat{U}^\dagger = \hat{U}(\hat{D}^+ - \hat{\tilde{D}}^-)\hat{U}^\dagger = \hat{Q} - \hat{S}, \tag{30}$$

where $\hat{D}$ is a diagonal matrix with the eigenvalues of $\hat{\rho} - \hat{\sigma}$, $\hat{D}^+$ ($\hat{D}^-$) contains all positive (negative) eigenvalues of $\hat{D}$, $\hat{\tilde{D}}^- = -\hat{D}^-$ and $\hat{Q}$ and $\hat{S}$, by construction, are positive operators with orthogonal supports, i.e. they have positive eigenvalues and eigenvectors corresponding to the non-zero eigenvalues that are mutually orthogonal.

To compute the square root of a positive semidefinite and Hermitian matrix $\hat{\rho}$, one can, in general, work in the eigenbasis in which the square root of the matrix is given by $\hat{U}\sqrt{\hat{D}}\hat{U}^\dagger$, where $\hat{D} = \sum_i \lambda_i |\lambda_i\rangle \langle\lambda_i|$, again, is the diagonal matrix of $\hat{\rho}$ containing its eigenvalues λ_i. This can be seen by squaring it $\hat{U}\sqrt{\hat{D}}\hat{U}^\dagger\hat{U}\sqrt{\hat{D}}\hat{U}^\dagger = \hat{\rho}$. The square root of the diagonal matrix can be obtained by taking the square root of the eigenvalues $(\sum_i \sqrt{\lambda_i} |\lambda_i\rangle \langle\lambda_i|)^2 = \sum_i \lambda_i |\lambda_i\rangle \langle\lambda_i| = \hat{D}$. Hence by applying this lemma to $(\hat{\rho}-\hat{\sigma})^2$ instead of $\hat{\rho}$ and taking the positive root, we arrive at the following identity:

$$D(\hat{\rho}, \hat{\sigma}) = \frac{1}{2}\sum_i |\lambda_i^{\hat{\rho}-\hat{\sigma}}|, \tag{31}$$

where $\lambda_i^{\hat{\rho}-\hat{\sigma}}$ are the eigenvalues of $\hat{\rho}-\hat{\sigma}$. It also follows from the above decomposition that $|\hat{\rho}-\hat{\sigma}| = \hat{Q}+\hat{S}$ and because $\mathrm{Tr}(\hat{\rho}-\hat{\sigma}) = \mathrm{Tr}(\hat{Q}-\hat{S}) = 0$, we can write $D(\hat{\rho}, \hat{\sigma}) = \mathrm{Tr}(\hat{Q})$. With $\hat{P}$ projecting onto the support of $\hat{Q}$ such that $\mathrm{Tr}\big[\hat{P}(\hat{\rho}-\hat{\sigma})\big] = \mathrm{Tr}\big[\hat{P}(\hat{Q}-\hat{S})\big] = \mathrm{Tr}(\hat{P}\hat{Q}) = \mathrm{Tr}(\hat{Q})$, which can always be done, and then relaxing this constraint, we get the following chain of inequalities which leads back to Equation 29:

$$\mathrm{Tr}\big[\hat{P}(\hat{\rho}-\hat{\sigma})\big] = \mathrm{Tr}\big[\hat{P}(\hat{Q}-\hat{S})\big] \leq \mathrm{Tr}(\hat{P}\hat{Q}) \leq \mathrm{Tr}(\hat{Q}) = D(\hat{\rho}, \hat{\sigma}). \quad \square \tag{32}$$

It can then be deduced that the probability of being able to distinguish the states is just $\frac{1}{2}\big(1 + D(\hat{\rho}, \hat{\sigma})\big)$. For pure states, the trace distance reduces to the simple form

$$\delta(|\psi\rangle, |\phi\rangle) = D\big(\hat{\rho} = |\psi\rangle\langle\psi|, \hat{\sigma} = |\phi\rangle\langle\phi|\big) = \sqrt{1 - |\langle\psi|\phi\rangle|^2}. \tag{33}$$

This derives from the fact that, similar to Section 4.6, the two states can be written as $|\psi\rangle = \cos(\theta)|0\rangle + \sin(\theta)|1\rangle$ and $|\phi\rangle = \cos(\theta)|0\rangle - \sin(\theta)|1\rangle$ with $\theta \in [0, \frac{\pi}{4}]$. Their overlap is then $s = \langle\psi|\phi\rangle = \sin(2\theta)$ and $\hat{\rho}-\hat{\sigma} = \cos(2\theta)(|0\rangle\langle 0| - |1\rangle\langle 1|)$ which yields a trace distance of $D(\hat{\rho}, \hat{\sigma}) = \cos(2\theta) = \sqrt{1 - |\langle\psi|\phi\rangle|^2}$. So the probability P_Q is quantified. Now, the classical trace distance between two distributions $p(x)$ and $q(x)$

$$\delta_C(p, q) = \frac{1}{2}\int |p(x) - q(x)| dx \tag{34}$$

is used to calculate the probability $P_C = \frac{1}{2}(1 + \delta_C(p, q))$ of being able to distinguish the two probability distributions. From the concept of distinguishability one goes on to introduce overlaps $\omega_Q = 1 - \frac{P_Q}{2}$ and

$$\omega_C = 1 - \frac{P_C}{2} = \int \min\big[p(x), q(x)\big] dx. \tag{35}$$

The previous inequality for the probabilities of distinguishing states translates to $\omega_C \leq \omega_Q$ which states that the probability distributions describing the knowledge about the real physical states cannot possibly overlap more than the quantum states. Intuitively, this is just to say that one cannot have a disadvantage in discriminating states by knowing about the actual distributions of the physical variables instead of the quantum states. These concepts are important in discussing the ontology of the quantum state.

4.8 Quantification of "Epistemicness"

As it is highly interesting and worthwhile, a short summary of the principles for quantifying what can be called epistemicness of the quantum state is given. First it was shown that no maximally epistemic model where $\omega_Q = \omega_C$ can reproduce all the predictions of quantum mechanics for Hilbert space dimension $d \geq 3$ and that the lowest value for the ratio $\frac{\omega_C}{\omega_Q}$ over all possible states tends to zero for growing Hilbert space dimensions by using simple facts about mutually unbiased bases (for $d \geq 4$) [34]. In addition, Barrett, Cavalcanti, Lal and Maroney (BCLM) derived, using the Bonferroni inequality, a noise tolerant way of measuring an upper bound for the following quantity:

$$k(\psi, \phi) = \frac{\omega_C(\mu_\psi(\lambda), \mu_\phi(\lambda))}{\omega_Q(|\psi\rangle, |\phi\rangle)}, \ \langle\psi|\phi\rangle \neq 0, \tag{36}$$

where $\mu_\psi(\lambda)$ and $\mu_\phi(\lambda)$ are probability distributions over physical states λ corresponding to the states $|\psi\rangle$ and $|\phi\rangle$. The upper bound they found is best expressed as [35]

$$k_0 \leq \frac{1 + \sum_{i<j} A_{ij}}{\sum_i \omega_C(|c\rangle, |\psi_i\rangle)}, \tag{37}$$

where $k_0 = \min_j k(c, \psi_j)$. $A_{ij} = |\langle ij1|\psi_i\rangle|^2 + |\langle ij2|\psi_j\rangle|^2 + |\langle ij3|c\rangle|^2$ is called antidistinguishability, $|\psi_i\rangle$ are a set of n states, $|c\rangle$ is a reference state and $|ijk\rangle\langle ijk|$ with $i = 1...n, j = 1...i-1, k = 1, 2, 3$ are three projectors defining a positive-operator valued measure (POVM). Equation 37 can be easily generalized to mixed states [35]. So the upper bound for k_0 refers to the lowest overlap ratio between the reference $|c\rangle$ and one state in $|\psi_i\rangle$. In general, $k(\psi, \phi)$ can be seen as a measure of the epistemicness of the quantum state. Coming back to the distinguishability of states, the impossibility to discriminate two quantum states can be explained by the overlap of the corresponding probability distributions. But what happens if the quantum overlap and the classical overlap of these distributions are not equal like in the maximally epistemic model? In this case, the classical overlap, as argued above, has to be smaller and therefore the impossibility of discriminating non-orthogonal quantum states cannot be fully explained by the fact that the two quantum states are compatible with the same physical states. Some additional explanation would be needed. The maximally epistemic model, which is defined as $k(\psi, \phi) = 1 \ \forall \psi, \phi$, is the only one that does not have this problem. But it does have the disadvantage of having been disproved mathematically [34]. The other extreme case, which is the ontic model for the quantum state, has $k(\psi, \phi) = 0 \ \forall \psi, \phi$ and all the troubles of discriminating non-orthogonal quantum states are explained by quantum mechanics itself. It means that the quantum state seems to truly have an ontological quality in the sense that anything we describe with it can be seen as a unique state of affairs. Another implication is that the probabilistic nature of quantum mechanics is not reducible to talk about a lack of knowledge of a real physical state.

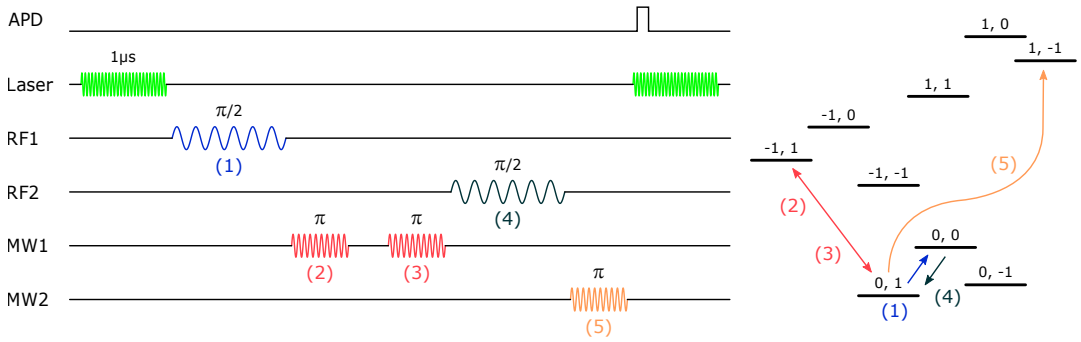

Figure 5: Pulse sequence for creating an entangled spin state. The first laser pulse intitializes the spins. The first radio-frequency (RF) pulse creates a superposition between two nuclear spin states. A subsequent microwave (MW) pulse plays the role of a CNOT gate on the electron spin. Then the state is recombined with a second, phase-shifted RF source and a second MW to read to another electron spin state. The switch for the APD signal is pulsed open for a brief time window right after the second laser pulse begins to collect spin-dependent fluorescence as described in Section 2.2. The energy levels in the term diagram on the right are explained further in Section 6.3.

5 Working with Spin States

5.1 Pulse Sequences

As an example for the measurement procedure, Figure 5 shows the pulse sequence for creating an entangled state between electron spin and the spin of the $^{14}\mathrm{N}$ nucleus. While the time scale is by no means in proportion, nor are any of the signal phases accurately represented, the diagram serves as an illustration for the order of operations that are applied. A first, 1 μs long laser pulse initializes the spins as described in Section 2.1. An initialization pulse as well as a second laser pulse for reading the state is employed in every pulse sequence. This is also true for the APD window created by a pulse to the proper switch that allows the spin-dependent fluorescence to pass to the counting device. To discriminate different nuclear spin states in the electron spin 0 state, often a microwave pulse is involved in the readout procedure that projects the population from a state with electron spin $m_e = 0$ and nuclear spin m_n, written as $|0, m_n\rangle = |0\rangle\,|m_n\rangle = |0\rangle \otimes |m_n\rangle$ to a state $|-1, m_n\rangle$ or $|1, m_n\rangle$. The electron spin state that best suits the rest of the pulse sequence is chosen, as the fluorescence only depends on the absolute value of the electron spin. This MW pulse is seen on the line termed MW2. To complete the example, between initialization and readout, an entangled state is produced by creating a superposition between two nuclear spin states by applying a $\pi/2$ pulse between two states. The term $\pi/2$-pulse refers to one quarter

of the period of a Rabi oscillation. A subsequent π-pulse transfers the population in only one of the two states two another state with different electron but the same nuclear spin. Thereby an entangled state of the sort $|\psi\rangle = \frac{1}{\sqrt{2}}(|m_{e,1}, m_{n,1}\rangle + |m_{e,2}, m_{n,2}\rangle)$, in the ideal case, is created. The details as well as the recombination process are described in Section 7 where the entanglement measurements are presented. In addition to the general scheme of measuring spins, two special types of measurements are of great importance to be able to work with spin states. These two methods are explored next.

5.2 Optically Detected Magnetic Resonance (ODMR)

Equation 11 gives a hint about what to expect when searching for resonances with spectroscopic techniques like the Optically Detected Magnetic Resonance (ODMR). ODMR is a technique that involves the application of a π-pulse of either a microwave or a radio-frequency signal. The frequency of the pulse is scanned through a certain interval of values to reveal resonances corresponding to energy levels or, rather, transition frequencies in the sense of energy differences divided by $\hbar$. The expected resonance shape, at least for high signal powers, involves a cardinal sine or sinc function, defined as $\mathrm{sinc}(x) = \frac{\sin(x)}{x}$. By setting $t = T$ in Equation 11, one arrives at this conclusion:

$$\begin{aligned} P_{10}(T) &= \frac{1}{1+(2dT)^2} \sin\left(\sqrt{1+(2dT)^2}\,\frac{\pi}{2}\right)^2 \\ &= \left(\frac{\sin\left(\sqrt{1+(2dT)^2}\,\frac{\pi}{2}\right)}{\sqrt{1+(2dT)^2}}\right)^2 \\ &= \left(\frac{\pi}{2}\right)^2 \mathrm{sinc}\left(\sqrt{1+(2dT)^2}\,\frac{\pi}{2}\right)^2. \end{aligned} \tag{38}$$

Indeed, this is the function describing the resonances seen in ODMR measurements. For small signal powers however, the overall broadening $2\sqrt{\Gamma^2+\Omega^2}$ (full width at half maximum) is dominated by the natural lifetime Γ^{-1} of the state, thus resulting in an approximately Lorentzian line shape [36]. The ODMR technique is used to measure the transition frequencies between spin states to be able to make any spin manipulations. The same principle applies for the electron spin as well as the nuclear spin. To be able to see the nuclear resonances, however, it is necessary to apply a microwave pulse that transfers the population from either the initial or the target nuclear spin state to another electron spin state with the same nuclear spin. As indicated in the last subsection, this is an often-applied method, e.g. for measurements involving only manipulations of the nuclear spin. Once the transition frequency is known, usually one wants to know the Rabi frequency for a certain signal power to be able to start manipulating the spin in a controlled manner. The next measurement that is introduced does exactly this job.

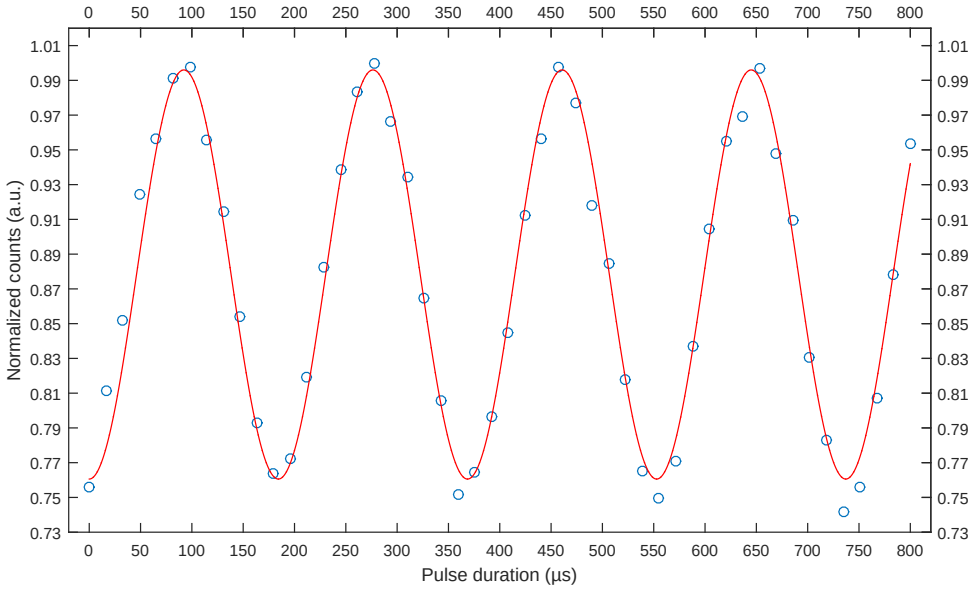

Figure 6: Nuclear Rabi measurement over several periods. The displayed oscillation has a Rabi frequency of Ω=(34.10±0.44) kHz, corresponding to a π-time of T=(92.14±0.12) μs, which lies in the typical range of values used in the experiments. Notice the apparent coherence time of arguably well over four periods for this Rabi frequency. This is a major characteristic when a signal of this coupling strength, or a slightly bigger one for that matter, is used to manipulate the nuclear spin over a time interval that is within these bounds, e.g. the experiments outlined in Section 10.

5.3 Rabi Measurement

Instead of varying the frequency of a signal pulse with a fixed duration, a Rabi measurement serves as a means by which the Rabi frequency of an interaction between the oscillating signal and the quantum spin is to be worked out. After the spin initialization, a pulse is applied to initiate a Rabi oscillation starting from a certain spin state and transferring its population to another. To measure the complete oscillation, a set of measurements is done in which the length of the relevant pulse is varied over the expected time for one or several periods of the Rabi oscillation. The resulting sinusoidal signal can then be used to extract the Rabi frequency. For nuclear spin states, again, a microwave pulse in the readout, cf. MW2 in Figure 5, has to be employed to get a handle on the actual population in the initial or target spin state. For an illustration of what an experimental result of such a procedure might look like, see Figure 6 which shows a nuclear Rabi oscillation with Rabi frequency $\Omega \approx$34 kHz or $f = \frac{\Omega}{2\pi} \approx$5.4 kHz. The sinusoidal character predicted by Equation 11 is typically found to agree extremely well in all cases where the assumptions for the two-level model are expected to apply.

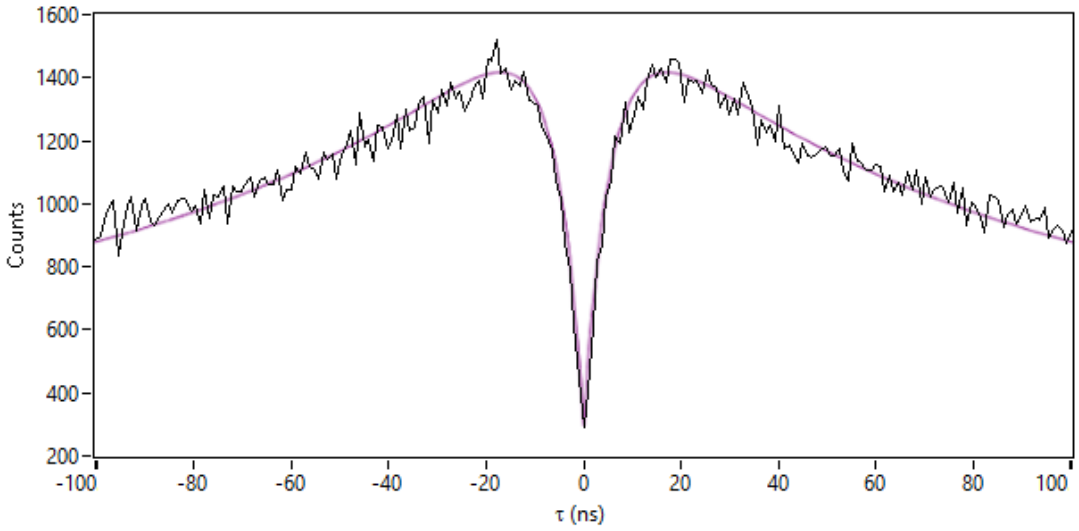

Figure 7: Photon antibunching indicating a single emitter, the nitrogen-vacancy center. The diagram shows the number of occurrences, or counts, of two photons arriving in the counting device with a delay time of τ (up to the width of the time bin). The gap in the middle stems from the finite lifetime of the excited spin states. While the NV is in its excited state, it will only emit a photon after a certain, characteristic time. For small delays, this process rarely occurs twice. A model function with two exponential decays [37] is used to show that $g^{(2)} < 0.5$ for the typically measured singal-to-noise ratios. This inference is used to provide proof that there is only one single NV center.

6 The Diamond

The diamond sample is equipped with a small lens etched onto its surface. To find out whether there really is only one NV center under it, the photons in the fluorescence signal emerging can be counted with a highly time-resolved counting device to calculate the second order intensity correlation function $g^{(2)}(\tau)$ which is defined by the function

$$g^{(2)}(\tau) = \frac{\left\langle \hat{a}^\dagger(0)\hat{a}^\dagger(\tau)\hat{a}(\tau)\hat{a}(0)\right\rangle}{\left\langle \hat{a}^\dagger\hat{a}\right\rangle^2}, \tag{39}$$

where $\hat{a}^\dagger$ and $\hat{a}$ are creation and annihilation operators of the field and $\langle ... \rangle$ indicates time averaging. This, however, has to be translated into quantities that can be computed from the data. As the counting device has a finite time resolution, the number of photons in this time window can only be either 0 or 1 and the same applies for the product of the number of photons at 0 and the number of photons at time τ. Hence $g^{(2)}(\tau)$, up to normalization, equates to the number of photon pairs with a delay τ. Figure 7 shows the result of such a statistic where photon antibunching can be seen.

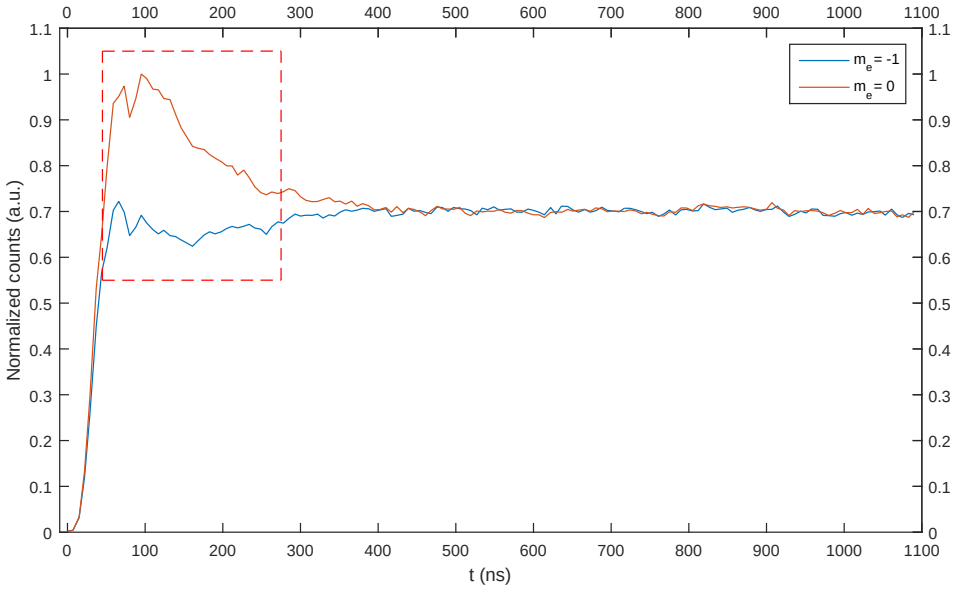

Figure 8: Fluorescence curve of the NV center. Depending on the electron spin m_e, the fluorescence over time differs in the first few hundred nanoseconds before an equal population state is established by the interaction with the laser. The difference in fluorescence indicated by the red box is the ultimate tool for reading out any spin state, including the result in Figure 6. The horizontal interval of the red box shows the time window chosen by maximizing the visibility or contrast, as explained in the text.

6.1 Fluorescence

To be able to distinguish any two spin states, it is necessary to filter out only a small piece of the fluorescence, as shown in Figure 8. The time window is chosen to maximize

$$V = \frac{r_0 - r_{-1}}{r_0 + r_{-1}},$$

the visibility, with r_{m_e} being the counts or the count rate of the state with electron spin m_e. A similar quantity, the contrast, is mainly used in the description of the data:

$$C = \frac{r_{-1}}{r_0}. \tag{40}$$

Alternatively, r_{-1} and r_0 can be substituted with the lowest and highest value of any function, respectively. While the window for the fluorescence signal, depicted as the box in Figure 8, should, actually, be determined by the relative error of the difference in counts assuming for example Poissonian distribution, it turns out to give no significantly different answer than simply maximizing the visibility or the contrast for that matter.

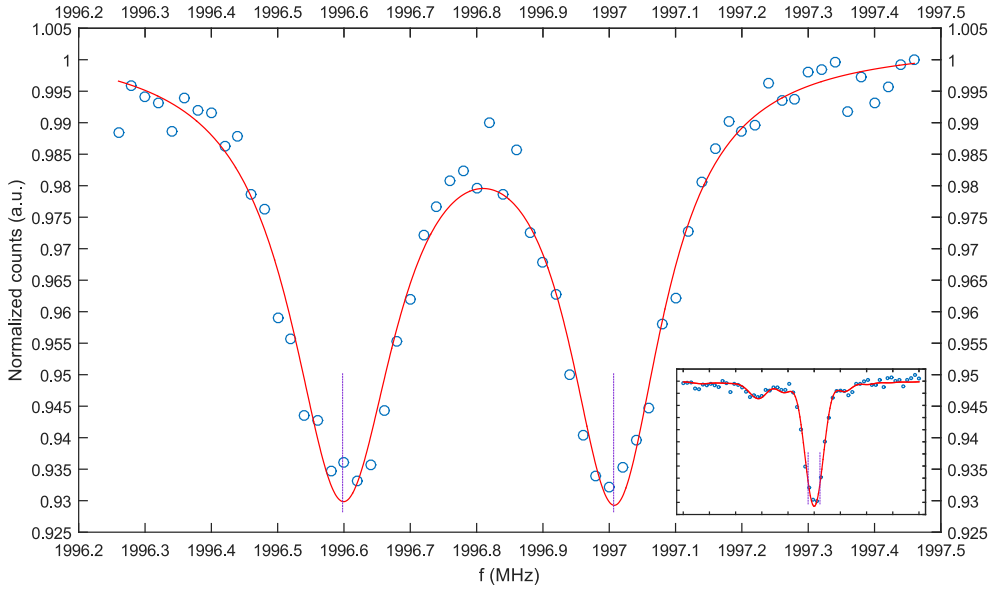

Figure 9: Energy level splitting due to a nearby ^{13}C atom in the diamond lattice. The diagram shows a low-power ODMR of an electron spin transition from $m_e = 0$ to $m_e = -1$ with a microwave pulse duration of 12.5 μs revealing a hyperfine splitting of 400.0±4.0 kHz. While it is not evident, it seems plausible to assume that this splitting stems from the hyperfine coupling of the electron spin to a nearby ^{13}C nucleus with spin $\frac{1}{2}$ and, apparently, no forbidden electron spin transitions at this lattice site and magnetic field magnitude [38]. The inset indicates the dips' positions in Figure 12.

6.2 Neighbouring ^{13}C Spin

An important feature of this particular NV center in this diamond sample is its hyperfine splitting due to the coupling to a neighbouring spin, presumably the spin of a ^{13}C nucleus. Figure 9 shows an ODMR revealing the splitting that results from a hyperfine coupling between electron spin and the spin of the ^{13}C nucleus. The splitting is close to 400 kHz which is at least consistent with the assumption of a ^{13}C atom being the cause of it [38]. The polarization seems to be very close to zero as the depths of the two dips agree to 97 % assuming a Gaussian distribution of the depths and using the overlap in Equation 35. The forbidden electron spin transitions described in previous works [38, 39] seem to be suppressed by the lattice site of the nucleus and the relatively weak magnetic field of approximately 300 Gauss. While no manipulation of its spin has been achieved and for electron spin manipulations with high microwave powers it is negligible, the ^{13}C nuclear spin plays a role in discussing the dephasing process of the electron spin. It also gives a lower bound for microwave powers in addressing the electron spin in an isolated manner. The utilization of this further qubit system

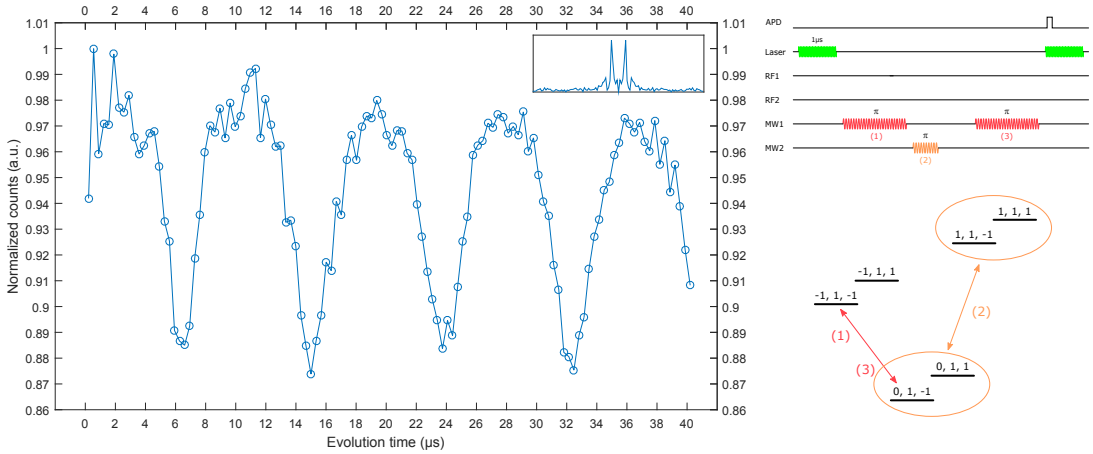

Figure 10: Oscillations between states of the ^{13}C nuclear spin in the electron spin state $m_e = -1$. It is unclear what the origin of these oscillations is. They are obtained by preparing a single state corresponding to one of the dips in Figure 9 with a slow microwave pulse. The other possible nuclear spin state is driven to the electron spin state 1. After a certain evolution time, the first pulse is applied again which results in the displayed and apparently anharmonic oscillation with frequency 117.02±0.89 kHz. This value is extracted from the spectrum of the data, as seen in the inset of the data plot, by fitting two Lorentzians to the double peak. The pulse sequence is also shown and the energy levels in the term diagram are explained in the following section (6.3).

would have to involve a polarization procedure for the spin [39, 40]. In addition to the hyperfine splitting, the carbon nucleus exhibits anharmonic oscillations between spin states in the electron spin state -1, as can be seen in Figure 10. The hyperfine coupling between electron spin and the ^{13}C spin is anisotropic in the $m_e = -1$ state which, using a hyperfine tensor coupling and the secular approximation, yields the eigenstates

$$\begin{aligned} |-1,+\rangle &= \cos\left(\frac{\theta}{2}\right)|-1,\downarrow\rangle + \sin\left(\frac{\theta}{2}\right)e^{i\phi}|-1,\uparrow\rangle\,, \\ |-1,-\rangle &= -\sin\left(\frac{\theta}{2}\right)e^{-i\phi}|-1,\downarrow\rangle + \cos\left(\frac{\theta}{2}\right)|-1,\uparrow\rangle \end{aligned} \tag{41}$$

with θ depending on the tensor components and $|\downarrow\rangle$ and $|\uparrow\rangle$ being spin states of the ^{13}C nuclear spin [38]. In general, this procedure predicts four transition frequencies. The forbidden transitions decrease in amplitude for lower θ and vanish with it which seems to be the case. By using that the difference of the transition frequencies to electron spin 1 is nearly equal to the ones to electron spin -1, one would infer that the two states are near degeneracy and that the splitting is less than the natural linewidths. A mixing process between the carbon spin states thus at least does not seem impossible.

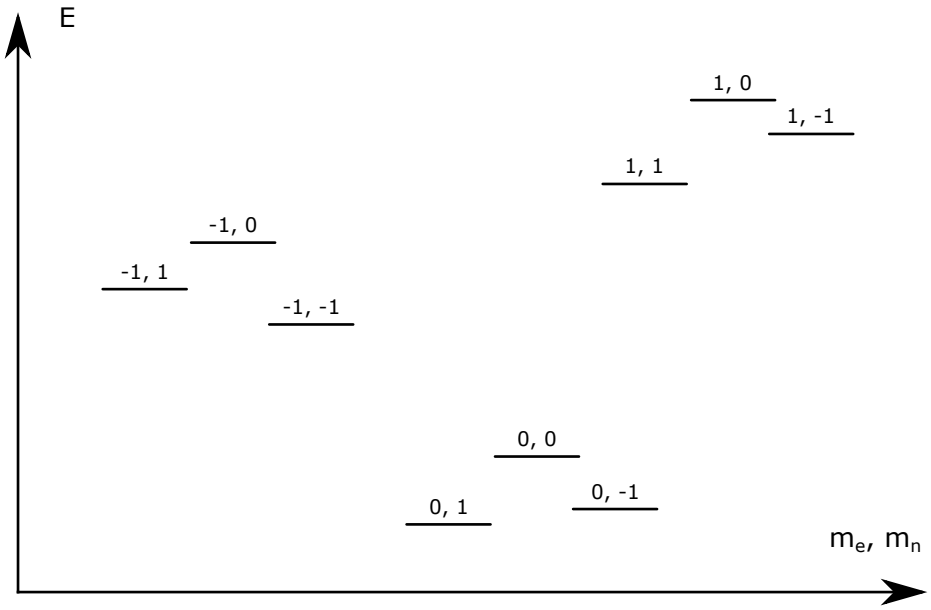

Figure 11: Structure and labelling of the relevant energy levels. The first number indicates the electron spin m_e and the second number gives the ^{14}N nuclear spin m_n. The two ^{13}C spin states for each level, degenerate at zero magnetic field for $m_e = 0$ due to the lack of a quadrupolar term in the $S = 1/2$ hyperfine interaction, are omitted.

6.3 Energy Levels

Spin states are written as $|m_e\, m_n\rangle$ (cf. Figure 11) and when the ^{13}C nuclear spin plays a role as $|m_e\, m_n\, m_c\rangle$. While for some experiments it is of no importance, the populations in the $m_e = \pm 1$ states being non-zero due to imperfect polarization of the electron spin affects the procedure of the experiment, the analysis or both. According to previous investigations, the electron spin is typically polarized to 70-90 % into the $m_e = 0$ state by the optical polarization process [41]. Consequently, every counter-oscillation etc. has to be considered for an accurate description of the systems dynamics. In general, this nine-level subsystem alone allows for a lot of interesting quantum information processing applications. In Section 7, entangled states involving $|0, 0\rangle$ and $|-1, 1\rangle$ and $|0, 0\rangle$, $|-1, 1\rangle$ and $|1, -1\rangle$, respectively, will be generated. After that, a similarly entangled state will be prepared and its decoherence process is reversed by flipping the non-zero electron spin in Section 8. Then the decoherence is used to demonstrate the effect of a measurement in Section 9 and finally, the nuclear spin of the ^{14}N atom is prepared in and projected onto certain states to demonstrate the possibility of creating orthogonal states and testing the ontology of the quantum state with it in Section 10.

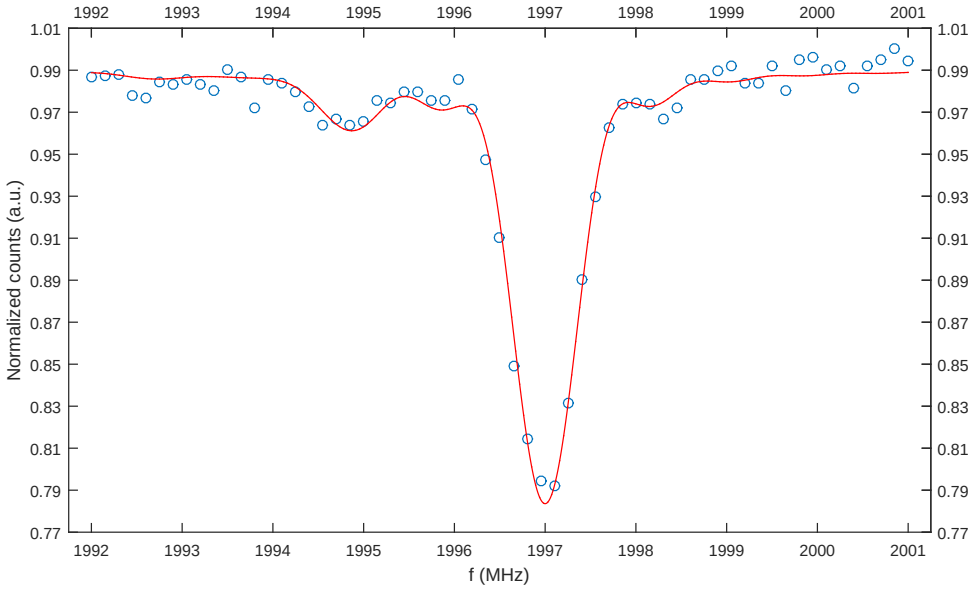

Figure 12: Polarization of the nuclear spin. This ODMR shows the degree to which the ^{14}N nuclear spin is polarized. The deepest dip corresponds to the transition $|0,1\rangle \rightarrow |-1,1\rangle$. The second dip near 1995 MHz is $|0,0\rangle \rightarrow |-1,0\rangle$ and $|0,-1\rangle \rightarrow |-1,-1\rangle$ near 1993 MHz is barely noticeable. Using the fact that the populations in the initial spin states are proportional to the depths of the dips, one gets that 88.6±1.6 % of the population is in the $m_n = 1$ state. The details of the fitting are described in the text.

One important insight comes through the fact that the depths of the dips in the ODMR in Figure 12 should be proportional to the relative populations of the spin states which can easily be derived from the linearity of the fluorescence in the electron spin 0 population. Two functions of the type in Equation 38 are fitted per dip for every ^{14}N spin state to give a proper fitting function. The ratios between the depths of the dips is held constant. The polarization process of the nucleus involves processes that increase the spin by one and ones that decrease it by one. The rates should not depend on the initial spin as the transition frequencies in the excited state are virtually the same but they depend on the direction. If r is the rate by which the spin is increased by one and s the rate by which it is decreased by one, a simple steady state solution of the rate equations gives the population ratios $\frac{p_1}{p_0} = \frac{p_0}{p_{-1}} = \frac{s}{r}$. Therefore the ratio of the populations between nuclear spin states is the same and the distribution is the same for different electron spin states. This also explains the polarization of the $m_n = 1$ state because $s > r$. The result of the fit is a polarization of 89 % of the nuclear spin state 1 when restricting the analysis to the electron spin 0. A high degree of polarization is obviously desirable, for it is of great interest to have a state that is as pure as possible.

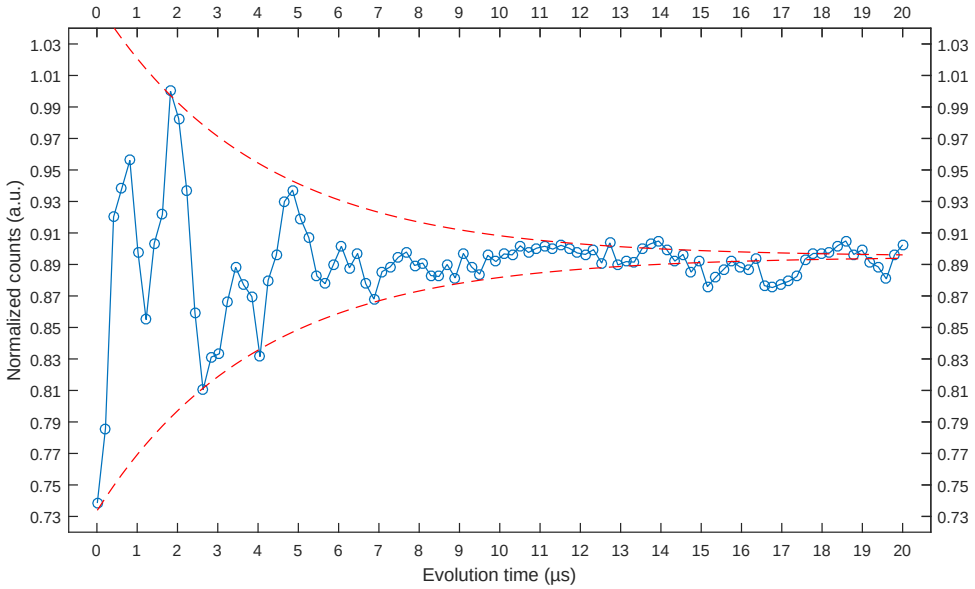

Figure 13: Free induction decay (FID) of the electron spin. By applying a $\pi/2$-pulse, an equal superposition between the two electron spin states $|0,1\rangle$ and $|-1,1\rangle$ is prepared. After a certain evolution time, another $\pi/2$-pulse is applied to potentially complete the transition to the state $|-1,1\rangle$. This way the coherence time of the electron spin is measured. The microwave frequency is detuned on purpose by approximately 500 kHz to create the oscillatory behaviour seen at the beginning while there is still coherence.

6.4 Lifetimes

Figure 13 shows the free induction decay (FID) measurement of the electron spin which involves the preparation of an equal superposition and the attempt to finalize the transition after a certain time. It shows a coherence time, usually called T_2^*, of approximately 4 μs. The coherence time of the nuclear spin has been determined to be 8.3$\pm$1.1 ms by observing oscillations in the FID signal up to 5 ms. The spin-lattice relaxation time, or T_1, of the electron spin state 0 is measured as 3.48$\pm$0.99 ms by observing the decay up to 10 ms. The transversal, or spin-spin relaxation, time, or T_2, of the electron spin which is measured by applying a π-pulse between the two pulses in the FID gives the degree to which the coherence information is stored in the proximal environment such that it can reappear in revivals of the electron spin coherence. For diamonds with impurities, typical values range up to few hundred microseconds [3, 42], depending on the diamond sample and the magnetic field strength. There is some indication that the ^{13}C nuclear spin decays with a time constant of approximately 200 μs. This estimate was established by preparing a certain carbon spin state, waiting and then reading the spin state. The next sections are dedicated to the main experiments.

7 Spin Entanglement

7.1 General Scheme

The idea of showing entanglement relies on the decoherence behaviour of an entangled state. As it involves a superposition of two electron spin states, these two components are expected to lose their phase relationship because the electron rapidly decoheres by interacting with its environment. By measuring the degree of coherence, it should be possible to track the loss of coherence when transitioning through entanglement and with increasing evolution time for entangled states. The coherence is measured by scanning the phase of the radio-frequency signal coming from RF2 in Figure 5 where the pulse sequence for generating an entangled qubit-qubit state, ideally of the form $|\psi\rangle = \frac{1}{\sqrt{2}}(|0,0\rangle + |-1,1\rangle)$, is depicted. When recombining the state, the Rabi oscillation between $|0,1\rangle$ and $|0,0\rangle$ that was initiated by the π-pulse from RF1 is continued. By introducing a phase shift, here it is done using a second source, one can influence the direction of the oscillation up to the point of reversing it halfway. The scan gives a sinusoidal oscillation (cf. for example Figure 14) and the contrast can be used as a measure of coherence. This is done for different degrees of entanglement and different evolution times of the state. By observing a minimum of coherence after an evolution time of 5 μs for a maximally entangled qubit-qubit state and by showing the complete loss of coherence after an evolution time of 10 μs, the conclusion is drawn that the electron spin and the spin of the ^{14}N nucleus are entangled and that the degree of entanglement stands in a certain relationship to the degree of coherence that is destroyed by this time evolution. In the case where the coherence is lost completely, two incoherent spin populations counter-oscillate in the recombination process regardless of the phase shift and, effectively, no oscillation can be observed. This is the general scheme by which entanglement is demonstrated and even quantified. Generally speaking (this holds for all, not only the entanglement experiments), the electron spin and the nuclear spin initially are not in a pure state but an incoherent mixture of all the spin sates with $|0,1\rangle$ being the most highly populated one, as explained before. But this state is still treated as a pure state while keeping track of the observable influences of the other populations on the readout fluorescence, wherever they are present. This section on entanglement is divided in the following way. First, in Section 7.2 the way of measuring coherence is described and the decoherence profile of an entangled qubit state is shown. It becomes evident that coherence is completely lost after a long enough evolution time. Then the transition through entanglement is discussed with a demonstration of the degree of coherence after 5 μs for states of different degrees of entanglement. An apparent minimum is observed for the state that ought to be maximally entangled. After that the degree of entanglement is quantified by means of estimating errors and using facts about the observed Rabi oscillations before the observed symmetry is looked at in detail and a generalization is attempted.

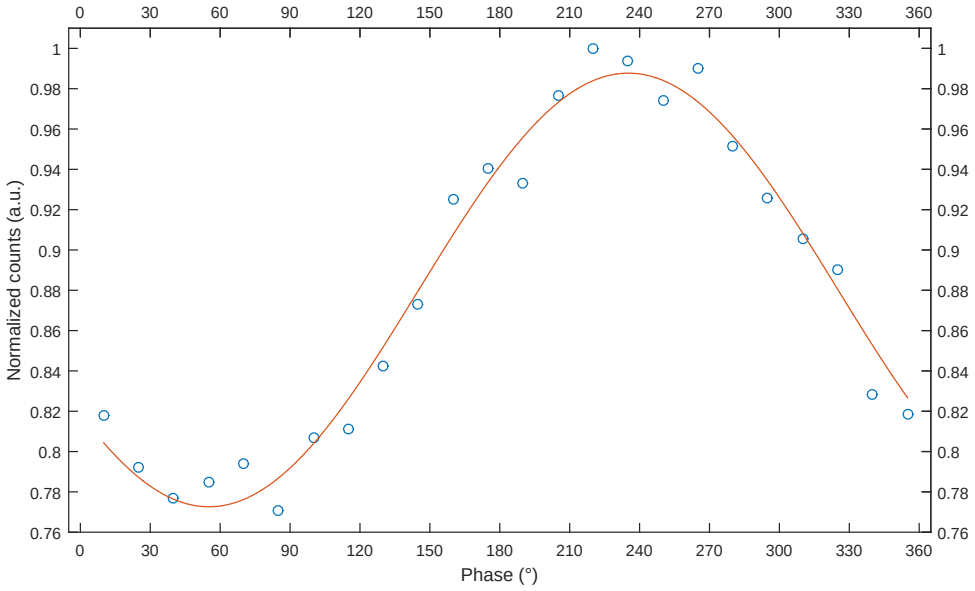

Figure 14: Phase scan of the radio-frequency pulse that constitutes the last step in recombining the entangled qubit-qubit state. One RF source is used in preparing the entangled state while the second is used to recombine it. The second source is phase shifted by the angle that is plotted on the x-axis. The Rabi oscillation is completed with a phase shift of 235°, reversed with 55° and by scanning the phase, the complete oscillation is recovered. Its contrast is used as a measure for the degree of coherence.

7.2 Coherence Measure

The proof of entanglement by witnessing the decoherence of the state works by getting a handle on the quantity called coherence. The phase scan of the combining RF source in Figure 14 is an example for the method that is employed. For any entangled state and after any time duration of letting it evolve freely, this tool can be used as the benchmark for the question about the degree to which a phase relationship still exists between the spin components of which the state is composed. The phase shift of 235°, probably stemming from the hyperfine splitting due to the ^{13}C nucleus, is used for measuring the decoherence profile of the state (cf. Figure 15). It reveals an oscillation that is attributed to the interaction with the carbon nucleus. The decoherence profile of the entangled qubit state resembles the FID measurement in Figure 13 up to a horizontal reflection due to the fact that the state in which the entangled state is recombined does not coincide with the readout state in this case. One can see that there is still coherence after 5 μs which is used in the next section to demonstrate a minimal coherence for the maximally entangled state that is diminished but finite. In addition, Figure 16 shows the lack of coherence after 10 μs via a direct Rabi oscillation.

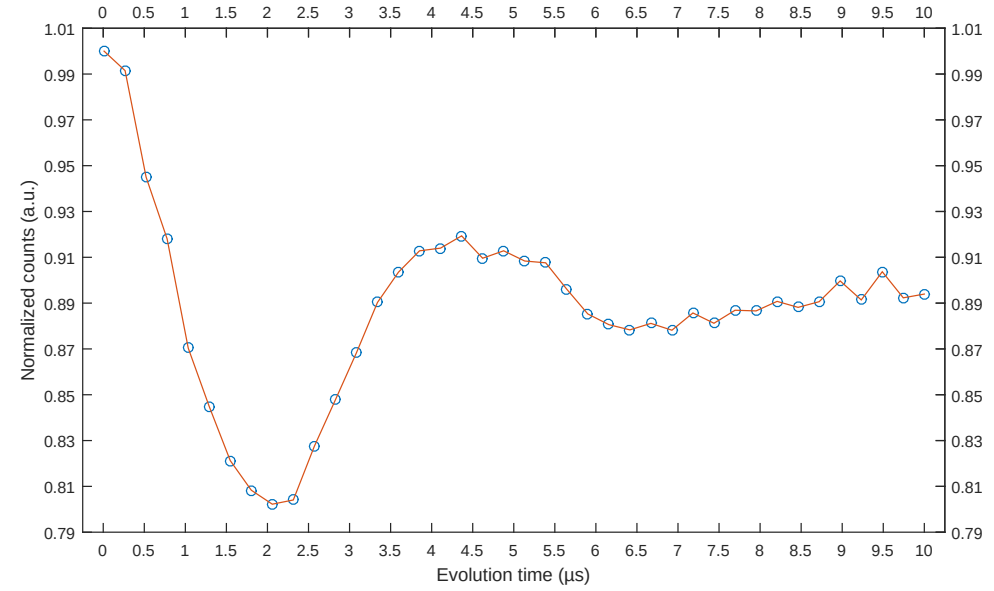

Figure 15: Decoherence profile of a fully entangled qubit-qubit state. The entangled state is prepared and after a certain evolution time, it is recombined (see Figure 5 for the pulse sequence). After 5 μs, there still seems to be coherence (cf. Figure 18).

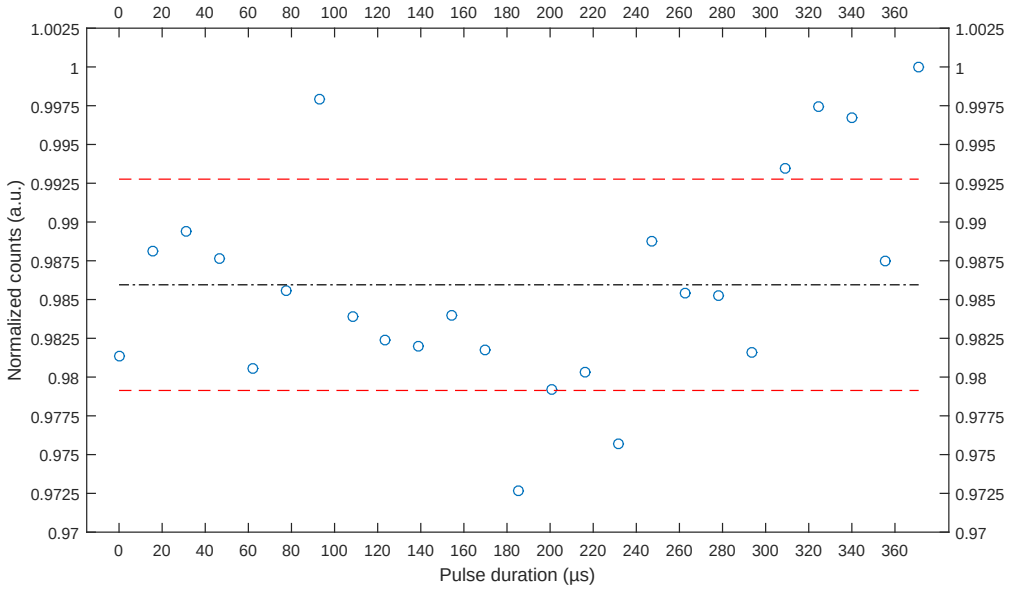

Figure 16: Lack of coherence after an evolution time of 10 μs. The application of RF pulses with different durations that cover two full oscillation periods is illustrated here.

7.3 Transitioning through Entanglement

To get a full picture of the entanglement process, an additional variable is introduced which is the population transfer η. To understand how it is defined, the procedure has to be explained first. The microwave that is providing the entangling pulse produces a Rabi oscillation for the relevant transition with the duration of a π-pulse being T. To create any partially entangled state, a pulse of length kT is applied with $k \in [0, 2]$. For the recombination of the state, a pulse of length $(1-k)T$ is needed to get a 2π-pulse in total. The stipulation of this exact procedure ideally generates a state of the form

$$|\psi\rangle = \frac{1}{N}\left[|0,0\rangle + \cos\left(\frac{k\pi}{2}\right)e^{i\phi_1}|0,1\rangle + \sin\left(\frac{k\pi}{2}\right)|-1,1\rangle\, e^{i\phi_2}\right], \tag{42}$$

with the approximations described in Section 4.1 (cf. Equation 11). N is the normalization of the state and ϕ_1 and ϕ_2 are arbitrary phases. The effect of a slight detuning and off-resonant driving of populations in other spin states is discussed in Section 7.4 where a number is put on the degree of entanglement that is achieved by this experiment. The population transfer is defined as $\sin\left(\frac{k\pi}{2}\right)^2$ with the right half folded up. It is the total population transfer in the Rabi oscillation and can be written as follows.

$$\eta(k) = \begin{cases} \sin\left(\frac{k\pi}{2}\right)^2 & \text{if } k \in [0,1] \\ 1 + \sin\left(\frac{(k-1)\pi}{2}\right)^2 & \text{if } k \in (1,2] \end{cases} \tag{43}$$

This quantity is chosen as the descriptive parameter for the entangled states in what follows as the degree of entanglement is expected to depend on the probabilities for the respective states and not the amplitudes. It also allows the transition through entanglement to be illustrated in a convenient way. The next page shows contrast measurements as described above after 5 μs of evolution time (cf. Figure 15) for states of different degree of entanglement parametrized by the population transfer η. In Figure 17, the measured oscillations for four entangled states are juxtaposed as a comparison of the degree of coherence. Figure 18 shows the extracted contrasts defined as two times the oscillation's amplitude divided by its maximum value. Both indicate a near perfect symmetry in η as is expected theoretically. So the maximally entangled state with $\eta = 1$ indeed has the lowest degree of coherence. The conjecture of the fact that this state seems to have vanishing coherence after 10 μs and the observed minimum in degree of entanglement leads us to the conclusion that it actually is a maximally entangled state up to experimental error. Considering that there are disregarded variables in this superficial analysis and that measured quantities bear uncertainties, the next destination is the determination of the real degree of entanglement of this exact state. To this end, it will be necessary to discuss phases, involve an additional spin state and the concepts from Section 4.4 for measures of entanglement.

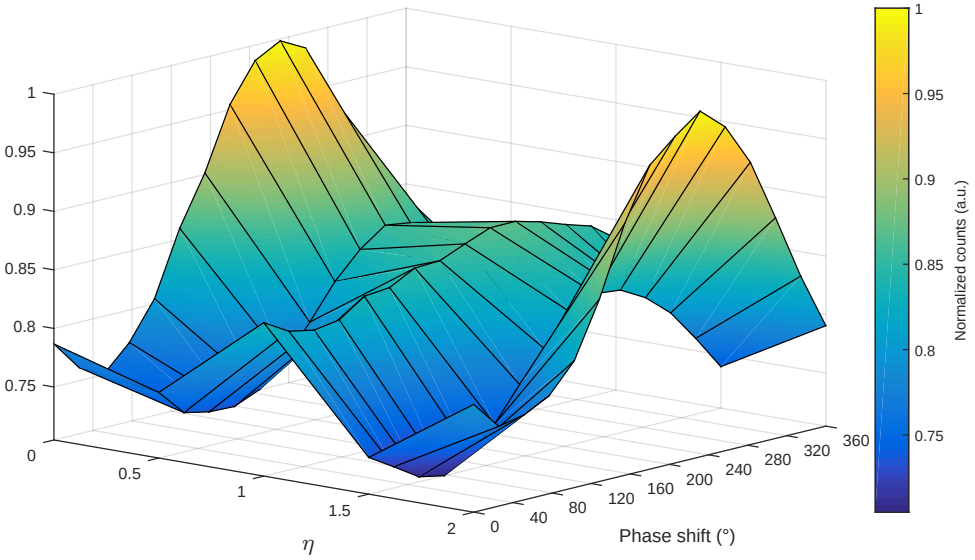

Figure 17: Coherent oscillations in recombining states with different degrees of entanglement. The population transfer η, defined in the main text above, parametrizes the state space which is doubly covered to test the symmetry and agreement with theory.

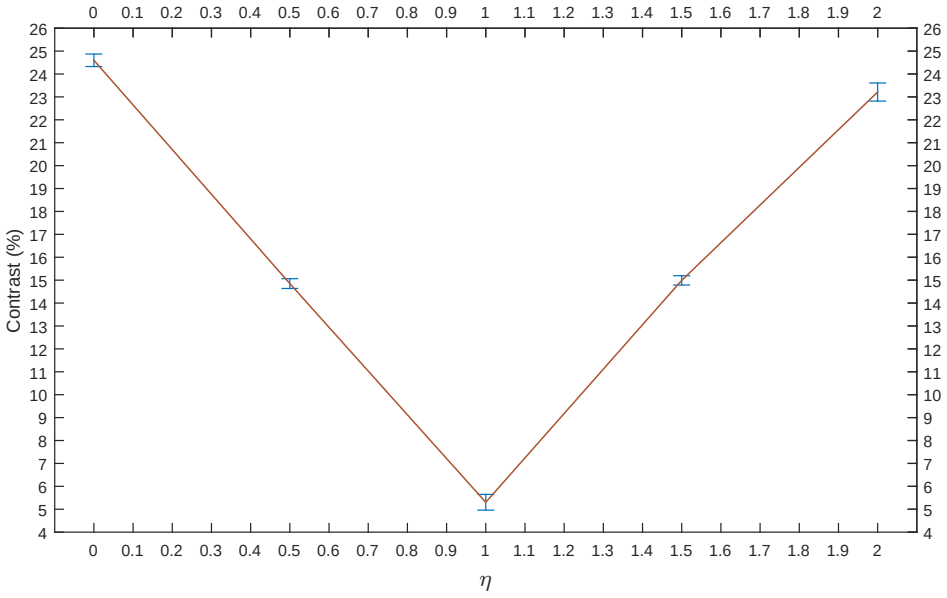

Figure 18: Contrasts quantifying the degree of coherence for the four states in Figure 17 above. The symmetry in the data indicates a maximum in entanglement at $\eta = 1$.

7.4 Degree of Entanglement

The first thing to notice is that the description of the state in Equation 42 completely neglects the off-resonant but coherent driving of the population in the state $|0,0\rangle$ to the state $|-1,0\rangle$. The estimation of this process has to involve the uncertainties in frequencies as does the discussion about the degree of entanglement in general. The electron spin transition frequencies are known to drift slowly over hours and days due to extremely fine changes in the magnetic field. To compensate for any such influence on the measurement, the data acquisition for the point describing the state with $\eta = 1$ in Figures 17 and 18 was, just as all the other ones, interrupted for intermediate measurements of the transition frequencies approximately every one and a half hours. While the uncertainty of these measurements is completely negligible, the values do show a dispersion of 8 kHz. To cover any frequency jitter during the measurement, an uncertainty of 50 kHz is assigned to the transition frequency. Using the two qubit model described in section 4.2.2, the amplitudes are calculated. The new state is now

$$|\psi\rangle = \alpha\,|0,0\rangle + \epsilon\,|0,1\rangle + \beta\,|-1,1\rangle + \zeta\,|-1,0\rangle\,, \tag{44}$$

with α, β, ϵ and ζ determined by taking an equal statistical mixture of the two ^{13}C spin states. This procedure is justified by the assumption that there is no phase relationship between the states and so no interference phenomena are expected. An error in radio-frequency for the ^{14}N nucleus is not considered as these transition were not observed to drift and the measurement uncertainty is negligible. For the measurement in Figure 14 with a π-pulse duration of 375 ns and a hyperfine splitting of 2.199 MHz, the relative entanglement entropy, defined as $\frac{S(\hat{\rho})}{\max_{\hat{\rho}}[S(\hat{\rho})]}$, calculated with the above assumptions is

$$\frac{S[\hat{\rho}_A]}{\ln(2)} = 93.9 \pm 1.3\ \%, \tag{45}$$

where an additional contribution to the error stems from an uncertainty of 6 ns in the Rabi period. It is determined by a comparison of the observed oscillation with prediction. During this particular measurement no intermediate ODMRs were made and a microwave detuning of 60 kHz revealed by an ODMR conducted shortly after the measurement is also included in the above value for the entanglement entropy. The deviation from maximal entanglement is a consequence of a total population of 2.64±0.46 % in the states $|0,1\rangle$ and $|-1,0\rangle$. The error is dominated by the uncertainty stipulated for the transition frequency. The values broadly agree with a six level model while a two level model predicts a slightly higher degree of entanglement. The relative negativity, defined as $-2\mathcal{N}(\hat{\rho})$, is a second estimator for the degree of entanglement:

$$-2\mathcal{N} = 94.85 \pm 0.91\ \%. \tag{46}$$

In summary, the construction of the estimators for the degree of entanglement are based on simple observations about Rabi oscillations and the associated uncertainties.

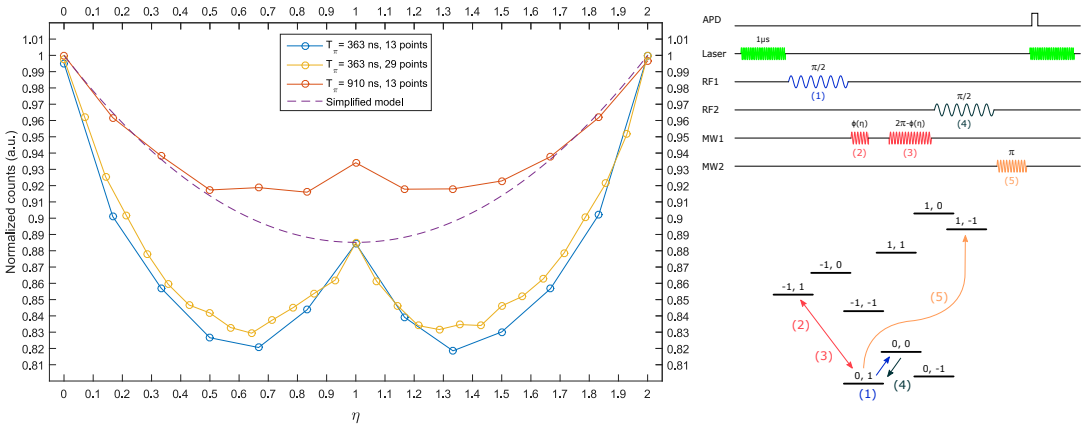

Figure 19: Recombination of partially entangled states described by the population transfer η using two different π-pulse durations. The apparent offset at the symmetry point derives from a phase shift that was optimized for short π-pulses and a normalization using the maximum value which is reduced by this inadequate phase. The dashed line shows a simplified model ignoring the effects of microwave phase rotations, off-resonant driving, remnant coherence and the presence of populations in the electron spin state $m_e = -1$, all depending on η. These effects are expected to produce the shape of the data curves. The value at the symmetry point should be (nearly) a shared point between model and data because it is near to the decoherence limit of the counts.

7.5 Symmetry

A further analysis of the observed symmetry when transitioning through entanglement is given below, connected to the data shown in Figure 19. It shows the recombination of different entangled states after 5 μs. To quantify the symmetry, the asymmetry is defined as the absolute value of the difference between symmetric measurement points

$$\bar{s} = \sum_{\eta=0}^{<1} |r^*_\eta - r^*_{2-\eta}|, \tag{47}$$

where r^*_η is the normalized count rate for the state with entanglement parameter η. For the three depicted data sets, the respective mean values and standard errors are

$$\bar{s}_1 = 2.78 \pm 0.76 \text{ ‰},$$
$$\bar{s}_2 = 2.03 \pm 0.96 \text{ ‰},$$
$$\bar{s}_3 = 4.48 \pm 0.91 \text{ ‰}.$$

The lowest value corresponds to 1 % of the contrast. This seems fairly low and it is another indicator that the highest entanglement should be found very close to $\eta = 1$.

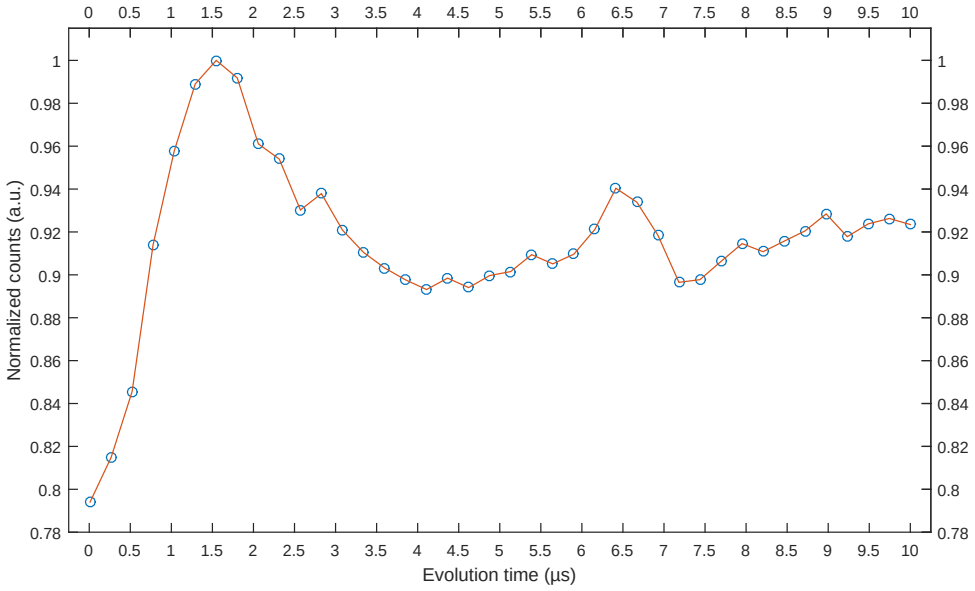

Figure 20: Free induction decay measurement of a superposition of all three electron spin states. As a reference for the investigation of entangled qutrit states, the FID of an equal superposition of the states $|0,1\rangle$, $|-1,1\rangle$ and $|1,1\rangle$ up to 10 μs is provided.

7.6 Generalization to Qutrit Entanglement

The procedure of the last sections could be generalized to qutrit states involving all three spin states for both the electron and the nitrogen nucleus. This endeavour is only suggested in this last section on entanglement. The idea is, again, a dense sampling of partially entangled states combined with an observation of their decoherence behaviour. Figure 20 shows a FID measurement of a state that is an equal superposition of all electron spin sates. It serves as a comparison for the decoherence profile of the entangled qutrit state in Figure 21 which involves the recombination of the state. Figure 22 is the analogous measurement to Figure 19. Note that for the decoherence profile a slightly different sequence is used than for the entanglement transition measurement. In the former, the population in the state $|0,0\rangle$ is transferred to $|-1,0\rangle$. Then the main population in $|0,1\rangle$ is placed in $|0,0\rangle$ and two subsequent RF split the population on the three nuclear spins in electron spin state 0. Lastly, two microwave pulses create a partially entangled state. Neglecting off-resonant driving, the state is

$$|\psi\rangle = \frac{1}{N}\left[\,|0,0\rangle + \sqrt{1-\eta}\,\big[\,|0,1\rangle + |0,-1\rangle\,\big] + \sqrt{\eta}\,\big[\,|-1,-1\rangle + |1,1\rangle\,\big]\right] \qquad (48)$$

for $\eta \in [0,1]$ and with the phases neglected. The measurement in Figure 22 does not use the first pulse. But the asymmetry is mainly attributed to measurement uncertainty.

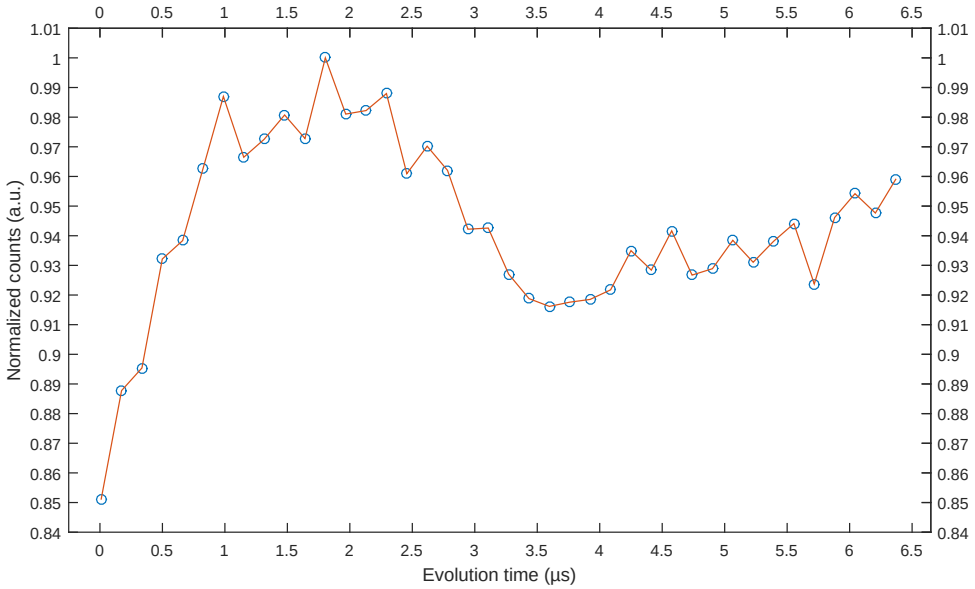

Figure 21: Decoherence profile of an entangled qutrit-qutrit state. The state is prepared and after a certain evolution time it is recombined in $|0,0\rangle$ from where it is read out.

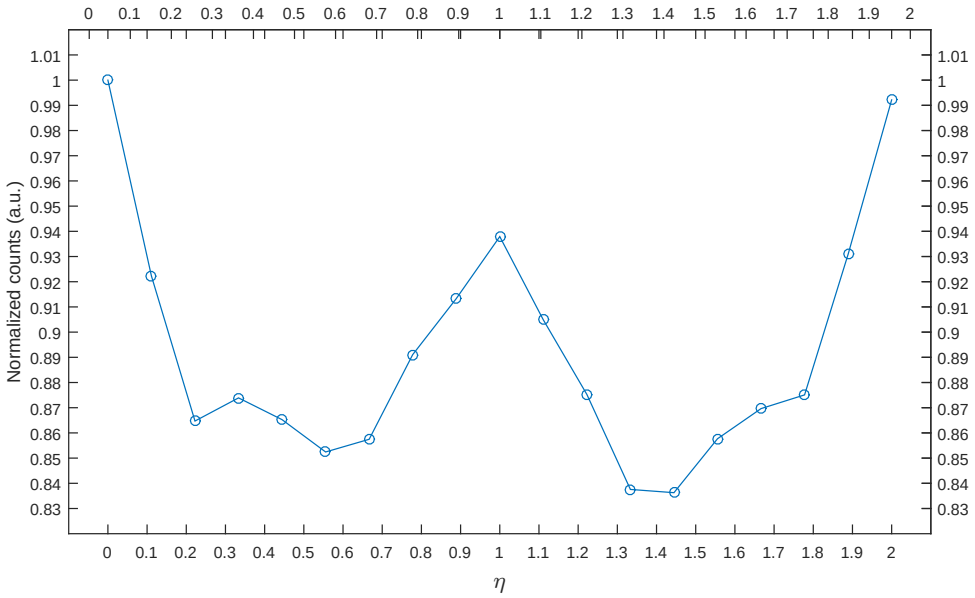

Figure 22: Transition through qutrit entanglement. The data exhibits an asymmetry of 1.10±0.39 % as defined in Equation 47 that is attributed to measurement uncertainty.

8 Reversing Decoherence

8.1 Concept

This chapter deals with the problem of reversing decoherence in the most direct manner, so far as it is possible. To this end, the only quantum mechanical entity that is attributed to the decoherence process is used to induce a rewinding process: the spin, more precisely the electron spin in this case. Insofar as the decoherence of the electron spin is governed only by the spin state and a time-independent Hamiltonian, the loss of phase coherence due to perturbations caused by the surrounding system should be perfectly reversible for any decoherence time. As these conditions are not expected to actually apply to the given system, limitations on the evolution time are anticipated by the time-dependence of the Hamiltonian alone. The degree to which these limitations can be exhausted and what limitations are set by the procedure itself is the subject matter of a set of experiments conducted for the purpose of developing a direct method of preserving coherence via an actual reversal of the decoherence mechanism. An entangled state, similar to the qubit state described before, is prepared and after a fixed evolution time, the non-zero electron spin component is flipped to induce a reverse gear evolution of the system. After exactly the same evolution time, up to accuracy of the electronic devices, the spin is flipped back to its original state. This way the complete time evolution of the electron spin should be compensated, at least in the ideal case. The coherence is measured in the same way as for the entanglement demonstration, described in Section 7.2. After applying the rephasing sequence, the population in $|-1,1\rangle$ is brought back to $|0,1\rangle$ where an oscillation in the recombination of the state is measured by applying a last readout MW pulse to $|1,1\rangle$. Every spin flip involves two short ($\approx$ 200 ns) MW pulses. An entangled state

$$|\psi\rangle = \frac{1}{\sqrt{2}}\big[\,|0,-1\rangle + |-1,1\rangle\,\big],$$

of course idealizing the procedure and also ignoring phases, is used to reduce off-resonant driving of the population in the electron spin 0 state. A single spin flip gives

$$|\psi\rangle = \frac{1}{\sqrt{2}}\big[\,|0,-1\rangle + |1,1\rangle\,\big].$$

It is realized by applying the transitions $|-1,1\rangle \rightarrow |0,1\rangle \rightarrow |1,1\rangle$ in this order. One pair of spin flips with an evolution time of τ preceding each of them is called a correction. Section 8.2 presents a direct measurement of the coherence during a free evolution of the state. Then, in Section 8.3, the limits of using a single correction are being explored. The last section (8.4) discusses the results obtained from using multiple corrections. An analysis of the observed data in terms of the underlying mechanisms and the conclusions for the efficacy of the procedure is given for both the case with the single correction (2 spin flips) and the case with multiple corrections (2N spin flips).

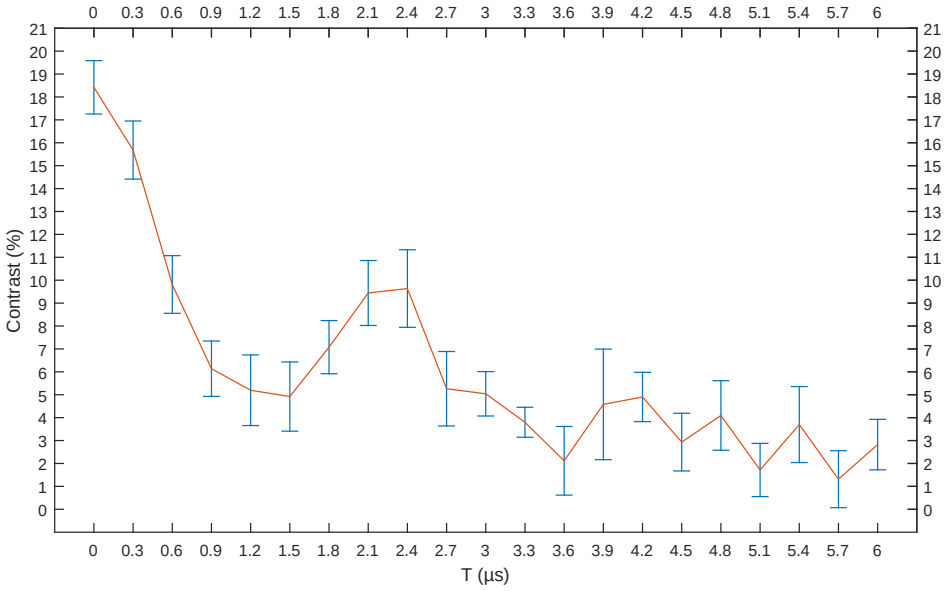

Figure 23: Contrast as measure of the degree of coherence for free evolution of an entangled qubit-qubit state. As before, the contrast is extracted from the phase scan in the RF source recombining the entangled state. The error bars are standard errors calculated from a sinusoidal fit. The oscillations are attributed to the interaction of the electron with the ^{13}C nucleus. This curve will act as a reference in Section 8.4.

8.2 Free Evolution

To be able to observe an improvement in coherence time, a reference is needed. The coherence measurements for a free evolution of the entangled state are shown in Figure 23. It is taken out of a set of measurements using multiple spin flips for rephasing the electron, discussed in Section 8.4, with MW π-pulse durations of 206 ns and 204 ns for the two pulses making up one spin flip. For the measurements in the next section, a separate curve is acquired with the parameters used there. So Figure 23 serves only as an example. The two data sets, however, agree on the most important characteristic which is coherence time. As discussed before, after an evolution of 6 μs, every reasonable degree of coherence is lost. That is the point where the degree of coherence has dropped to less than a fifth and slowly decays without any observed revivals. It will be argued that this coherence time can already be extended by performing a single spin flip. The quantity that will be used as a comparison to the free evolution time is the total evolution time $T = 2N\tau$, where N is the number of corrections and τ is the evolution time preceding every spin flip in the sequence. The idea is to show that even though the system is in two entangled states that should decohere at a similar or even the same rate, the addition of the evolution times in each does not naively compare

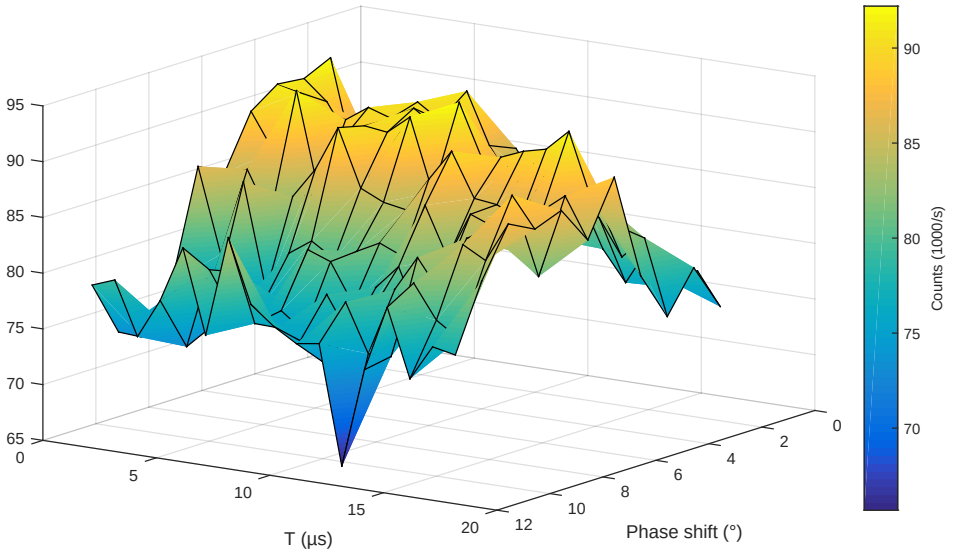

Figure 24: Coherence after correcting with one pair of spin flips. The time axis gives the sum of evolution times preceding the spin flips. Notice the slow decay of coherence as measured by the contrast of the oscillations at equal time (cf. Figure 25). This seems to be in strong opposition to the free evolution of the system as depicted in Figure 23. The small number of spin flips suggests an explanation beyond fidelities.

to an equivalent evolution time in one of them because the evolution is (partially) reversed. So for the total time in just one of the states, the time axis termed T in the relevant diagrams has to be halved. But the actual definition of T seems to be justified well because it emphasizes the difference between free evolution and evolution interrupted by spin flips. Both durations will be called T, distinguished by the context.

8.3 Single Correction

As will be discussed later, the application of multiple spin flips is slightly problematic due to the somewhat hard problem of comprehending the full process in a theoretically successful manner. But a single correction involves only two spin flips, or four MW pulses, and is thus within a realm that can be modelled easily. Figure 24 shows a juxtaposition of the frequently mentioned oscillations in combining the entangled state for different times T which are total evolution times, as described above. It is apparent that the coherence does not decay quickly on a short time scale as 6 μs. The quantified version of it is seen in Figure 25, where the contrasts for each evolution time are plotted combined with their standard errors and also a reference curve measured

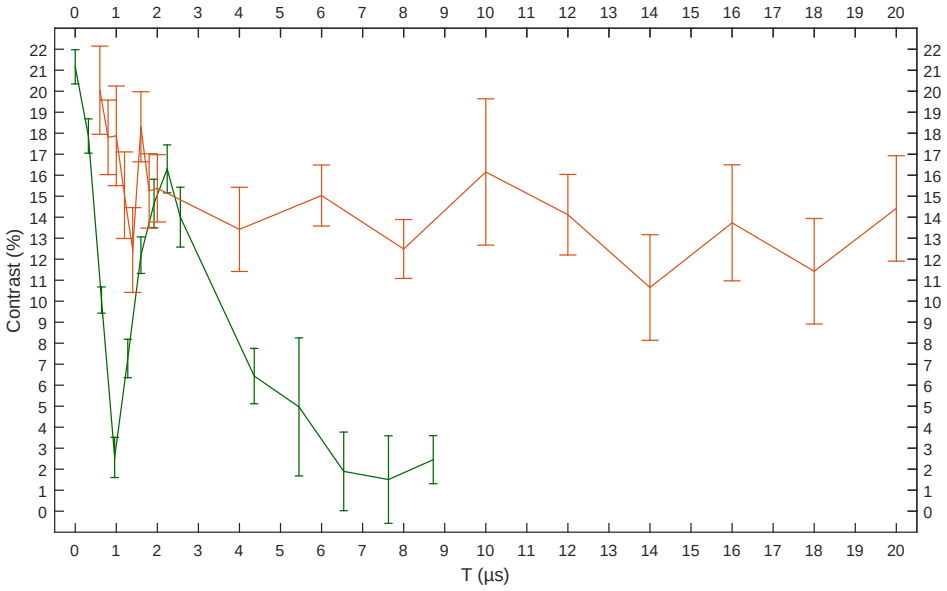

Figure 25: Contrast as coherence in rephasing the electron spin with one pair of spin flips. The contrasts of the oscillations in Figure 24 are extracted by fitting a sinusoidal function (orange curve). The coherence during a free evolution of the state using the same parameters is shown as a reference (green). It is not the curve in Figure 23. Here, the π-pulse duration of the two spin flip MW pulses is 216 ns and 252 ns, respectively.

for the free evolution of the system with the same parameters for the MW pulses. The durations of the MW pulses are 216 ns and 252 ns for the transitions $|0,1\rangle \leftrightarrow |-1,1\rangle$ and $|0,1\rangle \leftrightarrow |1,1\rangle$, respectively. An important thing to consider is the entirety of effects that can lead to an increase in observed contrast, at least for the case with the correction applied. Consider the initial state before applying MW pulses, which is something like $\frac{1}{\sqrt{2}}[|0,1\rangle + |0,-1\rangle]$. An imperfect MW pulse transfers most but not all of the populations in the transition $|0,1\rangle \leftrightarrow |-1,1\rangle$ and some but not a zero amount of the populations in the transition $|0,-1\rangle \leftrightarrow |-1,-1\rangle$. The same applies for a MW pulse to the electron spin state 1. Coherence between the two nuclear spin states in the non-zero electron spin state is created. But the important feature for the coherence measurement is the similarity of the amplitudes and this feature is suppressed by the high ratio deriving from the goodness of the pulses. Letting the electron spin contributions decohere from each other and applying the pulse again gives a negligible ratio. Applying a RF $\pi/2$-pulse and scanning the phase of the signal does not give any contrast in the extreme case of only one state being populated. This is also the reason why incoherent populations do not give any contribution at all. These considerations lead to the conclusion that there should be no significant

contribution to the observed contrast once the electron spin components have dephased and therefore the above data cannot be explained by any fidelity arguments about the spin flips connected to off-resonant or imperfect driving. On the contrary, the extra MW pulses are even expected to lower the contrast. Some genuine coherence has to be present for the contrast to be of any appreciable value. The initial population in $|0,0\rangle$ counter-oscillates with respect to the main population in $|0,1\rangle$. This can be seen by imagining the states $|0,1\rangle$ and $|0,0\rangle$ forming a qubit with states on the north and south pole on the Bloch sphere. The first $\pi/2$-pulse brings them to the equator. The transition $|0,0\rangle \leftrightarrow |0,-1\rangle$ plays no important role because the relative phase is conserved. When a portion of the population in $|0,-1\rangle$ is lost through off-resonant driving, the two states are kinked down equally on the Bloch sphere. Any relative phase that is picked up during the pulse sequence is the same for both of these incoherent contributions. The recombining RF pulse rotates the states by an axis on the equator which always results in opposite z-components. The contrast decays at the latest after $T = 40$ μs to approximately 5 % and does not rise again. The coherence time is improved by a factor of five through this correction consisting of one pair of spin flips.

8.4 Multiple Corrections

As can already be seen in the previous data (cf. Figure 25), the best strategy to rephase a superposition of the electron spin seems to be with a single evolution time $\tau \ll 1$ μs. The reason why this is evident is the fact that after this time a significant portion of the coherence seems to be already lost even after a single correction. Adding a few corrections after that is not expected to increase the coherence at any point which agrees with observations. A similar reasoning as before could be applied for the observed data using the π-pulse durations of the two MW pulses, namely 202 ns and 206 ns, respectively. The important distinction, however, is the short single decoherence time τ that does not allow for the assumption of complete decoherence. While this puts a constraint on the convenience of the analysis, a few simple facts can be established as a starting point and then the rest of the argument is developed. According to a nine level model, the spin flip in the direction $|-1,1\rangle \rightarrow |1,1\rangle$ coherently guides 98.68 % of the populations in the initial states $|-1,1\rangle$ and $|0,-1\rangle$ to the target states $|1,1\rangle$ and $|0,-1\rangle$ and 98.69 % in the other direction. The off-resonant driving of the population in the state $|0,-1\rangle$ is very low ($<$0.5 % population transfer) for both pulses. So the argumentation from the last section certainly applies to some number of corrections in the sense that if there were no coherence after one single decoherence time τ, there would be no contrast either. The other extreme case is $\tau = 0$ where, in the ideal case, no loss of coherence is expected due to the fast Rabi oscillations of the spin flips. The finite fidelity of the spin flips, however, can lead to a reduction in the observed contrast. Even though the off-resonant driving is extremely low for π-pulses, the sequential application of pulses can lead to a coherent build-up

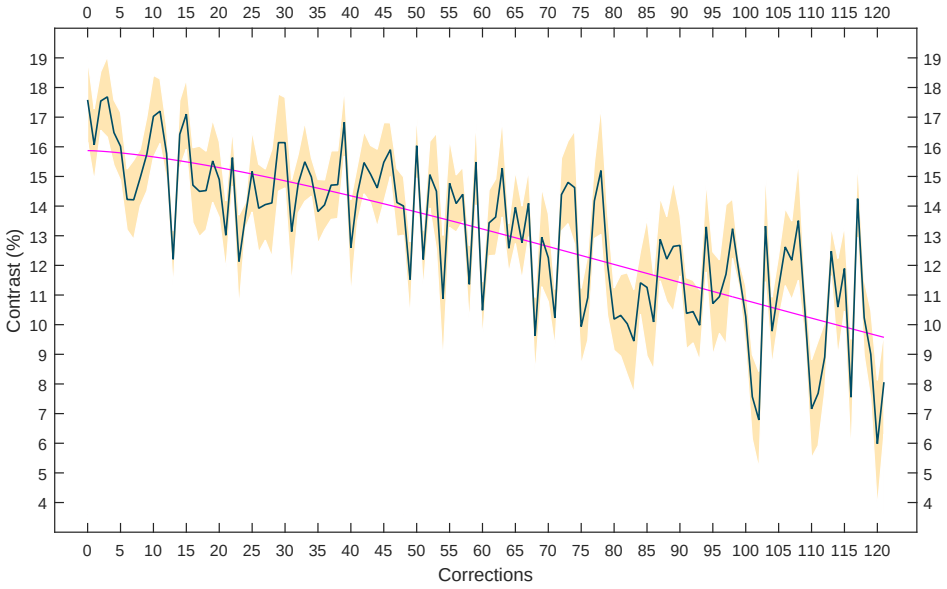

Figure 26: Reversing decoherence without decoherence. The total effect of the coherent manipulations involved in the rephasing procedure are studied by applying spin flips without letting the state decohere freely and measuring the contrast. The yellow band is the standard error. Note that each correction involves one pair of spin flips, where a spin flip is a transition between electron spin 1 and -1. A decay function of the form $ae^{-(c/c^*)^p}$ is fitted from which the exponent p=1.45±0.30 and the decay constant c*=193±23 are extracted. The same procedure is applied for the curves in Figure 28.

of populations due to the amplitude of the off-resonant Rabi oscillation that is not low. For example, an application of ten corrections within the nine-level model gives a distribution of populations of 48.3 %, 21.2 %, 14.8 %, 14.1 % and 1.3 % among the states $|-1,1\rangle$, $|1,-1\rangle$, $|0,-1\rangle$, $|-1,-1\rangle$ and $|0,1\rangle$, respectively, when starting with $\frac{1}{\sqrt{2}}[|-1,1\rangle + |0,-1\rangle]$. Considering that 10 corrections correspond to 40 MW pulses, this should not be too surprising. Looking at the two states that are supposed to be recombined, this would mean a reduction in contrast to 64 % of the initial value when the overall reduction in fluorescence counts is ignored (cf. Figure 26 for a comparison). But in the relevant case there is a non-zero decoherence time between spin flips and thus the remnant populations of one pulse, which are expected to be very small as described above, decohere not only once but also during the application of the two pulses connecting to the second electron spin state and the evolution time in said until the correction cycle is completed. So the total dephasing time of the remnant populations is 800 ns up to 2400 ns, depending on the method as discussed later. Comparing with Figure 23, one notices that this should be enough to destroy most of

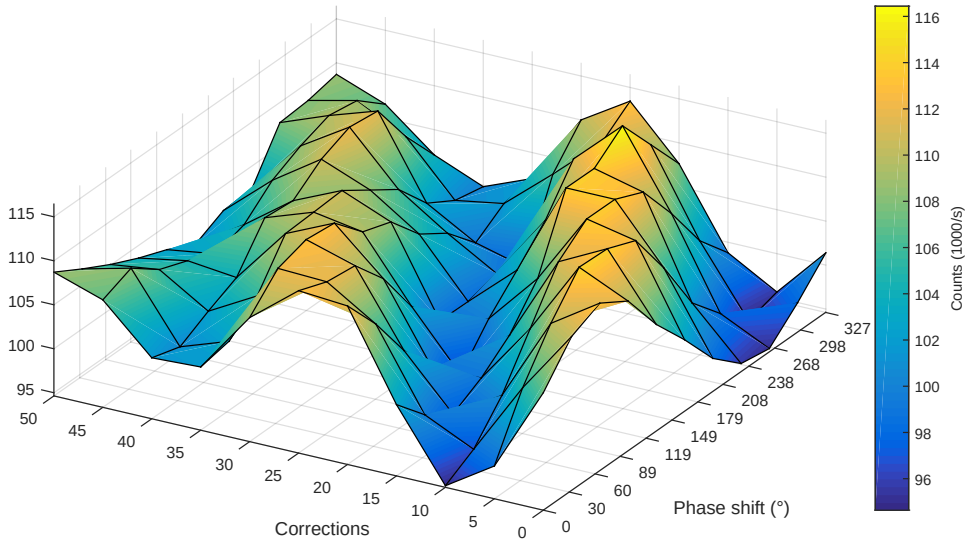

Figure 27: Coherent oscillations after rephasing with multiple spin flips. The diagram shows phase scans after different numbers of corrections and a single decoherence time τ of 400 ns. Most noticeable is the slow fading away of the contrast (coherence) that lasts up to the 50th correction which corresponds to a total procedural time of 81 μs.

the coherence. The consequence is that the coherent build-up of remnant populations in unwanted states is not only suppressed but also partially compensated for by the incoherent components arising from the decoherence process. Even if this were only the case for one of the electron spin states, e.g. because the rephasing is successful, this would then mean that the reversal of the decoherence was successful and thus a deviation from this description would even be a positive feature. Secondly, the distribution of the populations among states would not lead to an increase in observed contrast but rather a decrease up to the denominator in the definition of the contrast that compensates mathematically to, actually, also decrease it. This is more or less a consequence of the unitarity of the applied transformations or the conservation of probabilities. Let p_0 and p_1 be the populations in the zero and non-zero electron spin state, their sum is p_s and r_0 and r_1 are the fluorescence rates of these states. Then the contrast is $c = \frac{p_0(r_0-r_1)}{p_0 r_0+p_1 r_1} = \frac{r_0-r_1}{r_0-r_1+\frac{p_s}{p_0}r_1}$. So it decreases overall with decreasing p_0. The argument also works when it is assumed that the coherent population is only a part of p_0. In Figure 27 the coherent oscillations after up to 50 corrections and a single decoherence time of 400 ns are visualized as an example. Again, there is an evident regularity and monotonicity suggesting a slow decay of coherence with increasing number of corrections. The connection to Figure 26 is given not only through

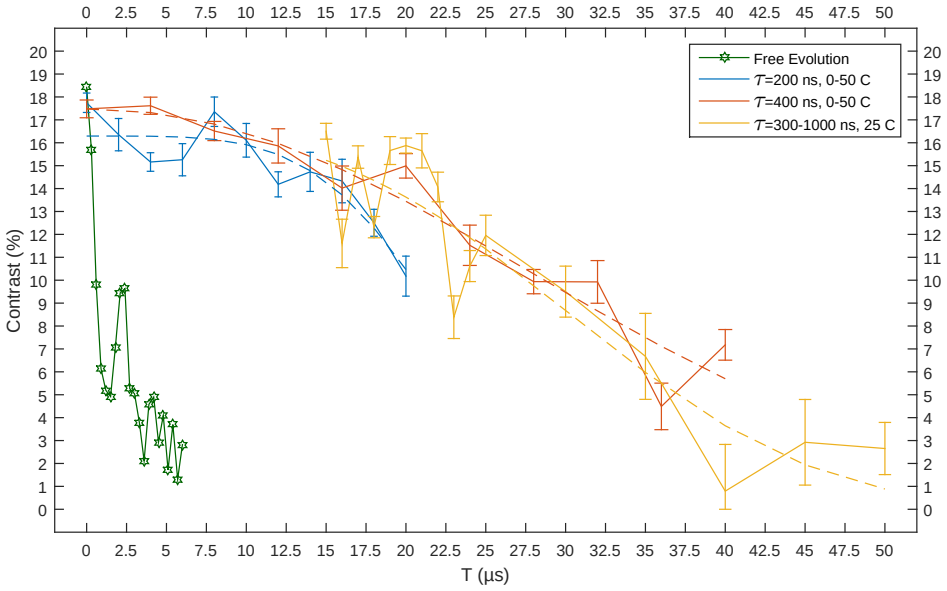

Figure 28: Rephasing with multiple spin flips. Three data sets with different methods of maintaining the coherence of the state are compared to each other and the free evolution of the state. The time axis refers to the (total) evolution time. Functions of the form $ae^{-(T/\tau)^p}$ are fitted. The extracted exponents p are 4.2±1.6, 2.09±0.49 and 3.0±1.3 and the decay constants τ are 24.2±2.4 μs, 37.9±2.4 μs and 34.8±3.3 μs, respectively. The error bars on the free evolution curve are suppressed for clarity.

this similitude in envelope but also by the fact that it is the same procedure only with evolution times inserted between the spin flips. Figure 28 shows a comparison between different methods of rephasing the electron spin, each involving multiple corrections. An interesting agreement in the course of the decay in coherence as a function of total evolution time is observed. The best coherence time lies at 40 μs which, again, differs from the free evolution by at least a factor of five. The drop at the end of the data of the third method in Figure 28 is potentially explained by the occurrence of a small revival after around 2.4 μs. This could lead to a greater build-up of remnant populations as discussed above. Generally speaking, the method of rephasing with multiple corrections seems rather limited by the fidelity of the spin flips. These are in turn limited by the splitting of the energy levels of the ^{13}C nuclear spin because a very fast pulse is needed to drive both of the spin states, which also increases off-resonant driving in other spin states of the ^{14}N nucleus. These effects result in a trade-off with an upper bound for the fidelity. On the other hand, there seems to be no evidence that the observed increase in coherence time could be explained by these imperfections. The data suggests that the decoherence of the electron spin can be genuinely reversed.

9 A Leggett-Garg-Type Test of Macrorealism

9.1 Simulating A Measurement

This chapter deals with a somewhat simplehearted demonstration which, nevertheless, has its value in the realization of an important thought experiment. The thought experiment is outlined as follows. A system is prepared in a superposition of, say, two states and two different apparatuses that fundamentally do not interact can be used in measuring the system to determine in which state it actually is. After one apparatus measures the state, the strict interpretation of quantum mechanics implies that the coherence of the state should be lost while the state of the system is still unknown to an outside observer, or apparatus (cf. Section 4.3). For this outside observer, the state of the system is truly in a mixed state while for the apparatus, or observer, that did the measurement the measurement must have had a definite outcome. The discussion of this relational nature of quantum mechanics is probably best captured by Rovelli [43], for a no-go theorem for facts about the world see Brukner [44]. While it would be interesting to realize a pair of fundamentally non-interacting apparatuses experimentally, the logic in the following demonstration is in some sense reversed. Instead of providing a pair of non-interacting apparatuses and testing whether this relational aspect can be observed, the fact that such a measurement gives an incoherent mixture for the system's state as a result is used as the starting point. The goal is to perform the second measurement of the second observer and see whether the first measurement has affected the outcome of the second measurement and if yes, in what way. The demonstration connects to the discussion by Leggett and Garg because one premise for macrorealism to hold is the non-invasiveness of the measurement (cf. Section 4.5). It is equivalent to the statement that the difference between a coherent (pure) and an incoherent (mixed) state has no reality in this world view because phases are a purely quantum mechanical entity mathematically connected to the complex representation of the system's state in a Hilbert space. The actual experiment is built up in the following way. The initial spin state is either $|0,-1\rangle$ or $|0,1\rangle$ meaning that the main population which is in $|0,1\rangle$ is either left there or transferred to $|0,-1\rangle$ with RF π-pulses. The use of two different starting states is for pragmatic reasons that will become evident soon. To simulate a measurement in an entangled basis, the identity $|\langle\psi|\phi\rangle|^2 = |\langle\phi|\psi\rangle|^2$ is exploited by transforming the initial states to the entangled basis using the same procedure as before that involves something like a Hadamard gate on the nuclear spin followed by a controlled NOT gate on the electron spin. The entangled state is then measured in the eigenbasis of the Hamiltonian through the interaction with the environment. Of course it is not really measured by anybody but the crucial point is that this does not matter. After this first measurement the entanglement sequence is applied in an inverse manner and the population in $|0,1\rangle$ is read out which constitutes the second measurement. The effect of the first measurement is studied.

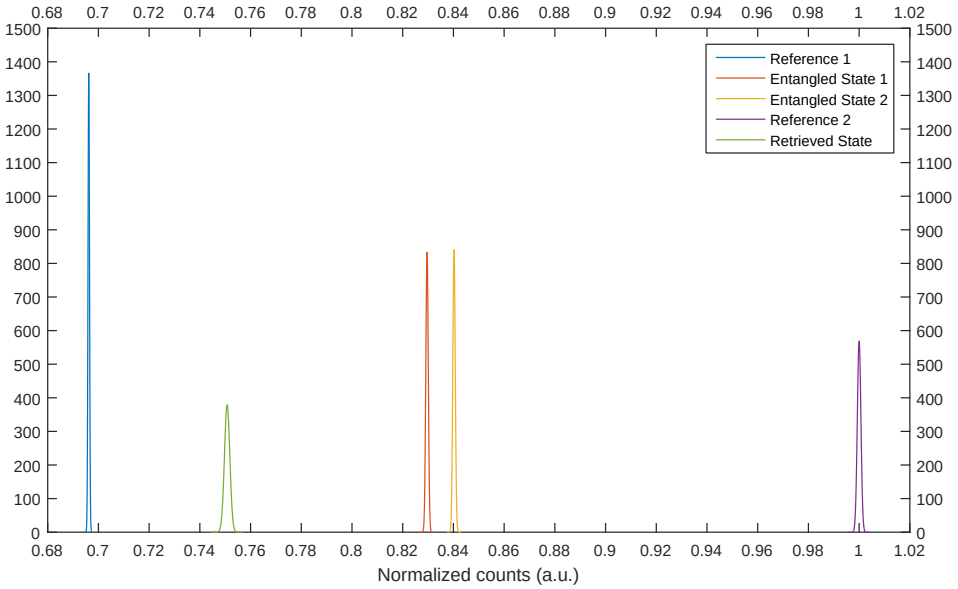

Figure 29: The effect of fundamentally independent measurements. The two outer peaks correspond to the usual measurement of two different initial spin states while the two peaks in the middle involve an intervening measurement by a fundamentally independent apparatus. It is a simulated measurement physically realised by the decoherence of the electron spin after a free evolution time of 16.16 μs. The fifth peak is an attempt to retrieve the left state by rephasing with 10 corrections (cf. Section 8).

9.2 Macrorealism and Retrieving the State

Using two reference counts from simply reading out the two above mentioned initial states, the discrepancies between the absence and presence of an intervening measurement can be illustrated. The decoherence time for simulating the measurement is 16 μs. The durations of the two MW pulses are again 202 ns and 206 ns. In Figure 29, the measured outcomes are represented by Gaussians of the observed count rates with widths corresponding to the standard errors. The simulated measurement introduces a discrepancy of at least 188 standard errors. The splitting of the two "perturbed" outcomes is attributed to imperfect pulse quality and a slight detuning due to MW frequencies that are not strictly updated. This results in a small remnant coherence. Also it is not known whether there is some non-zero coherence after 16 μs. The small lowering from the mean of the references is also tied to half of the initial population in $|0,0\rangle$ being transferred to a dark state during the readout. A fifth peak gives the outcome after rephasing with 10 corrections and $\tau = 400$ ns. The slightest frequency drift can render the adjusted phase inadequate after 40 MW pulses. Given that this is probably the case, based on observations, the result seems relatively satisfactory.

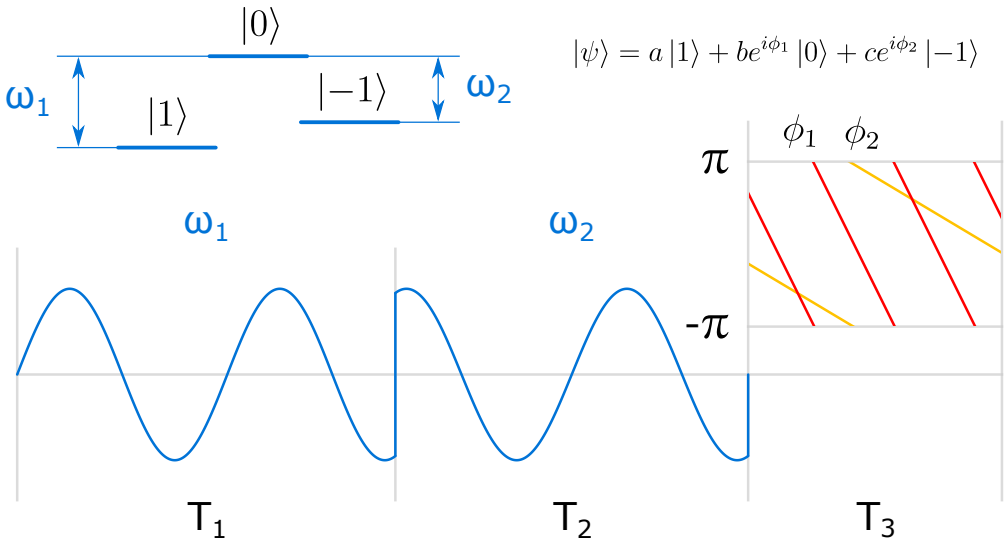

Figure 30: Preparation of an arbitrary spin state $|\psi\rangle = a\,|1\rangle + be^{i\phi_1}\,|0\rangle + ce^{i\phi_2}\,|-1\rangle$ of the ^{14}N nucleus. Starting from a nearly pure state $|1\rangle$, the targeted populations a^2, b^2 and c^2 can be achieved with sinusoidal pulses of appropriate duration. The relative phases ϕ_1 and ϕ_2 can be acquired by letting the state evolve freely. The large difference in energies makes it possible to find a waiting time T_3 that approximates the wanted phases to high accuracy. The scales are by no means meant to be in right proportion.

10 Nuclear Spin States

10.1 Preparation and Projection

The preparation and projection of potentially arbitrary spin states is a worthwhile goal when working with any quantum system because it is equivalent with the possibility of fully controlling the system. A possible scheme is provided and tested for orthogonal and nearly orthogonal states that can be used for tests of quantum mechanics. In Figure 30 the concept of preparing any spin state is illustrated. In principle, any state

$$|\psi\rangle = a\,|1\rangle + be^{i\phi_1}\,|0\rangle + ce^{i\phi_2}\,|-1\rangle \tag{49}$$

can be prepared from a pure state $|1\rangle$ by applying a RF pulse of appropriate duration T_1 to $|0\rangle$ and a subsequent pulse with duration T_2 to $|-1\rangle$. The initialization of a (nearly) pure state is discussed further below. By finding the proper pulse durations, the populations a^2, b^2 and c^2 can be achieved to high accuracy. But the phases ϕ_1 and ϕ_2 are still left to be determined by the process. By simply waiting, the phases rotate by themselves due to the energy difference of the states. For nuclear spin transition

frequencies $\frac{\omega_1}{2\pi}$ = 5056.333±0.015 kHz and $\frac{\omega_2}{2\pi}$ = 4830.171±0.026 kHz, ϕ_1 cycles approximately 5 times while ϕ_2 crosses it 113 times in a single microsecond. Given that the accuracy of the pulsing device is one nanosecond and the π-pulse durations are 105.06±0.39 μs and 105.24±0.43 μs, this is an intermediate time scale. Most importantly, it is short compared to the long coherence time of the nuclear spin. Practically speaking, the three level model suggested in Section 8.4 is utilized in combination with a numerical differential equation solver for optimizing the pulse lengths to get as near as possible to the wanted populations and then the waiting time is calculated that is not too long and that gives similar enough phases as to have a state that resembles the target state in terms of squared scalar product. The solutions often exceed 99.9 %.

To measure an arbitrary nuclear spin state, a similar method as the preparation procedure is developed. Let's call the state that is to be measured $|\phi\rangle$. Imagine that $|\phi\rangle$ is prepared even though the spin can be in an arbitrary state for this to work, as will be argued. For the reversal of the transformation from $|1\rangle$ to $|\phi\rangle$ to work, the RF signals must have the continued phases from the preparation after the total preparation time of $T_p = T_1 + T_2 + T_3$. In addition, a phase shift of π is needed in both segments (two frequencies) of the RF signal for the Rabi oscillations to be reversed by flipping the rotation axis in the Bloch sphere picture. The RF signal for preparing a state $|\psi\rangle$ is

$$U^{\psi}(t) = U_0\big[\cos(\omega_1 t)\Theta(t)\Theta(T_1^{\psi} - t) + \cos(\omega_2 t)\Theta(t - T_1^{\psi})\Theta(T_1^{\psi} + T_2^{\psi} - t)\big],$$

where U_0 is the voltage amplitude and $\Theta(t)$ is the Heaviside step function. After the application of this signal and a waiting time T_3^{ψ}, the state $|\psi\rangle$ is prepared. The signal

$$\begin{aligned} U_{\phi}(t) =& U_0\Big\{ \cos\big[\omega_1(t + T_p^{\phi}) + \pi\big]\Theta(t - T_p^{\psi})\Theta(T_p^{\psi} + T_{\phi}^1 - t) \\ &+ \cos\big[\omega_2(t + T_p^{\phi}) + \pi\big]\Theta(t - T_p^{\psi} - T_{\phi}^1)\Theta(T_p^{\psi} + T_{\phi}^1 + T_{\phi}^2 - t)\Big\}, \end{aligned}$$

can then be used to measure the state $|\phi\rangle$ on $|\psi\rangle$. The pulse durations T^1 and T^2 for reading a state are notationally distinguished because they can differ from T_1 and T_2. They are optimized separately. The complete RF signal $U_{\phi}^{\psi}(t) = U^{\psi}(t) + U_{\phi}(t)$ is written onto the frequency generator as an arbitrary waveform and then sent through the wires under the diamond after the spin initialization procedure. Mathematically speaking, the measurement of ϕ is a transformation that brings $|\phi\rangle$ back to the state $|1\rangle$. It is described by a unitary $\hat{U}_{\phi}$. Without loss of generality, it can be expressed as

$$\begin{aligned} \hat{U}_{\phi} &= \sum_{mn} u_{mn} |\tilde{m}\rangle \langle\tilde{n}| = \sum_{mn} \Big[\sum_i |i\rangle \langle i|\Big] u_{mn} |\tilde{m}\rangle \langle\tilde{n}| \\ &= \sum_i |i\rangle \Big[\sum_{mn} \langle\tilde{n}| \langle i|\tilde{m}\rangle u_{mn}\Big] = |1\rangle \langle\alpha| + |0\rangle \langle\beta| + |-1\rangle \langle\gamma|, \end{aligned}$$

where $|\tilde{m}\rangle$, $|\tilde{n}\rangle$ etc. are arbitrary states and $|i\rangle$ are the spin eigenstates with $i = -1, 0, 1$. From the fact that $\hat{U}_\phi$ projects $|\phi\rangle$ onto $|1\rangle$, it follows that $|\alpha\rangle = |\phi\rangle$ and $\langle\beta|\phi\rangle = \langle\gamma|\phi\rangle = 0$. Secondly, $|\beta\rangle$ and $|\gamma\rangle$ are also orthogonal because unitarity implies

$$\hat{U}_\phi^\dagger \hat{U}_\phi = |\phi\rangle\langle\phi| + |\beta\rangle\langle\beta| + |\gamma\rangle\langle\gamma| \stackrel{!}{=} \hat{\mathbb{1}}$$

and an application of $|\beta\rangle$ or $|\gamma\rangle$ on both sides leads to this conclusion. The main insight then emerges as the identity $|\langle 1|\hat{U}_\phi|\psi\rangle|^2 = |\langle\phi|\psi\rangle|^2$ which ultimately says that reading out the state $|1\rangle$ after applying $\hat{U}_\phi$ to $|\psi\rangle$ is just as good as directly measuring $|\phi\rangle$ on $|\psi\rangle$ as long as $\hat{U}_\phi$ transforms $|\phi\rangle$ to $|1\rangle$. The above description gives a complete guide on working with arbitrary spin states when given a pure state $|1\rangle$. The next paragraph deals with the realization of such a state or, actually, a satisfactory approximation to it.

After the optical cycle induced by a laser pulse, the electron spin and the nuclear spin are polarized through the mechanisms described in Section 2.3. This laser pulse initiates every pulse sequence and every pulse sequence is continuously applied in a long chain of steady repetitions. Usually, millions of repetitions of the same sequence are read out as to collect a sufficient amount of data for an analysis. Before manipulating the spin and reading it out, the polarized spin populations can be redistributed in an extended initialization procedure that produces a nearly pure state. In the below experiments involving the nuclear spin, the following three initialization steps are added:

1. $|0,-1\rangle \leftrightarrow |1,-1\rangle$
   A MW π-pulse swaps the population in $|0,-1\rangle$ (≈ 1 %) with the population in $|1,-1\rangle$ (≈ 0.1 %) to bring the populations in $m_e = 0$ closer to a pure state.

2. $|0,-1\rangle \leftrightarrow |0,0\rangle$
   A RF π-pulse swaps the population in $|0,-1\rangle$ (≈ 0.1 %) with the population in $|0,0\rangle$ (≈ 8 %) to facilitate the next operation.

3. $|0,-1\rangle \leftrightarrow |-1,-1\rangle$
   A MW π-pulse swaps the population in $|0,-1\rangle$ (≈ 8 %) with the population in $|-1,-1\rangle$ (≈ 0.1 %) to bring the populations in $m_e = 0$ closer to a pure state.

The result is a nearly pure state $|0,1\rangle$, or just $|1\rangle$, with a purity of 99.3 % ($\mathrm{Tr}[\hat{\rho}^2]$) and 99.7 % of the population in $|1\rangle$ when assuming an electron spin polarization of 80 %, ideal pulses and when restricting to the electron spin 0 states. For 70 % polarization it is still 98.9 % and 99.4 % and for 90 % polarization it's 99.7 % and 99.9 %. A more detailed discussion of the populations is given in the next paragraph where all underlying processes during one measurement sequence are sifted through one after another using the observed transition frequencies and Rabi frequencies. It will serve as the foundation for a more robust analysis of the collected data. In addition, the method for extracting probabilities from the observed fluorescence counts is explained.

Main transition	Purp	T_π (ns)	f (MHz)	Main (%)	Side 1 (%)	Side 2 (%)
$\|0,-1\rangle \leftrightarrow \|1,-1\rangle$	Init	424	3912.60	97.2±3.6	3.5±1.9	0.04±0.24
$\|0,-1\rangle \leftrightarrow \|-1,-1\rangle$	Init	419	1828.63	97.2±3.5	3.1±1.8	0.00±0.13
$\|0,1\rangle \leftrightarrow \|1,1\rangle$	Read	410	1833.06	97.3±3.4	2.3±1.7	0.09±0.31

Table 1: Transition efficiencies for the initialization and readout MW pulses. The purposes of the pulses along with the π-pulse durations and frequencies are tabulated next to the transition efficiencies of the pulses (percentage of transferred population when starting with 100 %). The side transitions with a difference in nuclear spin of ± 1 and ± 2 are termed Side 1 and Side 2. The values are computed using a two level approach and a statistical mixing of both ^{13}C states and allowing for an error of 5 ns in the actual π-pulse duration (Rabi frequency) and up to 100 kHz detuning from the transition. Probabilities out of range are notationally tolerated for visual simplicity.

The MW π-pulse durations for the two initialization pulses described above are 424 ns and 419 ns, respectively. The MW frequencies are 3912.60 MHz and 1828.63 MHz. The readout pulse of 410 ns π-pulse duration and 1833.06 MHz frequency is applied to the transition $|0,1\rangle \leftrightarrow |-1,1\rangle$. As it turns out to be in good agreement with other models and the following purposes only demand a rough estimation, a two level approximation is used for the upcoming calculations. The effects of the MW pulses in terms of transition efficiencies in the main and in side transitions are tabulated in Table 1. In addition to these numbers, the following qualitative statements are crucial:

1. Any erosion of the population in $|0,1\rangle$ during the initialization only reduces the purity in electron spin 0. The reverse process is indistinguishable from an increase in purity. In fact, it is exactly that. Also this effect is extremely small because the pulses are chosen with this aim.

2. The imperfections of the initialization pulses are small and the adjustments to the purity of the state is also small (cf. Table 2).

3. The readout fluorescence is still linear in $|\langle\phi|\psi\rangle|^2$ but it involves small extra terms that can vanish completely in certain cases. (This is justified later.)

4. Any remnant coherence between the electron spin 0 states and the readout electron spin states is expected to be completely lost between initialization and readout because they are separated by well over 100 μs. Thus the readout fluorescence only depends on the populations in the electron spin 0 states that, in turn, only depend on the nuclear spin manipulations as the rest is held equal.

Electron spin 0 polarization	$\|0,1\rangle$	$\|0,0\rangle$	$\|0,-1\rangle$	$\mathrm{Tr}[\hat{\rho}^2]$
70 %	99.0 %	0.4 %	0.6 %	98.1 %
80 %	99.3 %	0.2 %	0.5 %	98.6 %
90 %	99.5 %	0.1 %	0.4 %	99.0 %

Table 2: Distribution of populations in electron spin 0 after the initialization. The obtained values for the transition efficiencies of the MW pulses from Table 1 are used to calculate the distribution of populations in electron spin state 0 as well as the purity.

The conjecture of these insights facilitates the conversion of the measurement observables (fluorescence counts) to probabilities corresponding to qutrit state projections.

The probabilities $|\langle\phi|\psi\rangle|^2$ are extracted as follows. Three fluorescence markers are measured in every set of measurements, two high ones and a low one. Simply reading the initialized state is used as the low fluorescence marker (LFM). The result of measuring a state on itself is expected to give this value. The two high fluorescence markers (HFM) consist of a π-pulse with ω_1, a π-pulse with ω_2 only for the second HFM and subsequent readout. The reason for not simply omitting the readout MW pulse is the non-zero population in $|-1,1\rangle$ that is transferred to $|0,1\rangle$ during the readout in every other sequence. So this HFM would be too low. The reason for the second HFM is the imperfect readout pulse that also drives the states $|0,0\rangle$ and $|0,-1\rangle$ off-resonantly but not equally. The least population that can end up in $|0,1\rangle$ through nuclear spin manipulations is p_0, the initial population in $|0,0\rangle$ which is the lowest of the three (cf. Table 2). In this regard it also seems to be the perfect fluorescence marker. Within this constraint, the population p_1 can end up either in $|0,0\rangle$ or in $|0,-1\rangle$. The off-resonant driving of the readout pulse slightly differentiates these two cases. Thus the second fluorescence marker. The discrepancy can be seen in Figure 31. Like the imperfections of the initialization pulses, it is a result of the ^{13}C nuclear spin. Only one MW frequency is applied and the splitting defies perfect optimization for both states.

From unitarity, the translation of error in purity to the error in fluorescence can be derived. The population $p_1^{\phi\psi}$ in the state $|1\rangle$ after preparing $|\psi\rangle$ and measuring $|\phi\rangle$ is

$$\begin{aligned} p_1^{\phi\psi} = \sum_i p_i |\langle 1| \hat{U}_\phi \hat{U}^\psi |i\rangle|^2 &= p_1 P_\phi^\psi + p_0 P_\phi^{\psi^{\perp_1}} + p_{-1} P_\phi^{\psi^{\perp_2}} \\ &= p_0 + (p_1 - p_0) P_\phi^\psi + (p_{-1} - p_0) P_\phi^{\psi^{\perp_2}}. \end{aligned} \tag{50}$$

So the population is still linear in the probability P_ϕ^ψ but it contains an extra term that is proportional to the difference $p_{-1} - p_0$ which, according to the above calculations,

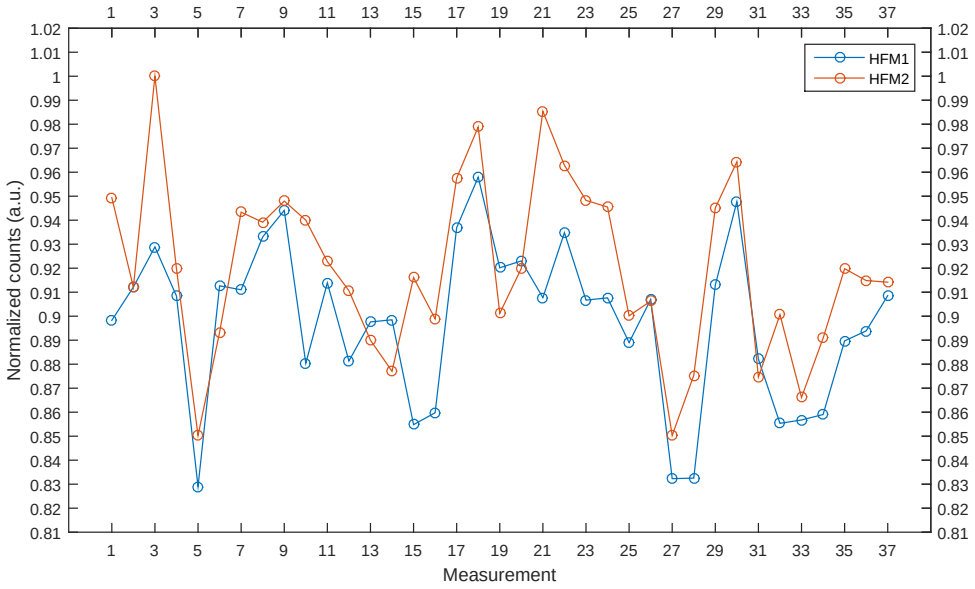

Figure 31: High fluorescence markers (HFMs) for measuring probabilities. To convert fluorescence counts into probabilities, adequate low and high fluorescence markers that indicate 0 % and 100 % have to be found. The illustrated data shows two different HFMs that cover the full interval of an unknown parameter. The reason for this obscurity is an imperfect readout pulse that differentiates otherwise equivalent measurement outcomes through off-resonant driving (see main text for the full explanation of this).

is positive. $|\psi^{\perp_2}\rangle$ is an orthogonal state that is generated from $|-1\rangle$ by $\hat{U}^{\psi}$. A similar treatment can be applied for the populations $p_o^{\phi\psi}$ and $p_{-1}^{\phi\psi}$ after the measurement, i.e.

$$\begin{aligned} p_0^{\phi\psi} &= \sum_i p_i |\langle 0| \hat{U}_\phi \hat{U}^\psi |i\rangle|^2 = p_0 + (p_1 - p_0) P^{\psi}_{\phi_{\perp_1}} + (p_{-1} - p_0) P^{\psi^{\perp_2}}_{\phi_{\perp_1}} \\ &= p_1 + p_{-1} - p_0 - (p_1 - p_0)(P^{\psi}_{\phi} + P^{\psi}_{\phi_{\perp_2}}) - (p_{-1} - p_0)(P^{\psi^{\perp_2}}_{\phi} + P^{\psi^{\perp_2}}_{\phi_{\perp_2}}), \\ p_{-1}^{\phi\psi} &= \sum_i p_i |\langle -1| \hat{U}_\phi \hat{U}^\psi |i\rangle|^2 = p_0 + (p_1 - p_0) P^{\psi}_{\phi_{\perp_2}} + (p_{-1} - p_0) P^{\psi^{\perp_2}}_{\phi_{\perp_2}}. \end{aligned} \tag{51}$$

In the limit of $P^{\psi}_{\phi} \to 1$, these equations always give the proposed LFM where the populations are in their initial positions. This follows from the previously hinted identity

$$\langle 1| \hat{U}_\phi |\psi\rangle = \langle 1| \left\{ |1\rangle \langle\phi| + |0\rangle \langle\phi_{\perp_1}| + |-1\rangle \langle\phi_{\perp_2}| \right\} |\psi\rangle = \langle\phi|\psi\rangle \tag{52}$$

because it implies that $\hat{U}^{\dagger}_{\phi} |1\rangle = |\phi\rangle$ for any $|\phi\rangle$ and thus $\hat{U}^{\dagger}_{\phi} = \hat{U}^{\phi}$. It follows that $|\phi_{\perp_1}\rangle = \left[\langle\phi^{\perp_1}| \right]^{\dagger}$ and $|\phi_{\perp_2}\rangle = \left[\langle\phi^{\perp_2}| \right]^{\dagger}$. The orthogonal states generated by $\hat{U}^{\phi}$

are exactly the same states that map back to the initial states through $\hat{U}_\phi$. Thus the above conclusion for the case $|\phi\rangle = |\psi\rangle$. In general, the probabilities are bounded by

$$\begin{aligned} P^{\psi}_{\phi_{\perp_2}} \leq & 1 - P^{\psi}_{\phi}, \\ P^{\psi^{\perp_2}}_{\phi} \leq & 1 - P^{\psi}_{\phi}, \\ P^{\psi^{\perp_2}}_{\phi_{\perp_2}} \leq & 1 - P^{\psi}_{\phi_{\perp_2}}, \\ P^{\psi^{\perp_2}}_{\phi_{\perp_2}} \leq & 1 - P^{\psi^{\perp_2}}_{\phi}. \end{aligned} \tag{53}$$

The last terms in the Equations 51 are neglected because they are extremely small. Their maximum absolute values are approximately 0.6 % and 0.3 % assuming an electron spin polarization of 80 % (cf. Table 2) and the off-resonant readout efficiency are 2.3 % and 0.09 % (cf. Table 1) which gives a maximum population error of $< 1.5 \times 10^{-2}$ % in total. Within this approximation, the LFM is an ideal reference. Also the last term in Equation 50 is dropped. Its maximum population error lies at approximately 0.3 %. The error has a positive sign in the sense that it can result in a slightly higher probability. As stated before, this term vanishes for the LFM. The observed fluorescence rates of the actual measurements include it but the measurements HFMs do not because they are not constructed as such. While the first term in Equation 51 is rigorously used to find the extreme values that correspond to the two HFMs, the same is not done for the last term in Equation 50 which would include a HFM that transfers p_{-1} to $|1\rangle$. Instead, the lowest value is adopted in the choice of the HFMs. The consequence is that nearly orthogonal states can appear slightly less orthogonal while very similar states are unaffected. Including this term would give darker HFMs because it would result in a slightly greater population that is transferred to the dark state (because $p_{-1} - p_0 > 0$). The probabilities are calculated with the formula

$$P = \frac{r - r_{HFM}}{r_{LFM} - r_{HFM}}, \tag{54}$$

where r is the fluorescence count rate of the measurement, $r_{HFM} = \frac{1}{2}(r_{HFM1} + r_{HFM2})$ the rate of the HFM and r_{LFM} the rate of the LFM. This is easily justified through the linearity of the fluorescence in the populations $p_1^{\phi\psi}$, $p_0^{\phi\psi}$ and $p_{-1}^{\phi\psi}$, and the linearity of the populations in P^{ψ}_{ϕ}. The mean value for the HFMs is explained as follows. The value of the probability $P^{\psi}_{\phi_{\perp_2}}$ is 0 for HFM1 and 1 for HFM2. The correct HFM would have a value that results from an interpolation from the LFM with $P^{\psi}_{\phi_{\perp_2}} = 0$ through the value corresponding to the states of the measurement. That is the point where linearity in P^{ψ}_{ϕ} applies. This point is unknown. For any $P^{\psi}_{\phi} \in [0, 1]$ it can have any value $P^{\psi}_{\phi_{\perp_2}} \in [0, 1]$. A large measurement set of state pairs with the same overlap would give a symmetric distribution about the mean value $P^{\psi}_{\phi_{\perp_2}} = \frac{1}{2}$ because of the

	Raw		Normalized	
	R	O	R	O
$\|\psi_1^c\rangle$	99.00±1.27 %	2.77±2.25 %	102.29±1.47 %	1.70±2.90 %
$\|\psi_2^c\rangle$	98.58±1.21 %	-2.83±1.75 %	101.03±1.78 %	-0.03±2.19 %
$\|\psi_1^1\rangle$	98.93±1.90 %	-0.69±1.81 %	101.28±2.06 %	-2.24±2.60 %
$\|\psi_2^1\rangle$	97.82±1.43 %	-1.11±2.15 %	98.59±2.03 %	-0.24±2.49 %
$\|\psi_1^2\rangle$	100.06±1.22 %	0.66±1.95 %	101.01±1.62 %	2.35±2.41 %
$\|\psi_2^2\rangle$	95.86±1.36 %	3.15±1.76 %	98.32±1.68 %	3.24±2.09 %
$\|\psi_1^3\rangle$	98.26±1.54 %	-0.12±1.63 %	98.44±1.53 %	1.93±2.32 %
$\|\psi_2^3\rangle$	97.50±1.33 %	-1.91±2.05 %	99.50±2.00 %	1.08±2.24 %

Table 3: Reversibilities and orthogonalities of eight states. For odd row numbers the orthogonalities (O) give measurements of the state with the state in the next row and for even row measurement with the above state. Reversibilities (R) are states measured on themselves. Raw and normalized refer to whether the fluorescence counts are normalized with the technique described in the main text before computing the probabilities. The targeted states have perfect orthogonality and can be found in Appendix Section A.3. Probabilities out of range are notationally tolerated for simplicity.

linearity. In the following data, for each data set the probability is computed individually with the mean HFM and the variance is taken as the squared maximal distance to the marginal values. The variance of the mean value of the data points is added to the combined variances of the individual data points. Each data point is measured for 1 minute and 37 identical measurement sets are collected in total.

10.2 Reversibility and Orthogonality

The ability to reverse a state, i.e. measure it on itself, is an important feature where having the same state in the preparation and in projection is required. Table 3 as well as Figures 32 and 33 show the outcomes of measuring the reversibilities and orthogonalities of eight states. The results are split into probabilities computed from the raw fluorescence counts and those where a novel normalization technique is applied prior to this calculation. The technique involves the threefold repetition of the sequence. In the second copy no MW readout pulse is used and in the third one two strong pulses (34 ns and 61 ns) to different electron spin states are applied for two reference counts.

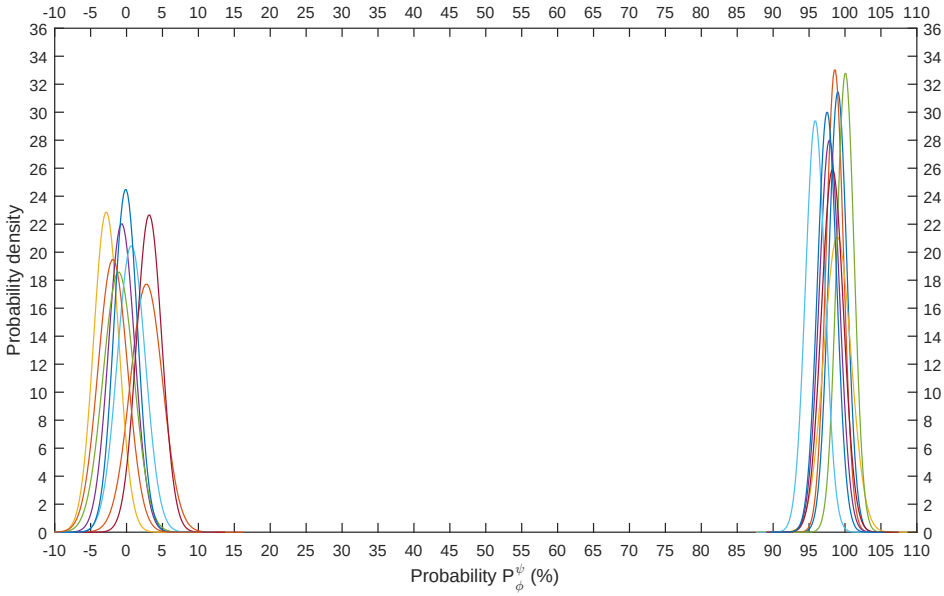

Figure 32: Reversibilities and orthogonalities of eight states (cf. Section A.3 of the Appendix). The Gaussian peaks show the probabilities of eight self-measurements and four pairwise orthogonal measurements including the reversed equivalents. The widths are determined by the variances described in the main text at the end of Section 10.1.

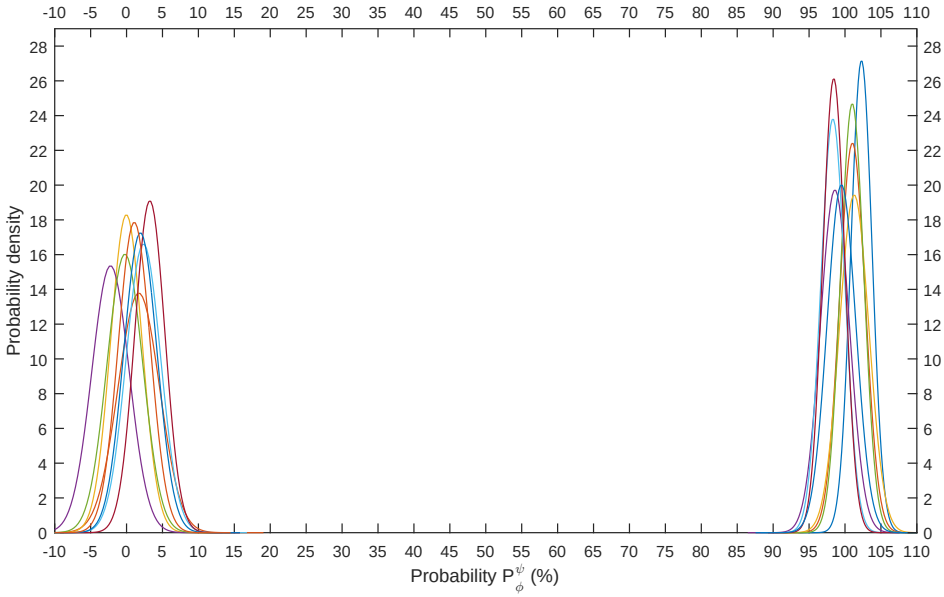

Figure 33: Reversibilities and orthogonalities using normalized counts (see main text).

10.3 Towards Testing the Quantum State's Ontology

The focus on orthogonal states originates from the idea of testing how accurately the procedure discriminates states. Another application is for testing quantum mechanics itself. It has been shown that testing the reality of the quantum state is more fault-tolerant than previously assumed [35], at least for the qutrit case but possibly also for higher dimensions. Knee's algorithm for calculating optimal states for such a test is utilized and the resulting density matrices are decomposed into pure states for separate measurements. As it turns out, the density matrices are all mixtures of two pure states with nearly equal weights (cf. Appendix Section A.3). As shown in Section A.2 of the Appendix, the trace distance of two density matrices involving a nuclear norm of their difference can be approximated by probability measurements of the decomposed states. This derivation is needed to calculate the denominator in the bound for k_0:

$$k_0 \leq \frac{1+\sum_{i<j} A_{ij}}{\sum_i \omega_C(\hat{\rho}^c, \hat{\rho}^i)}, \tag{55}$$

(cf. Section 4.8) which involves the trace distance of two density matrices in the overlap terms $\omega_C(\hat{\rho}^c, \hat{\rho}^i) = 1 - \frac{1}{2}\|\hat{\rho}^c - \hat{\rho}^i\|_*$. In Section A.2 an upper bound, actually, rather than an approximation for the trace distance is found where it is expressed through measurable probabilities. An upper bound gives the biggest value for the fraction in the above inequality. The solution is the lowest upper bound and for the small imbalance in weights of the density matrices it is dominated by the maximum scalar product of the states $\max\{|\langle\psi_1^c|\psi_2^c\rangle|, |\langle\psi_1^i|\psi_2^i\rangle|\}$ and the dependence is very well described by a linear approximation. The consequence is that even for actually perfectly orthogonal states the greatest error due to the averaging of the HFM described above is picked out and it is highly amplified through the square root from probability to amplitude. Every term $\omega_C(\hat{\rho}^c, \hat{\rho}^i)$ involves a sample of only two measurements and then the maximum value is taken. Call X_1 the first scalar product and X_2 the second. The probability distributions $f_1(x_1)$ and $f_2(x_2)$ describing the ignorance of the unknown parameter described in the last section are uniform in their corresponding intervals $I_1 = [a_1, b_1]$ and $I_2 = [a_2, b_2]$ as indicated there. So the expectation value of the maximum is

$$M = E\big[\max\{X_1, X_2\}\big] = \int_{a_1}^{b_1}\int_{a_2}^{b_2} f_1(x_1) f_2(x_2) \max\{x_1, x_2\} dx_1 dx_2. \tag{56}$$

The intervals I_1 and I_2 are symmetric about the mean values $\mu(X_1)$ and $\mu(X_2)$. Perfectly orthogonal states have identical intervals and distributions which leads to

$$\begin{aligned} M =& \frac{1}{4a^2}\int_{-a}^{a}\int_{-a}^{a} \max\{x_1, x_2\} dx_1 dx_2 = \frac{1}{4a^2}\int_{-a}^{a}\left[\int_{-a}^{x_2} x_2 dx_1 + \int_{x_2}^{a} x_1 dx_1\right] dx_2 \\ =& \frac{1}{4a^2}\int_{-a}^{a}\left(\frac{x_2^2}{2} + a x_2 + \frac{a^2}{2}\right) dx_2 = \frac{1}{4a^2}\left(\frac{a^3}{3} + a^3\right) = \frac{a}{3}. \end{aligned}$$

Theory	Raw	Normalized	Theory	Raw	Normalized
3.84 %	-2.96±1.86 %	-0.04±2.18 %	2.89 %	5.48±1.57 %	6.89±2.19 %
2.52 %	3.14±1.65 %	3.17±2.02 %	4.01 %	1.64±1.48 %	4.83±1.80 %
0.22 %	6.06±1.90 %	3.53±2.40 %	0.33 %	-2.57±1.89 %	0.45±2.04 %
3.13 %	-0.46±1.55 %	2.99±2.14 %	3.50 %	9.04±1.83 %	7.87±2.12 %
3.04 %	1.36±1.72 %	-0.27±2.12 %	3.58 %	3.99±1.46 %	2.68±2.54 %
0.68 %	4.90±1.54 %	3.67±1.75 %	0.06 %	-2.52±1.66 %	-0.49±2.15 %
3.30 %	4.04±1.47 %	2.44±1.89 %	3.26 %	-0.76±1.73 %	3.75±2.03 %
3.88 %	7.75±1.66 %	10.35±2.31 %	2.84 %	7.79±1.73 %	3.57±2.33 %
0.16 %	3.93±1.62 %	3.74±2.01 %	0.36 %	0.08±1.37 %	3.14±2.24 %

Table 4: Probabilities for the antidistinguishability. The first three rows are the three outcomes of the first POVM measurement, the second set of three outcomes the second POVM measurement etc. The two states separated horizontally are the two states of which the density matrix is composed. See Appendix Section A.3 for the states. Negative probabilities are tolerated for ease of notation and to highlight discrepancies.

For the two HFMs, the nominal probability values are computed which correspond to the marginal probability values in the described interval. A third of the square root of their equal distance to zero, which is 3.96 % for the probabilities calculated from the raw counts and 2.60 % for the probabilities calculated from the normalized counts, is subtracted from the scalar products in calculating the overlaps to correct for the above shift. Note that this is not an argument about epistemic states of quantum systems but simply an experimental inadequacy described with probability theory. For computing the epistemicness from the measurements, matching orthogonalities are averaged and in non-linear functions the variances are taken as the squared distances to the marginal values. The values used to calculate the antidistinguishability are given in Table 4. Negative probabilities are taken to be zero. The values obtained for the bound in Equation 37 are $88.76^{+9.55}_{-8.76}$ % for the raw counts and $92.40^{+8.55}_{-7.33}$ % for the normalized counts. Note that the lower error margin of the first value might be slightly lower than theoretically possible. One very important recapitulation is the method by which these values are arrived at. The pulse sequences calculated with the qutrit model are instructions fed into the machine. The assumptions for the measurement process rely on properties of the readout pulse and the purity of the initial state. This chapter is more of a proof for the theory than an experiment that relies on theoretical justification.

11 Discussion

The results once again highlight the value of the nitrogen-vacancy center as a tool for conducting quantum information experiments. With this particular diamond sample, a central, limiting role is attributed to the extra spin, speculated to be a ^{13}C nucleus, that is coupling to the electron spins. It makes the construction of fast pulses for achieving electron spin gates with near perfect fidelity impossible because the energy level splitting defies an optimization for both transition frequencies. This is certainly the case for the rectangular pulses used here. The consequence is an optimized pulse that has small but non-zero off-resonant driving of secondary electron spin transitions and high but imperfect driving of the main transition, thereby restricting the range of possibilities for certain experiments. The reversal of the electron spin decoherence through inverting the spin state in particular is contingent upon a high fidelity of the spin flips. But also the imperfect readout in the ontology experiment traces back to this problem and introduces an additional uncertainty in the data. From a more general perspective, however, this extra system could serve as a means of extending the Hilbert space of the composite spin system. By designing a signal chain that facilitates the coherent manipulation of this additional qubit, the variety of potential research directions could be widened even further. A controllable spin system with a total Hilbert space dimensionality of 18 is a desirable goal for a number of applications. The entangled two-qubit state consisting of two pairs of electron and nitrogen nucleus spin states is found to have a degree of entanglement of 94 % in Section 7. The degree of entanglement is defined as the ratio between entanglement measure and its maximally attainable value. The entanglement entropy and the negativity seem to agree on this value. While the proof of entanglement is indirect in the sense that the degree of entanglement is not directly calculated from observed quantities, it relies on highly credible data and the surrounding qualitative demonstrations of the entanglement build an empirically sound environment for it. The complete loss of coherence after 10 μs and the dependence of the degree of coherence after 5 μs on the degree of entanglement indicate the destruction of the entangled states by the environment. The astonishing degree of symmetry in the entanglement parameter also supports the demonstration's premise by confirming the expectations from correct pulse durations but non-vanishing off-resonant driving. The generalization to qutrit entanglement would be an interesting endeavour as the procedure is an attractive one. The idea of distributing coherent populations and directly measuring their mutual degrees of coherence at a later time is a highly convenient tool and can also be generalized to the point of projecting potentially arbitrary states onto on another, as was exemplified in the very last chapter. Reversal of the electron spin decoherence is partially achieved through the application of spin flips. As mentioned above, the limiting factor of the extra spin dominates the time scale over which this procedure is successful. Firstly, it contributes to the dephasing of the electron spin itself and

secondly the spin flip fidelities are impaired by the energy level splitting. While the sequential application of spin flips shown in Figure 28 suggests a smaller impact of this deficiency on the loss of coherence than the rephasing data, this need not necessarily be the case. The remnant populations caused by off-resonant driving decohere only with approximately half the splin flip time. The reason is that the spin flip consists of two steps. While this shortness causes a significant build-up of coherent remnant populations, it also allows for revivals. The single decoherence time in the actual rephasing data is longer and so the coherent part of the populations is smaller and the revivals are suppressed. This is to say that the inadequacy of the pulses probably has a greater effect in these measurements. That being sad, it is fascinating to be able to observe the attenuation of the effect of decoherence by means of partially reversing it without assuming anything particular about the nature of its origin. The macrorealism test bares deep insights that are common sense not even for most quantum physicists. It is the premise that yields these conclusions. The idea is to, mostly qualitatively but also quantitatively, show the invasiveness of a measurement by simulating the measurement of a second, fundamentally independent party which, arguably, is the most general case. Eventually, this demonstration shows the results the main party would obtain after such an intervention. They differ by at least 188 standard errors from the measurements without an intervention. The ontology experiment serves as a paragon for the idea of conducting tests of quantum mechanics with solid state spins. It also provides the operational means for preparing and projecting potentially arbitrary nuclear spin states. Two values for the epistemicness bound have been calculated from the data. The value deriving from the raw counts is preferred here. On the one hand, it is the lower value. But also the normalized counts do not seem to express any clear sign of improvement. The probability data even suggests the opposite conclusion which is why this value is discussed here. While a statistically conclusive test would require a taking into account of imperfections in reversibilities and POVM orthogonalities, the obtained value $88.76^{+9.55}_{-8.76}$ % for the epistemicness bound serves more as a proof that this test is possible with the NV center as most of the uncertainty is due to short overall measuring time. Taken seriously, it prohibits the maximally epistemic interpretation of the quantum state within one standard deviation. The lowest experimentally obtained bound known so far, using photons, is 69 % [35, 45]. An extension of the Hilbert space dimensionality could be used for reaching beneath 50 % and thereby reaching a milestone in testing the ontology of the quantum state. Most strikingly, the calculation of pulse sequences for generating and projecting qutrit states of the ^{14}N nuclear spin produces highly orthogonal states and builds a foundation for an arbitrary state formalism which could be utilized in a more involved way or generalized to other spins, keeping their coherence times in mind. For example, there is no connection between the analysis of the ontology data and the computation of the pulse sequences. The calculations are no more than instructions for reaching the

targeted goals. As was already mentioned, the uncertainty in the data is mostly due to short measurement time. While the overall time could be increased, the measurement efficiency could be decreased as well. Also the component deriving from the ^{13}C nucleus could be eliminated by initializing its spin state. As long as this is not a polarization mechanism, i.e. the localization of population in one spin state, this would increase the measuring time due to the lowered contrast and the resulting need for collecting more photons. The initialization of the nucleus' spin is also highly relevant for more advanced experimental schemes utilizing the carbon spin in the experimental protocols. Future experiments could empirically justify the preparation and projection of arbitrary spin states of the individual particles and, most importantly, ideally the composite spin state, e.g. of one ^{14}N and one ^{13}C nucleus. This would facilitate all kinds of experiments like the ontology test mentioned above and, not least, be highly advantageous in quantum computation. The generation of arbitrary spin states requires a detailed investigation of spin coherence and relaxation times, selection rules, symmetries in level splittings, the possibility of differentially applying phases to single states or phase differences between states, and, obviously, the required signal chains needed for producing these spin gates. An incremental development of these clusters of experimental intricacies therefore seems an adequate strategy and this thesis defines a small piece in this project. But the directions are diverse, the goals clear and the possibilities rich. In conclusion, the nitrogen-vacancy center can act as a very general playground for implementing spin gates and for experimenting with the relationship between the mathematical structures of quantum theory and observable physical phenomena up to the point of testing the reality of the quantum state itself, as shown here and hopefully continued.

Appendix

A.1 Eigenvalues of Reduced Density Matrices

Starting with a generic bipartite pure state $|\psi\rangle = \sum_{mn} c_{mn} |m\rangle |n\rangle = \sum_m |m\rangle |\tilde{m}\rangle$, the states $|m\rangle$ can be taken to be the eigenstates of the reduced density matrix $\hat{\rho}_A$

$$\hat{\rho}_A = \sum_m \lambda_m |m\rangle \langle m| = \mathrm{Tr}_B\big[\, |\psi\rangle \langle\psi| \,\big] = \sum_{imn} |m\rangle \langle n| \langle i|\tilde{m}\rangle \langle \tilde{n}|i\rangle \,. \tag{57}$$

The two scalar products can be swapped and summing over i gives an identity (completeness). A comparison of both sides of the equation then gives $\langle \tilde{n}|\tilde{m}\rangle = \delta_{mn}\lambda_m$. So this basis is orthogonal, too. For zero eigenvalues, the states $|\tilde{m}\rangle$ vanish. Otherwise they can be normalized with $|m'\rangle = \frac{1}{\sqrt{\lambda_m}} |\tilde{m}\rangle$. Going back to the state $|\psi\rangle$, it is now

$$|\psi\rangle = \sum_m \sqrt{\lambda_m}\, |m\rangle |m'\rangle \,. \tag{58}$$

This is actually the proof for the Schmidt decomposition of any state. The aimed at proof is a simple corollary because the reduced density matrix of the second system is

$$\hat{\rho}_B = \mathrm{Tr}_A\big[\, |\psi\rangle \langle\psi| \,\big] = \sum_{imn} \sqrt{\lambda_m \lambda_n}\, \langle i|m\rangle \langle n|i\rangle |m'\rangle \langle n'| = \sum_m \lambda_m |m'\rangle \langle m'| \,. \tag{59}$$

A.2 Overlap Calculations

To get an expression for the nuclear norm $\|\hat{\rho}^c - \hat{\rho}^i\|_*$, the matrix $\hat{\tilde{\rho}}^i = \hat{\rho}^c - \hat{\rho}^i$ in question is investigated and decomposed in minute detail until a clue is obtained.

$$\hat{\tilde{\rho}}^i = p_1^c \left|\psi_1^c\right\rangle \left\langle\psi_1^c\right| + p_2^c \left|\psi_2^c\right\rangle \left\langle\psi_2^c\right| - p_1^i \left|\psi_1^i\right\rangle \left\langle\psi_1^i\right| - p_2^i \left|\psi_2^i\right\rangle \left\langle\psi_i^2\right| = \sum_{k=1}^{4} p_k \left|\psi_k\right\rangle \left\langle\psi_k\right| \quad (60)$$

The weights $p_{\{1,2\}}^{\{c,i\}}$ are given in Section A.3 and the states $|\psi_{\{1,2\}}^c\rangle$ as well as $|\psi_{\{1,2\}}^i\rangle$ are orthogonal to each other and in the experiment nearly orthogonal. The nuclear norm of a Hermitian matrix is the sum of its absolute eigenvalues. The epistemicness is maximal when this sum is maximal as well. So the function to be maximized is

$$f = \sum_{j=1}^{3} |\lambda_j| \quad (61)$$

as to receive the most pessimistic solution in terms of a maximum upper bound on k_0. To do this, the states $|\psi_k^i\rangle$ in Eq. (60) are expressed in the eigenbasis $\{|\lambda_j\rangle\}_j$ of $\hat{\tilde{\rho}}^i$.

$$|\psi_k\rangle = \begin{pmatrix} c_{k1} \\ c_{k2} \\ c_{k3} \end{pmatrix} = c_{k1} |\lambda_1\rangle + c_{k2} |\lambda_2\rangle + c_{k3} |\lambda_3\rangle$$

$$\hat{\rho}_k = |\psi_k\rangle \langle\psi_k| = \begin{pmatrix} c_{k1} \\ c_{k2} \\ c_{k3} \end{pmatrix} \otimes \begin{pmatrix} c_{k1}^* & c_{k2}^* & c_{k3}^* \end{pmatrix} = \begin{pmatrix} |c_{k1}|^2 & c_{k1}c_{k2}^* & c_{k1}c_{k3}^* \\ c_{k2}c_{k1}^* & |c_{k2}|^2 & c_{k2}c_{k3}^* \\ c_{k3}c_{k1}^* & c_{k3}c_{k2}^* & |c_{k3}|^2 \end{pmatrix}$$

Equating the spectral decomposition of $\hat{\tilde{\rho}}^i$ to the weighted sum in Eq. (60) gives

$$\hat{\tilde{\rho}}^i = \sum_{j=1}^{3} \lambda_j |\lambda_j\rangle \langle\lambda_j| = \begin{pmatrix} \lambda_1 & 0 & 0 \\ 0 & \lambda_2 & 0 \\ 0 & 0 & \lambda_3^i \end{pmatrix} = \sum_{k=1}^{4} p_k \begin{pmatrix} |c_{k1}|^2 & c_{k1}c_{k2}^* & c_{k1}c_{k3}^* \\ c_{k2}c_{k1}^* & |c_{k2}|^2 & c_{k2}c_{k3}^* \\ c_{k3}c_{k1}^* & c_{k3}c_{k2}^* & |c_{k3}|^2 \end{pmatrix}. \quad (62)$$

So the three equations for the eigenvalues of $\hat{\tilde{\rho}}^i$ read

$$\lambda_1 = p_1^c |c_{11}|^2 + p_2^c |c_{21}|^2 - p_1^i |c_{31}|^2 - p_2^i |c_{41}|^2 \quad (63)$$

$$\lambda_2 = p_1^c |c_{12}|^2 + p_2^c |c_{22}|^2 - p_1^i |c_{32}|^2 - p_2^i |c_{42}|^2 \quad (64)$$

$$\lambda_3 = p_1^c |c_{13}|^2 + p_2^c |c_{23}|^2 - p_1^i |c_{33}|^2 - p_2^i |c_{43}|^2. \quad (65)$$

As the trace of a density matrix is one and the trace of $\hat{\tilde{\rho}}^i$ being the difference of two density matrices is thus zero, the sum of the eigenvalues has to be zero. Therefore

two eigenvalues always have to be of the same sign. These two eigenvalues are called λ_{j_1} and λ_{j_2}. Using the trace, the third eigenvalue $\lambda^i_{j_3}$ can be identified as $-\lambda^i_{j_1} - \lambda^i_{j_2}$. Thus the function that has to be maximized is

$$f = |\lambda_{j_1}| + |\lambda_{j_2}| + |\lambda_{j_1} + \lambda_{j_2}|.$$

Depending on the signs of λ_{j_1} and λ_{j_2}, one gets $f = \pm 2(\lambda_{j_1} + \lambda_{j_2})$ and thus

$$f = \pm 2\left[p^c_1(x^2_{11} + x^2_{12}) + p^c_2(x^2_{21} + x^2_{22}) - p^i_1(x^2_{31} + x^2_{32}) - p^i_2(x^2_{41} + x^2_{42})\right], \quad (66)$$

where $x_{k1} = |c_{kj_1}|$ and $x_{k2} = |c_{kj_2}|$. To maximize f in Eq. (66), one can apply the following considerations. By only using the fact that the pure states making up ρ^c and ρ^i individually satisfy some scalar products, the terms with superscript c and i can be separated and maximized independently. For the positive terms - whatever they are after deciding the sign of f - one can take the round brackets to be one as the states can be chosen such that their third component is not populated at all. Such states can still satisfy $|\langle\psi^{\{c,i\}}_1|\psi^{\{c,i\}}_2\rangle| = C$ for any $C \in [0, 1]$ for either c or i, depending on the sign of f. For the negative terms, a notational generalization of the two possible cases is undertaken by substituting the negative terms in the square brackets of Equation 66 - whatever they are - through $f = 2(1 + g)$ with the function

$$g = -q_1(y^2_{11} + y^2_{12}) - q_2(y^2_{21} + y^2_{22}) \quad (67)$$

that now still has to be maximized. It is obviously a concave function in all the y_{kj} with a maximum at $y_{kj} = 0$. But the measured scalar product $\epsilon = |\langle\psi^{\{c,i\}}_1|\psi^{\{c,i\}}_2\rangle|$ of the two states sets a constraint for the maximization. This parameter is expected to be close to zero, but this assumption is not necessary for the derivation. The quantities $F_j = y_{1j}y_{2j}$ with $j = 1, 2, 3$ can be used to formulate this constraint. If any y_{kj} is zero, then $F_j = 0$ and the same component of the second vector $y_{k'l}$ is also compatible with zero because it does not contribute to the scalar product. Otherwise, F_1 and F_2 can be substituted into Eq. (67) by using $y_{21} = \frac{F_1}{y_{11}}$ and $y_{22} = \frac{F_2}{y_{12}}$ with $y_{11}, y_{12} \neq 0$

$$g = -q_1(y^2_{11} + y^2_{12}) - q_2(\frac{F^2_1}{y^2_{11}} + \frac{F_2}{y^2_{12}}). \quad (68)$$

The gradient of g is

$$\nabla g = \begin{pmatrix} \frac{\partial g}{\partial y_{11}} \\ \frac{\partial g}{\partial y_{12}} \end{pmatrix} = \begin{pmatrix} -2q_1y_{11} + 2q_2\frac{F^2_1}{y^3_{11}} \\ -2q_1y_{12} + 2q_2\frac{F^2_2}{y^3_{12}} \end{pmatrix} \quad (69)$$

and the Hessian matrix is

$$H = \begin{pmatrix} \frac{\partial^2 g}{\partial y^2_{11}} & \frac{\partial^2 g}{\partial y_{11}\partial y_{12}} \\ \frac{\partial^2 g}{\partial y_{12}\partial y_{11}} & \frac{\partial^2 g}{\partial y^2_{12}} \end{pmatrix} = \begin{pmatrix} -2q_1 - 6q_2\frac{F^2_1}{y^4_{11}} & 0 \\ 0 & -2q_1 - 6q_2\frac{F^2_2}{y^4_{12}} \end{pmatrix} \quad (70)$$

with a strictly negative determinant. Setting the gradient of g to zero, the maximum

$$\begin{pmatrix} y_{11} \\ y_{12} \\ y_{21} \\ y_{22} \end{pmatrix} = \begin{pmatrix} \sqrt{s_1 F_1} \\ \sqrt{s_1 F_2} \\ \sqrt{s_2 F_1} \\ \sqrt{s_2 F_2} \end{pmatrix},$$

with $s_1 = \sqrt{\frac{q_2}{q_1}}$ and $s_2 = \frac{1}{s_1} = \sqrt{\frac{q_1}{q_2}}$ emerges and g can be written as $g = -2F\sqrt{q_1 q_2}$ with $F = F_1 + F_2$. Now F remains to be minimized for the maximum value of g and therefore f. The equation of the scalar product is $c^*_{k1}c_{k'1} + c^*_{k1}c_{k'3} + c^*_{k3}c_{k'3} = \epsilon e^{i\alpha}$. The sum of any set of complex numbers can only be zero if the modulus of any one number is less than or equal to the sum of the moduli of the other numbers. Bringing the term $\epsilon e^{i\alpha}$ to the left-hand side and applying this principle gives the inequalities

$$\epsilon \leq F_1 + F_2 + F_3 \tag{71}$$

together with every permutation of the term on the left-hand side with any term on the right-hand side. Using the norm of the states $\sum_{j=1}^{3} y_{kj}^2 = 1$, the third components of the two vectors can be expressed through the first two components

$$y_{13} = \sqrt{1 - y_{11}^2 - y_{12}^2} = \sqrt{1 - s_1 F}, \; y_{23} = \sqrt{1 - s_2 F} \tag{72}$$

which gives an upper bound $F \leq \min(s_1, s_2)$ and also it follows that $F_3 = y_{13}y_{23} = \sqrt{1 - s_1 F}\sqrt{1 - s_2 F} \leq 1 - F$ which is just true. The norm of the states and their scalar product are the only constraints on the states and they are encoded in the above inequalities. Rearranging and squaring the first inequality $\epsilon \leq F_1 + F_2 + F_3$ gives

$$\begin{aligned} \epsilon &\leq F + F_3 \\ \epsilon - F &\leq F_3 \\ \epsilon^2 - 2\epsilon F + F^2 &\leq 1 - F(s_1 + s_2) + F^2 \\ F(s_1 + s_2) - 2\epsilon F &\leq 1 - \epsilon^2 \\ F &\leq \frac{1 - \epsilon^2}{s_1 + s_2 - 2\epsilon} \end{aligned} \tag{73}$$

and in a similar way the second inequality $F_3 \leq F_1 + F_2 + \epsilon$ for orthogonality gives

$$F \geq \frac{1 - \epsilon^2}{s_1 + s_2 + 2\epsilon}. \tag{74}$$

It is easy to see that this lower bound is actually lower than the upper bound in Equation 73. It decreases monotonically in ϵ and its highest value at $\epsilon = 0$ is $\frac{1}{s_1+s_2} \leq \frac{1}{s_1} = s_2$ and $\frac{1}{s_1+s_2} \leq \frac{1}{s_2} = s_1$ and thus $\frac{1}{s_1+s_2} \leq \min(s_1, s_2)$. So the lower bound in Equation

74 is compatible with norm 1 and also the first inequality for orthogonality. The two remaining inequalities are $F_1 \leq \epsilon + F_2 + F_3$ and $F_2 \leq \epsilon + F_1 + F_3$. One of the variables F_1 or F_2 is still free to choose and for $F_1 = F_2$ both of the last inequalities reduce to the true inequality $\epsilon + F_3 \geq 0$. So taking the lower bound in Equation 74 and maximizing g over the two possible signs of f, the solution to the problem is

$$\begin{aligned} f &\leq 2\left\{1 - 2\min\left[\frac{1-\epsilon^2}{s_1+s_2+2\epsilon}\sqrt{q_1 q_2}\right]\right\} \\ &\leq 2\left\{1 - 2\min_{a\in\{c,i\}}\left[\frac{1-|\langle\psi_1^a|\psi_2^a\rangle|^2}{\sqrt{\frac{p_2^a}{p_1^a}}+\sqrt{\frac{p_1^a}{p_2^a}}+2|\langle\psi_1^a|\psi_2^a\rangle|}\sqrt{p_1^a p_2^a}\right]\right\}. \end{aligned} \tag{75}$$

A.3 States and POVMs

In the following representations, both of the given matrices contain quantum states as their rows. The columns express their components, e.g. in the basis $\{|-1\rangle, |0\rangle, |1\rangle\}$ of the ^{14}N nuclear spin. The eight states used in Sections 10.2 and 10.3 are

$$\begin{pmatrix} |\psi_1^c\rangle \\ |\psi_2^c\rangle \\ |\psi_1^1\rangle \\ |\psi_2^1\rangle \\ |\psi_1^2\rangle \\ |\psi_2^2\rangle \\ |\psi_1^3\rangle \\ |\psi_2^3\rangle \end{pmatrix} = \begin{pmatrix} 0.836109 + 0.139712i & -0.371852 - 0.230203i & 0.300225 + 0i \\ -0.219434 + 0.254338i & -0.148108 + 0.562636i & 0.74072 + 0i \\ 0.0162826 + 0.296575i & 0.0634338 - 0.502966i & 0.809184 + 0i \\ -0.719003 + 0.405708i & -0.401471 - 0.282469i & -0.278331 + 0i \\ 0.544688 + 0.321391i & 0.620716 + 0.371706i & -0.276711 + 0i \\ -0.225326 + 0.116085i & 0.473569 + 0.0650543i & 0.840983 + 0i \\ 0.0718171 - 0.428786i & -0.467282 - 0.453615i & 0.621986 + 0i \\ -0.128229 - 0.563556i & 0.612743 + 0.390543i & 0.371463 + 0i \end{pmatrix}.$$

They originate pairwise from the decomposition of four density matrices with weights

$$\begin{pmatrix} p_1^c \\ p_2^c \\ p_1^1 \\ p_2^1 \\ p_1^2 \\ p_2^2 \\ p_1^3 \\ p_2^3 \end{pmatrix} = \begin{pmatrix} 0.499539 \\ 0.500461 \\ 0.486433 \\ 0.513567 \\ 0.496885 \\ 0.503115 \\ 0.488482 \\ 0.511518 \end{pmatrix}.$$

The three sets $m = 1, 2, 3$ of three-dimensional POVM measurements with three outcomes $n = 1, 2, 3$ for the ontology test in Section 10.3 are $|mn\rangle$ with

$$\begin{pmatrix} |11\rangle \\ |12\rangle \\ |13\rangle \\ |21\rangle \\ |22\rangle \\ |23\rangle \\ |31\rangle \\ |32\rangle \\ |33\rangle \end{pmatrix} = \begin{pmatrix} -0.511836 + 0.0697423i & -0.121209 + 0.631373i & 0.565541 + 0i \\ 0.701998 + 0.33998i & -0.353362 + 0.00107471i & 0.516475 + 0i \\ -0.113691 - 0.334435i & 0.390452 - 0.5562i & 0.642975 + 0i \\ -0.145979 - 0.465692i & -0.475486 + 0.547928i & 0.485294 + 0i \\ 0.261818 + 0.694026i & -0.0121499 + 0.0573532i & 0.668089 + 0i \\ -0.184515 - 0.421373i & 0.423489 - 0.539359i & 0.564046 + 0i \\ 0.547434 - 0.352178i & 0.550079 + 0.267121i & 0.449829 + 0i \\ -0.240746 + 0.584332i & 0.114899 + 0.371594i & 0.670309 + 0i \\ -0.143811 - 0.395225i & 0.288754 - 0.625618 & 0.590203 + 0i \end{pmatrix}.$$

Acknowledgements

I want to thank Professor Philip Walther for giving me the opportunity to work in the laboratory. It turned out to be a great venture into experimental quantum physics with very insightful work. While the nitrogen-vacancy center is of great utility, "It's just a rock on a table", as my supervisor Michael Trupke - who I am also deeply grateful to - put it once. Also I want to thank Daniel Wirtitsch for introducing me to the lab, into NV center physics and for helping me out a lot. I was also pleased to work with my colleagues Sarah Reisenbauer, Cameron Salter, Rui Vasconcelos and Georg Wachter.

References

1. Manson, N. & Harrison, J. Photo-ionization of the nitrogen-vacancy center in diamond. *Diamond and Related Materials* **14,** 1705 –1710 (2005).
2. Kehayias, P. *et al.* Infrared absorption band and vibronic structure of the nitrogen-vacancy center in diamond. *Phys. Rev. B* **88,** 165202 (2013).
3. Doherty, M. W. *et al.* The nitrogen-vacancy colour centre in diamond. *Physics Reports* **528,** 1–45 (2013).
4. Gruber, A. *et al.* Scanning Confocal Optical Microscopy and Magnetic Resonance on Single Defect Centers. *Science* **276,** 2012–2014 (1997).
5. Balasubramanian, G. *et al.* Ultralong spin coherence time in isotopically engineered diamond. *Nature Materials* **8,** 383–387 (2009).
6. Dutt, M. V. G. *et al.* Quantum Register Based on Individual Electronic and Nuclear Spin Qubits in Diamond. *Science* **316,** 1312–1316 (2007).
7. Neumann, P. *et al.* Multipartite Entanglement Among Single Spins in Diamond. *Science* **320,** 1326–1329 (2008).
8. Togan, E. *et al.* Quantum entanglement between an optical photon and a solid-state spin qubit. *Nature* **466,** 730–734 (2010).
9. Neumann, P. *et al.* Quantum register based on coupled electron spins in a room-temperature solid. *Nature Physics* **6,** 249–253 (2010).
10. Santori, C *et al.* Nanophotonics for quantum optics using nitrogen-vacancy centers in diamond. *Nanotechnology* **21,** 274008 (2010).
11. Waldherr, G., Neumann, P., Huelga, S. F., Jelezko, F. & Wrachtrup, J. Violation of a Temporal Bell Inequality for Single Spins in a Diamond Defect Center. *Phys. Rev. Lett.* **107,** 090401 (2011).
12. Fuchs, G. D., Dobrovitski, V. V., Toyli, D. M., Heremans, F. J. & Awschalom, D. D. Gigahertz Dynamics of a Strongly Driven Single Quantum Spin. *Science* **326,** 1520–1522 (2009).
13. Alfasia, N. *et al.* Diamond magnetometry of Meissner currents in a superconducting film. *AIP Advances* **6,** 075311 (2016).
14. Howard, M *et al.* Quantum process tomography and Linblad estimation of a solid-state qubit. *New J. Phys.* **8,** 33 (2006).
15. Beveratos, A. *et al.* Single Photon Quantum Cryptography. *Phys. Rev. Lett.* **89,** 187901 (2002).
16. Alléaume, R *et al.* Experimental open-air quantum key distribution with a single-photon source. *New J. Phys.* **6,** 92 (2004).

17. Lucio Robledo1 Hannes Bernien, T. v.d. S. & Hanson, R. Spin dynamics in the optical cycle of single nitrogen-vacancy centres in diamond. *New J. Phys.* **13,** 025013 (2011).

18. Poggiali, F., Cappellaro, P. & Fabbri, N. Measurement of the excited-state transverse hyperfine coupling in NV centers via dynamic nuclear polarization. *Phys. Rev. B* **95,** 195308 (2017).

19. Ivády, V. *et al.* Theoretical model of dynamic spin polarization of nuclei coupled to paramagnetic point defects in diamond and silicon carbide. *Phys. Rev. B* **92,** 115206 (2015).

20. Zeuch, D., Hassler, F., Slim, J. & DiVincenzo, D. P. Exact Rotating Wave Approximation. *arXiv:1807.02858* (2018).

21. Zurek, W. H. Quantum origin of quantum jumps: Breaking of unitary symmetry induced by information transfer in the transition from quantum to classical. *Phys. Rev. A* **76,** 052110 (2007).

22. Zurek, W. H. Probabilities from entanglement, Born's rule $p_k = \mid \psi_k \mid^2$ from envariance. *Phys. Rev. A* **71,** 052105 (2005).

23. Lindblad, G. On the generators of quantum dynamical semigroups. *Comm. Math. Phys.* **48,** 119–130 (1976).

24. Gorini, V., Kossakowski, A. & Sudarshan, E. C. G. Completely positive dynamical semigroups of N-level systems. *Journal of Mathematical Physics* **17,** 821–825 (1976).

25. Dominy, J. M., Shabani, A. & Lidar, D. A. A general framework for complete positivity. *Quantum Information Processing* **15,** 465–494 (2016).

26. Weinberg, S. What happens in a measurement? *Phys. Rev. A* **93,** 032124 (2016).

27. Horodecki, M., Horodecki, P. & Horodecki, R. Separability of mixed states: necessary and sufficient conditions. *Physics Letters A* **223,** 1–8 (1996).

28. Peres, A. Separability Criterion for Density Matrices. *Phys. Rev. Lett.* **77,** 1413–1415 (1996).

29. Vidal, G. & Werner, R. F. Computable measure of entanglement. *Phys. Rev. A* **65,** 032314 (2002).

30. Von Neumann, J. *Mathematische Grundlagen der Quantenmechanik* (Springer, 1932).

31. Leggett, A. J. & Garg, A. Quantum mechanics versus macroscopic realism: Is the flux there when nobody looks? *Phys. Rev. Lett.* **54,** 857–860 (1985).

32. Pusey, M. F., Barrett, J. & Rudolph, T. On the reality of the quantum state. *Nature Physics* **8,** 475–478 (2012).

33. Leifer, M. S. Is the Quantum State Real? An Extended Review of ψ-ontology Theorems. *Quanta* **3,** 67–155 (2014).

34. Barrett, J., Cavalcanti, E. G., Lal, R. & Maroney, O. J. E. No ψ-Epistemic Model Can Fully Explain the Indistinguishability of Quantum States. *Phys. Rev. Lett.* **112,** 250403 (2014).

35. Knee, G. C. Towards optimal experimental tests on the reality of the quantum state. *New J. Phys.* **19,** 023004 (2017).

36. Grynberg, G., Aspect, A., Fabre, C. & Cohen-Tannoudji, C. *Introduction to Quantum Optics: From the Semi-classical Approach to Quantized Light* p. 84 (Cambridge University Press, 2010).

37. Kurtsiefer, C., Mayer, S., Zarda, P. & Weinfurter, H. Stable Solid-State Source of Single Photons. *Phys. Rev. Lett.* **85,** 290–293 (2000).

38. Dréau, A., Maze, J.-R., Lesik, M., Roch, J.-F. & Jacques, V. High-resolution spectroscopy of single NV defects coupled with nearby ^{13}C nuclear spins in diamond. *Phys. Rev. B* **85,** 134107 (2012).

39. Jamonneau, P., Hétet, G., Dréau, A., Roch, J.-F. & Jacques, V. Coherent Population Trapping of a Single Nuclear Spin Under Ambient Conditions. *Phys. Rev. Lett.* **116,** 043603 (2016).

40. Alvarez, G. *et al.* Local and bulk ^{13}C hyperpolarization in nitrogen-vacancy-centred diamonds at variable fields and orientations. *Nature Communications* **6,** 8456 (2015).

41. Gupta, A., Hacquebard, L. & Childress, L. Efficient signal processing for time-resolved fluorescence detection of nitrogen-vacancy spins in diamond. *J. Opt. Soc. Am. B* **33,** B28–B34 (2016).

42. Laraoui, A. *et al.* High-resolution correlation spectroscopy of ^{13}C spins near a nitrogen-vacancy centre in diamond. *Nature Communications* **4,** 1651 (2013).

43. Rovelli, C. Relational quantum mechanics. *International Journal of Theoretical Physics* **35,** 1637–1678 (1996).

44. Brukner, C. A No-Go Theorem for Observer-Independent Facts. *Entropy* **20,** 350 (2018).

45. Ringbauer, M. *et al.* Measurements on the reality of the wavefunction. *Nature Physics* **11,** 249–254 (2015).